

Development of MRI Methods to Assess Coronary Microvascular Function in Mice

A Dissertation

Presented to

the faculty of the School of Engineering and Applied Science

University of Virginia

in partial fulfillment
of the requirements for the degree

Doctor of Philosophy

by

Xinyuan (Sophia) Cui

May 2018

APPROVAL SHEET

This Dissertation
is submitted in partial fulfillment of the requirements
for the degree of
Doctor of Philosophy

Author Signature: Xinyuan Sophia Cui

This Dissertation has been read and approved by the examining committee:

Advisor: Frederick Epstein

Committee Member: Michael Salerno

Committee Member: Shayn Peirce-Cottler

Committee Member: Brent French

Committee Member: Brant Isakson

Committee Member: _____

Accepted for the School of Engineering and Applied Science:



Craig H. Benson, School of Engineering and Applied Science

May 2018

Abstract

Each year, over eight million patients in the USA visit the emergency department for chest pain or angina. The most common cause of the anginal symptom is myocardial ischemia. Traditionally, diagnosis of ischemia and the cause of angina has focused on the evaluation of the obstruction of coronary arteries by angiography for coronary artery disease (CAD). Nevertheless, a substantial percentage of patients with anginal symptoms and who show ischemia on stress testing have a normal coronary angiogram.

With the recognition of ischemia without obstructive CAD, the emerging concept in cardiology is that multiple factors including microvascular disease may be significant contributors to myocardial ischemia, and that obstructive CAD is one of the multiple potential causes. Indeed, studies have shown that a significant portion of ischemic patients has coronary microvascular disease (CMD). Patients with CMD experience recurrent chest pain and have high rates of cardiovascular events. However, the disease mechanism for CMD is not fully understood, and there is no established treatment for CMD.

Mouse models of human heart disease are widely used to investigate molecular and cellular mechanisms of disease and to investigate potential new therapies. Magnetic resonance imaging (MRI) in mice enables noninvasive and serial assessment of cardiovascular physiology and pathophysiology. In this dissertation, we aim to develop MRI methods to assess coronary microvascular function in mice. The new imaging tools combined with gene-modified mice and diet-induced obese mice would help study molecular mechanisms behind CMD and establish models of CMD to test traditional or novel treatments.

Coronary microvascular endothelial dysfunction is a biomarker and subtype of CMD. In Specific Aim 1 and 2, we developed a minimally invasive MRI method to probe coronary microvascular endothelial function or, more specifically, of coronary microvascular endothelial nitric oxide synthase (eNOS) function. Using this method, we demonstrated that coronary

microvascular eNOS dysfunction precedes impairment of myocardial perfusion reserve (MPR) in a mouse model of impaired MPR without obstructive CAD. The results from these two aims are summarized in [Chapter 2](#).

Ischemia can be assessed by perfusion MRI. In Specific Aim 3, we developed an improved perfusion MRI pulse sequence for mice, called self-gated steady-state pulsed arterial spin labeling, that quantitatively assess mouse myocardial perfusion in under 5 minutes and without contrast agents. The development and evaluation of the pulse sequence are summarized in [Chapter 3](#).

Finally, in an additional project, we tested the use of nonmetallic compound nitroxides as an alternative to gadolinium for first-pass contrast-enhanced myocardial perfusion imaging in mice. The results of nitroxides-enhance perfusion imaging are summarized in [Chapter 4](#).

Table of Contents

Abstract	3
Table of Contents.....	5
Abbreviations and Symbols	9
Chapter 1 Introduction.....	11
1.1 Coronary Microvascular Disease (CMD).....	12
1.1.1 Relevance of	12
1.1.2 Function of Coronary Microvasculature	14
1.1.3 Assessment of Coronary Microcirculation	14
1.1.4 Treatment for CMD	17
1.1.5 Mouse Models of CMD.....	18
1.2 Overall Goal	21
1.3 Endothelial Dysfunction	21
1.3.1 Relevance of Endothelial Dysfunction	21
1.3.2 Assessment of Coronary Endothelial Health	22
1.3.3 Role of eNOS in Regulating Permeability	23
Specific Aim 1 & 2.....	25
1.4 MRI Quantification of Myocardial Perfusion in Mice	26
1.4.1 First-Pass Contrast-enhanced MRI	26
1.4.2 Arterial Spin Labeling (ASL) MRI.....	31
Specific Aim 3	38

Chapter 2 MRI Assessment of Coronary Microvascular Endothelial Nitric Oxide Synthase (eNOS) Function using Myocardial T1 Mapping	39
2.1 Abstract	40
2.2 Introduction.....	41
2.3 Methods	42
2.3.1 Experimental Design	42
2.3.2 Animal Handling	44
2.3.3 MRI Acquisitions	44
2.3.4 Image analysis	46
2.3.5 Statistical Analysis	46
2.4 Results	47
2.4.1 NOS inhibition causes an increase in myocardial T1	47
2.4.2 The LNAME-induced myocardial T1 increase is mediated through eNOS.....	50
2.4.3 Myocardial perfusion does not change with LNAME.....	52
2.4.4 LNAME T1 mapping detects eNOS dysfunction in HFD mice.....	53
2.5 Discussion.....	55
 Chapter 3 Self-gated spASL: Improved Steady-Pulsed Arterial Spin Labeling using Retrospective Cardiac and Self-Navigated Respiratory Gating with Faster Looping Structure for Quantification of Myocardial Perfusion in Mice.....	 58
3.1 Abstract	59
3.2 Backgrounds	61
3.3 Methods	64

3.3.1 Self-gated spASL Pulse Sequence	64
3.3.2 Retrospective Self-navigated Reconstruction	66
3.3.3 Experimental Design	68
3.3.4 Animal Handling	68
3.3.5 MRI Acquisitions	69
3.3.6 Image analysis	70
3.3.7 Statistical Analysis	71
3.4 Results	71
3.4.1 Effect of Respiratory Gating	71
3.4.2 Comparison: Self-gated SpASL versus FAIR-LL ASL	76
3.5 Discussion	79
3.5.1 Self-navigated Respiratory Gating	80
3.5.2 Comparison of Perfusion Methods	81
3.5.3 Limitations	82
3.6 Conclusions	83
Chapter 4 First-pass Nitroxide-enhanced MRI for Imaging Myocardial Perfusion without Gadolinium	84
4.1 Abstract	85
4.2 Introduction	85
4.3 Methods	87
4.3.1 Relaxivity Measurement	87

4.3.2 Animal Experiment	88
4.3.3 Image Analysis.....	88
4.4 Results	89
4.4.1 Relaxivity Measurement	89
4.4.2 First-pass Nitroxide-enhanced MRI in Mice	90
4.5 Conclusion and Discussion.....	92
Chapter 5 Conclusions and Future Directions.....	93
5.1 Conclusions.....	94
5.1.1 Imaging Coronary eNOS Function by LNAME T1 Mapping	94
5.1.2 Self-gated spASL MRI in Mice.....	95
5.1.3 First-pass Nitroxide-enhanced MRI Myocardial Perfusion Quantification.....	95
5.2 Future Directions	96
5.2.1 Imaging Coronary eNOS Function by LNAME T1 Mapping	96
5.2.2 Improvement for Self-gated Steady State Pulsed ASL MRI in Mice.....	97
5.2.3 First-pass Nitroxide-enhanced MRI Myocardial Perfusion Quantification.....	97
Appendix A: Detection of Increased Coronary Microvascular Permeability with MRI T1 mapping and Gadolinium-labeled Albumin.....	98
Appendix B: List of Publications	103
References	107

Abbreviations and Symbols

3CP	3-Carbamoyl-PROXYL
ACh	Acetylcholine
AIF	Arterial Input Function
ANOVA	Analysis Of Variance
ASL	Arterial Spin Labeling
BLOSM	Block LOW-rank Sparsity with Motion-guidance
CAD	Coronary Artery Disease
CFR	Coronary Flow Reserve
CMD	Coronary Microvascular Disease
CS	Compressed Sensing
eNOS	Endothelial Nitric Oxide Synthase
FAIR-LL	Flow Alternating Inversion Recovery Look-Locker
FOV	Field Of View
HCD	High Cholesterol Diet
HFD	High Fat Diet
HFHSD	High Fat High Sucrose Diet
IEJ	Interendothelial Junctions
HFpEF	Heart Failure with Preserved Ejection Fraction

LGE	Late Gadolinium Enhanced Imaging
LNAME	N ^G -nitro-L-arginine methyl ester
MBF	Myocardial Blood Flow
MI	Myocardial Infarction
MPR	Myocardial Perfusion Reserve
MRI	Magnetic Resonance Imaging
NMR	Nuclear Magnetic Resonance
NO	Nitric Oxide
PET	Positron Emission Tomography
RAAS	Renin-Angiotensin-Aldosterone System
RF	Radio Frequency
ROI	Region Of Interest
ROS	Reactive Oxygen Species
spASL	Steady-State Pulsed ASL
TE	Echo Time
TF	Tissue Function
TR	Repetition Time
WT	Wild Type

Chapter 1 Introduction

1.1 Coronary Microvascular Disease (CMD)

1.1.1 Relevance of

Each year, over eight million patients in the USA visit the emergency department for chest pain or angina [1]. The most common cause of the anginal symptom is myocardial ischemia. Traditionally, diagnosis of ischemia and the cause of angina has focused on the evaluation of the obstruction of coronary arteries by angiography for coronary artery disease (CAD) [2]. Nevertheless, a substantial percentage (20 to 30% [3-5] even up to 50% [6]) of ischemic patients with angina symptoms has a normal coronary angiogram. Current evidence shows that a significant portion of these patients has coronary microvascular disease (CMD) [7-9]. Patients with CMD have high rates of cardiovascular events, including hospitalization for heart failure, sudden cardiac death, and myocardial infarction (MI) [10-15]. These patients also experience recurrent chest pain resulting in ongoing anxiety, limited exercise tolerance, and lower quality of life, making them more likely to present to health care services for repeat medical assessments and procedures [9, 16, 17]. Risk factors for CMD include aging [7, 9, 18], smoking [19], obesity [20], diabetes [21, 22], hypertension [23, 24] and hyperlipidemia [25]. Findings from the Women's Ischemia Syndrome Evaluation (WISE) study also showed that there is a high prevalence of CMD in women. CMD is present in approximately one half of women with chest pain in the absence of obstructive CAD and cannot be predicted by risk factors for atherosclerosis and hormone levels [7].

With the recognition that ischemic heart disease can occur in the presence or absence of obstructive CAD, the emerging concept in cardiology is that several factors such as microvascular dysfunction, endothelial dysfunction, thrombosis, inflammation and coronary vasospasm are significant contributors to myocardial ischemia, and that obstructive CAD is just one contributing factor [26]. This and additional editorials have proposed a paradigm shift where

it is understood that coronary microvascular disease (CMD) due to comorbidities is an important cause of ischemia [26] and a prevalent cause of heart failure with preserved ejection fraction (HFpEF) [27, 28]. Specifically, comorbidities such as obesity and diabetes lead to a systemic proinflammatory state, and subsequently causes coronary microvascular endothelial inflammation and coronary microvascular dysfunction, which in turns promotes left ventricular hypertrophy, remodeling, fibrosis, and stiffness, Figure 1-1 [27].

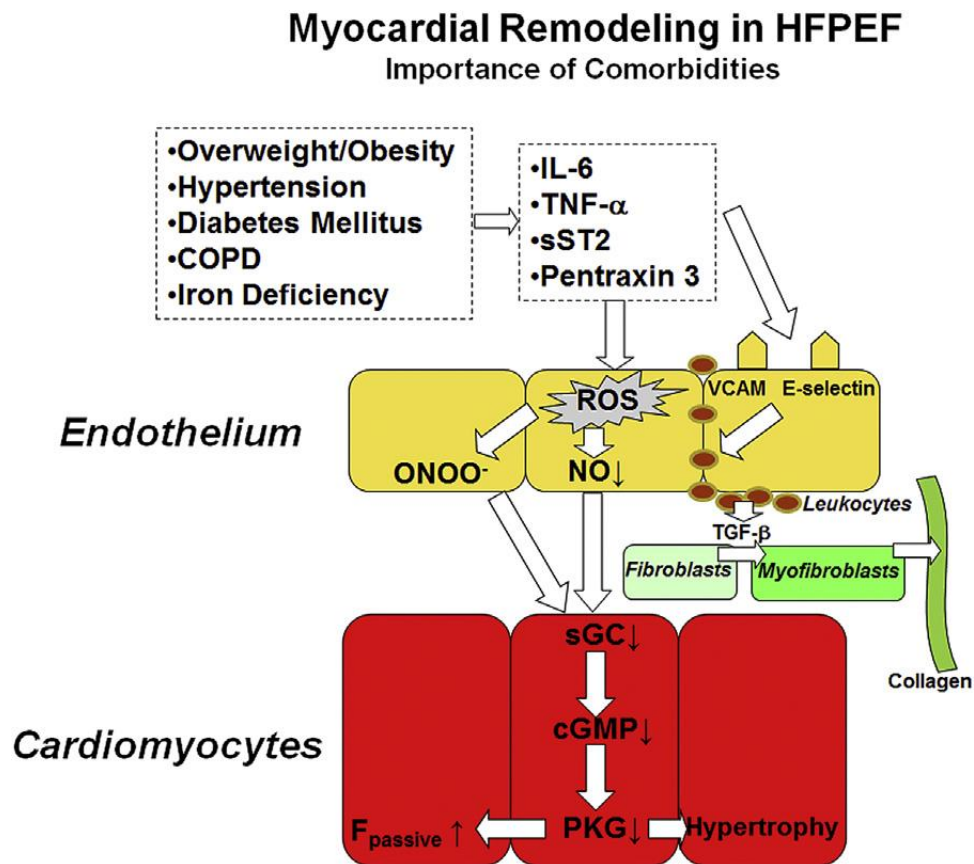


Figure 1-1. A novel paradigm for heart failure with preserved ejection fraction. Figure source: Paulus, W.J. and C. Tschöpe, A novel paradigm for heart failure with preserved ejection fraction. *Journal of the American College of Cardiology*, 2013. 62(4): p. 263-271.

1.1.2 Function of Coronary Microvasculature

The coronary arterial system is composed of three compartments [29]. The large epicardial coronary arteries have diameters ranging from 500 μm to 5 mm. The next level is the prearterioles, and they have diameters ranging from 100 to 500 μm . The smallest are the arterioles whose diameters are less than 100 μm . Prearterioles and arterioles make up the coronary microcirculation. The prearterioles are responsible for maintaining pressure, and the arterioles regulate coronary blood flow to match oxygen requirements and metabolic demands. Under normal physiological conditions, the coronary microcirculation regulates myocardial perfusion in response to increased demand by endothelial-dependent and –independent mechanisms [30]. In the pathophysiological state, the inability of the vascular smooth muscle to relax adequately at the microcirculation level indicates an endothelial-independent microvascular dysfunction. At the same time, an attenuated increase or a decrease in coronary blood flow in response to endothelial-dependent vasodilators such as acetylcholine (ACh) denotes an impairment in microvascular endothelial dysfunction. These abnormalities in the coronary microvasculature cause ischemia and chest pain in a patient with or without obstructed coronary arteries.

1.1.3 Assessment of Coronary Microcirculation

Due to the small size of the arterioles, coronary microcirculation cannot be directly visualized *in vivo* in humans. Since the microvasculature determines the coronary and myocardial blood flow, measurement of coronary flow reserve (CFR) is an assessment of the coronary microvascular function. Specifically, CFR is the magnitude of increase in the coronary blood flow between baseline and maximal vasodilation. Typically, adenosine and ACh are used to assess endothelial-independent and endothelial-dependent microvascular dysfunction, respectively, as shown in Figure 1-2 [31]. Adenosine acts on the A₂ receptor of the smooth

muscle cell and cause smooth muscle cell relaxation [32], and ACh causes the release of nitric oxide in the endothelium, which act on neighboring smooth muscle cells and cause vasorelaxation [33]. An intracoronary Doppler guidewire is used to evaluate changes in coronary blood flow in response to ACh and changes in coronary flow velocity reserve in response to intracoronary adenosine. The intracoronary Doppler guidewire is the gold standard for evaluating coronary microcirculation. However, the method is invasive by nature, and it is time-consuming, technically challenging, and not available in all facilities.

Thermodilution-derived index of microcirculatory resistance (IMR) is another invasive method for evaluating coronary microcirculation [34]. The thermodilution method estimates the mean transit time of intracoronary injection of room-temperature saline using a coronary pressure wire equipped with a temperature thermistors. The inverse of the hyperemic mean transit time has been shown to be correlated with and is a surrogate of absolute coronary blood flow [35, 36]. Study published showed that the Doppler guidewire method has superior diagnostic accuracy and sensitivity over the thermodilution method in predicting microvascular disease [37].

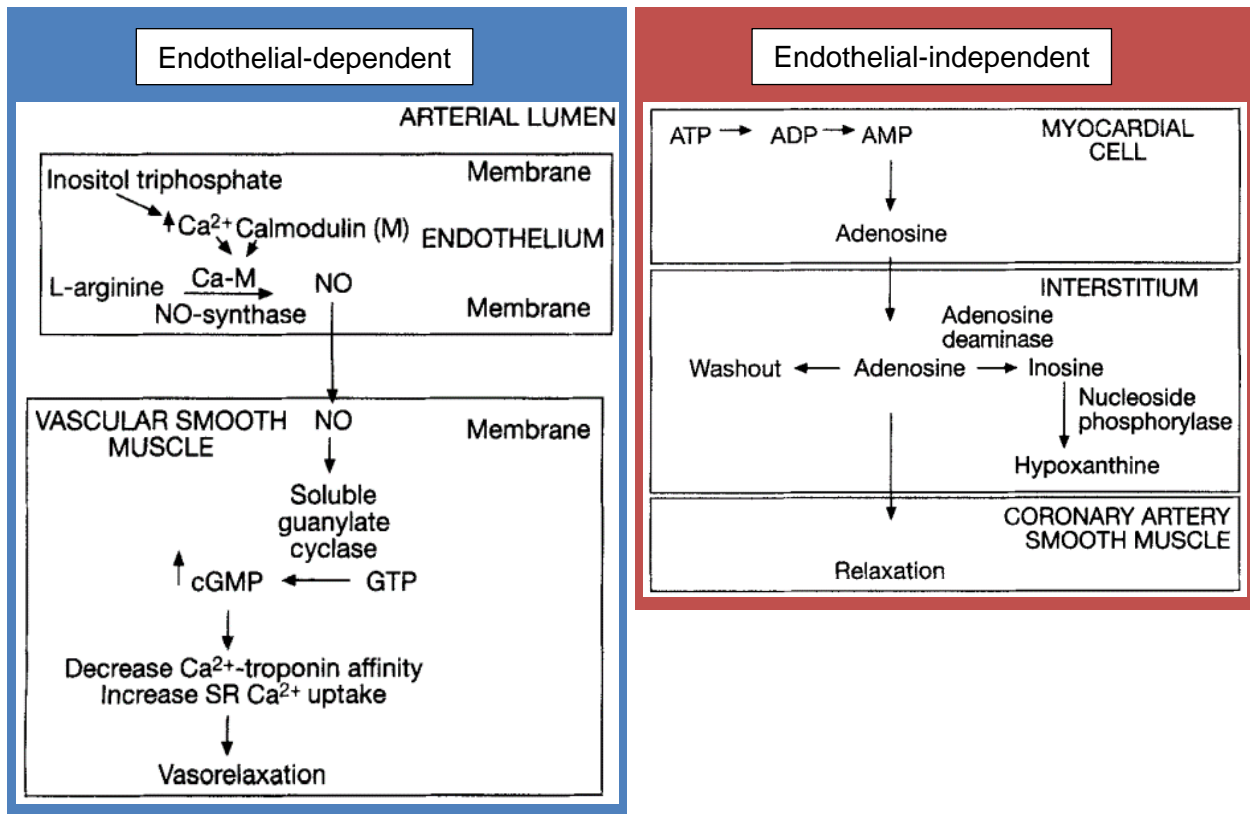


Figure 1-2. Left: Mechanisms for endothelial-dependent vasorelaxation by nitric oxide (NO). Right: Mechanisms for endothelial-independent vasorelaxation by adenosine. Image adapted from: Feliciano, L. and R.J. Henning, Coronary artery blood flow: physiologic and pathophysiologic regulation. Clin Cardiol, 1999. 22(12): p. 775-86.

The less invasive methods to assess coronary microvascular function is by measuring myocardial perfusion reserve (MPR), which also requires the finding by angiography that the patient does not have obstructive CAD. MPR is the ratio of myocardial perfusion at stress over rest measured using noninvasive techniques such as positron emission tomography (PET) and cardiac magnetic resonance imaging (MRI) analysis. Patients with angina and reduced MPR despite normal coronary angiogram are at risk for CMD. PET scanning monitors radioactive tracers to determine absolute myocardial blood flow [38]. For MRI, myocardial perfusion can be

assessed by exploiting the first-pass kinetics of T1-enhancing gadolinium-based contrast agents. During the first pass, the contrast agents diffuse into the interstitial space from the microvasculature, resulting in an increase in signal intensity that is proportional to the perfusion. Stress perfusion is measured during maximal vasodilation and is achieved by exercising or administering endothelial-independent vasodilators such as adenosine and regadenoson. Endothelial-dependent vasodilator ACh is not used to measure stress perfusion because systematic administration ACh causes a severe drop in blood pressure beyond tolerance. Although there is yet to be a consensus on the diagnostic cutoff for MPR, measurements of MPR correlate well with results from invasive measurements [39, 40], and patients with the lowest MPR values have worse prognosis [41, 42]. Other noninvasive methods to measure MPR include transthoracic Doppler echocardiography and contrast echocardiography; however, both methods suffer from excessive variability [43, 44].

1.1.4 Treatment for CMD

There is no established treatment for CMD. Current approaches to CMD treatment include reducing risk factors and incorporating atherosclerosis-treatments or angina-treatments that were developed and targeted at treating CAD. There is little evidence to support the effectiveness of the current treatment strategies for objectively-defined CMD [45]. Treatments targeting the renin-angiotensin-aldosterone system (RAAS), including Eplerenone and Enalapril have been tested as a CMD treatment, and are believed to be able to modulate the coronary microvascular tone by inhibiting angiotensin II which is a potent coronary vasoconstrictor [46-49]. Nitric oxide modulators, such as L-Arginine and Sildenafil that strengthen the guanylate cyclase signaling pathway and support endothelial nitric oxide mediation of coronary microvasculature tone has also been shown to improve CFR, but the improvements are not always significant [50-52]. Statins, with its anti-atherosclerotic effects, has been tested for its potential therapeutic

effects in CMD patients, but the improvements are not always significant [53-56]. Other studies have also examined estrogens, alpha-blockers, beta-blockers, and nitrates. Overall, there is still a lack of established treatment for CMD. A better understanding of the mechanisms underlying CMD is needed in order to facilitate the discovery and development of effective therapies.

1.1.5 Mouse Models of CMD

Despite the prevalence of CMD, the underlying disease mechanism is not fully understood, and there is no established treatment. Mouse models of human heart disease are widely used to investigate molecular and cellular mechanisms of diseases and to investigate potential new therapies. Mouse models are used extensively in research because of the similarities in the mouse cardiovascular systems to that of humans, the low cost of mouse studies, and the relative ease and success of genetic manipulation of mice [57, 58]. The experimental mouse models with microcirculation impairment can be divided into two types: 1) diet-induced obesity mouse models and 2) transgenic or knockout mouse models.

Mouse Model of Diet-induced Obesity

Obesity is one of the risk factors for microvascular dysfunction. A variety of rodent diets that induce obesity, including high-fat diet (HFD), high-fat high-sucrose diet (HFHSD), and high cholesterol diet (HCD), have been shown to also cause impaired microvascular function.

HFD mice: Mice fed an HFD are emerging as a common model of human obesity and diabetes. Aoqui et al. showed that mice fed an HFD (51% fat) for eight weeks show weight gain, blood pressure elevation, and microvascular endothelial dysfunction characterized by blunted response to ACh [59]. Furthermore, Naresh et al. showed that C57Bl/6 mice fed an HFD (60% fat) for 18–24 weeks have progressively increased LV mass and impaired MPR with fibrosis,

normal capillary density, and no aortic plaque. These results establish C57Bl/6 mice fed an HFD as a model of impaired MPR without obstructive CAD due to obesity and diabetes.

HCD mice: Stokes et al. showed that mice fed an HCD (1.25% cholesterol, 15.8% fat) for just three weeks have a significant increase in inflammation compared to control, measured by the number of leukocytes per area of vessel wall and tissue [60]. Additionally, the HCD mice have significant impairment of endothelial-dependent vascular relaxation to ACh in arterioles measured using intravital microscopy [60].

HFHSD mice: Longitudinal follow-up in mice fed an HFHSD (35 % fat, 34% high sucrose) showed that these mice developed cardiac dysfunction and a lower cardiac perfusion after four months of HFHSD feeding [61].

Transgenic Models

Models of genetically altered mice have also been shown to develop impaired microvascular function [62].

Db/db mice: Diabetes mellitus is associated with vascular complications, including impaired microvascular endothelial-dependent relaxation. The db/db mice have a mutation in leptin receptor and is a well-accepted model of type II diabetes. Starting at 24 weeks of age, db/db mice demonstrate left ventricular contractile dysfunction with preserved cardiac output and ejection fraction [63]. It has also been shown that the db/db mice have impaired coronary microvascular function assessed by examining isolated coronary arterioles [64]. Additionally, ACh-induced and capsaicin-mediated vasodilation is attenuated compared to wild-type controls, suggesting impaired endothelial-dependent vascular dysfunction [65, 66].

Sickle (BERK) mice: In sickle cell disease, intravascular sickling and attendant flow abnormalities lead to chronic inflammation and vascular endothelial abnormalities. It has been shown that transgenic-knockout Berkeley (BERK) mice have increased oxidative stress and attenuated vascular responses to NO-mediated vasoactive stimuli [67].

TRPV1(-/-) mice: DelloStritto et al. showed that TRPV1 signaling is a regulator of coronary blood flow to metabolism [66]. Contrast echocardiography showed that H₂O₂-induced vasodilation was inhibited in TRPV1(-/-) mice. Moreover, in wild-type control mice the H₂O₂-induced dilation in coronary microvessels was blocked by the TRPV1 antagonist [66].

SHR rats: In spontaneously hypertensive rats (SHR), an excess of oxidative stress is characterized by high production of free radicals, which is associated with endothelial dysfunction. Using this animal model, Neglia et al. showed that treatment with an anti-hypertensive drug leads to improvement in coronary blood flow [68].

1.2 Overall Goal

The overall goal of this dissertation is to develop MRI methods to assess coronary microvascular function in mouse models of CMD. MRI in mice enables noninvasive and serial assessment of cardiovascular physiology and pathophysiology. The new imaging tools combined with gene-modified mice and diet-induced obese mice would help study molecular mechanisms behind CMD and establish models of CMD to test traditional or novel treatments. Since CMD can be attributed to coronary endothelial-dependent dysfunction and coronary endothelial-independent dysfunction, we aim to develop noninvasive imaging tools to assess both aspects of CMD.

1.3 Endothelial Dysfunction

1.3.1 Relevance of Endothelial Dysfunction

The vascular endothelium is a monolayer of squamous epithelial cells that lines the interior surface of blood vessels. It is not only a physical barrier between circulating blood and vessel wall and underlying tissue, but it is also involved in multiple functions critical to vascular biology. Through the production of bioactive factors (most notably production of nitric oxide (NO) by endothelial nitric oxide synthase (eNOS)), the vascular endothelium closely regulates vessel tone, blood flow, and microvascular permeability. Because the endothelium is involved in such a wide range of facets maintaining the homeostasis of the body, its dysfunction is associated with a broad spectrum of human diseases and cardiovascular risk factors, including smoking [69, 70], hypercholesterolemia [71, 72], hypertension [73-75], hyperglycemia [76], familial history of

atherosclerosis [71, 77], obesity [78, 79], elevated C-reactive protein [80], and chronic systemic infection [81-83].

Because coronary endothelial dysfunction is an early and sensitive biomarker of disease progression [84-89], it has been called a “barometer” of cardiovascular health [90]. It has been shown that coronary endothelial dysfunction precedes diseases such as atherosclerosis [77, 84, 91] and is an independent predictor of cardiac events [7, 84-86, 92-96]. Suwaidi et al. found that 14% of the patients with severe coronary endothelial dysfunction, assessed by intracoronary ultrasound, had cardiac events during the 28-month follow-up, compared with no cardiac events in patients with mild to moderate endothelial dysfunction [86]. In a study of 147 patients undergoing an assessment of coronary endothelial function, 30% of the patients with CMD developed obstructive CAD at the 10-year follow-up [95]. Endothelial dysfunction is also highly prevalent in angina patients with nonobstructive CAD. Tremel and colleagues showed that in a study of 139 angina patients with nonobstructive CAD, 44% had endothelial dysfunction [97]. In addition, Ong et al. showed that 24.2% of patients with nonobstructive CAD had microvascular endothelial dysfunction [98].

1.3.2 Assessment of Coronary Endothelial Health

Strategies that identify coronary endothelial dysfunction can provide valuable information for better understanding of vascular biology, pathophysiology, and evaluation of therapy. There are several techniques for assessing endothelial function in the peripheral arteries [73, 77, 99]. However, the correlation between peripheral and coronary endothelial dysfunction is modest [100, 101]. The gold standard *in vivo* method for measuring coronary endothelial function is through invasive cardiac catheterization [102]. This technique uses quantitative coronary angiography to detect coronary artery dilatation in response to endothelial-dependent vasodilators such as ACh. In normal blood vessels, ACh causes vasodilation by stimulating

eNOS to increase endothelium-derived NO, and NO causes smooth muscle cell dilatation. Reduction or absence of endothelial-dependent dilatation indicates endothelial dysfunction.

Non-invasive imaging methods have been investigated to probe coronary endothelial function. Myocardial perfusion measured by PET can quantify absolute myocardial blood flow (MBF). However, the value of MBF is affected by epicardial vessels, resistance vessels, and the endothelium [103], accordingly, this method does not single out the endothelial effect from the total response. Coronary MRI is another technique investigated to measure endothelial health. Hayes and colleague quantitated coronary cross-sectional area and blood flow before and during isometric handgrip exercise, an endothelial-dependent stressor. Experiments were conducted in 20 healthy adults and 17 patients with coronary artery disease (CAD) [104]. Results showed that in healthy adults, coronary arteries dilated and flow increased with endothelial-dependent stress; while in CAD patients, coronary artery area and blood flow decreased with stress. None of the noninvasive methods investigated yet has the ability to probe the coronary microvascular endothelial function. We proposed that a potential way to interrogate coronary microvascular endothelial function may be to probe the role of eNOS in microvascular permeability.

1.3.3 Role of eNOS in Regulating Permeability

The vascular endothelium is an active paracrine, endocrine, and autocrine organ. In addition to regulating vessel diameter, the vascular endothelium also regulates the passage of cells and macromolecules from blood to tissue. Nitric oxide (NO) is an important protective molecule that mediates endothelial regulation of vascular homeostasis. eNOS is responsible for the generation of the majority of NO in the vascular endothelium [105]. The eNOS-mediated production of NO regulates multiple vascular functions, two of which are controlling vessel diameter and microvascular permeability [106-108]. In an inflammatory state, the vascular

endothelium, particularly eNOS, becomes a major target of reactive oxygen species (ROS). Oxidative stress causes eNOS to go through a process called eNOS uncoupling, converting eNOS from an enzyme that produces NO⁻ to producing superoxide anion. Reduced eNOS expression and NO bioavailability is directly associated with endothelial dysfunction [109], and causes an abnormal balance between vasodilators and vasoconstrictors, and increases vascular endothelial permeability [85, 110]. Studies show that in animals, inhibition of eNOS with pharmacological agents such as N^G-nitro-L-arginine methyl ester (LNAME) leads to increases in protein effluxes and microvascular fluid [106-108].

Currently, the direct measurement of coronary microvascular permeability in animals requires sacrificing animals at each time point. The Miles assay is the gold standard *in vivo* measurement to assess blood vessel permeability. It requires intravenous injection of Evans blue dye and a 30-minute waiting period, followed by organ collection. Then the Evans blue dye is extracted from the organ of interest, and the amount of Evans blue dye extravasated in interstitial tissue is quantified [111]. The invasive nature of the Miles assay prevents serial studies of endothelial dysfunction and has no potential to translate to human studies.

The nuclear magnetic resonance (NMR) spin-lattice relaxation time, or T1, characterizes the rate at which the longitudinal component of the nuclear magnetic moment recovers towards its thermodynamic equilibrium. The T1 value depends on the mobility of water in the lattice, and increased mobility leads to an increase in T1 [112]. MRI T1 mapping of the heart under baseline conditions reflects the normal homeostatic state of the coronary microvasculature.

Pharmacological inhibition of NOS rapidly depletes the local vessel wall NO concentration causing a rapid increase in microvascular permeability resulting in more protein efflux from blood to the extracellular space [106-108]. This movement of protein is accompanied by microvascular fluid efflux [107, 108]. The increase in interstitial water content in the tissue may be detected using MRI due to the elevation in the native myocardial T1 [113, 114]. Based on

this effect, we hypothesized that detection of an increase in myocardial T1 between baseline and NOS inhibition reflects a properly functioning eNOS system, i.e., one that actively maintains microvascular barrier integrity at baseline. Following this reasoning, a blunted change in myocardial T1 between baseline and NOS inhibition would be indicative of coronary endothelial dysfunction. This dissertation seeks to develop and apply these novel concepts through the following specific aims:

Specific Aim 1: To test the hypothesis that inhibition of eNOS causes an increase in myocardial T1.

(1A) Test the hypothesis that nonselective inhibition of NOS causes an increase in myocardial T1 by performing myocardial T1 mapping measurements in WT mice pre- and post-NOS inhibition.

(1B) Perform T1 mapping measurements before and after injection of a NOS inhibitor in eNOS-deficient (eNOS^{-/-}) mice. Significantly blunted changes in $\Delta T1$ in eNOS^{-/-} mice would provide strong evidence that eNOS is a major regulator of the system.

(1C) The increase in myocardial T1 after NOS inhibition could potentially also be due to vasodilatory effects. We will rule out this possibility by performing quantitative first-pass contrast-enhanced perfusion MRI with and without NOS inhibition.

Specific Aim 2: To test the hypotheses that (a) T1 mapping with NOS inhibition can detect coronary endothelial dysfunction in high-fat-diet (HFD) mice and (b) coronary endothelial dysfunction occurs before the onset of impaired perfusion reserve in HFD mice.

The results from these two aims are summarized in [Chapter 2](#). The pilot study that inspired the LNAME T1 mapping technique is summarized in [Appendix A](#).

1.4 MRI Quantification of Myocardial Perfusion in Mice

MRI perfusion imaging is the most promising non-invasive imaging technique to diagnose ischemic heart disease [115, 116]. Compared to PET, CMR has the advantage of better spatial and temporal resolution, lack of ionizing radiation, and wider scanner availability [41, 115, 117]. Myocardial contrast echocardiography [43] and Doppler echocardiography have also been shown to be able to quantify myocardial perfusion, but these methods suffer from excessive variability. Stress perfusion is measured during maximal vasodilation and is typically achieved by administering endothelial-independent vasodilators such as adenosine and regadenoson, therefore, assessing the endothelial-independent aspect of CMD.

Myocardial perfusion can be quantified using two MRI techniques, namely first-pass contrast-enhanced MRI and arterial spin labeling MRI. Both techniques are applicable to human and mice. Since the focus of this dissertation is on developing mouse MRI methods, a brief introduction of the two methods in mouse imaging is presented below.

1.4.1 First-Pass Contrast-enhanced MRI

First-pass gadolinium-enhanced perfusion MRI is an established technique for measuring myocardial perfusion and perfusion reserve in humans [118, 119]. First-pass perfusion in mice is more challenging due to their fast heart rate (300-800 beats/minute). Recent developments in the fast imaging techniques and spiral readout scheme made it possible to quantify myocardial perfusion in mice using first-pass MRI [120-122].

The first-pass method acquires serial images as an intravenously administered bolus of gadolinium contrast agent travel through the cardiac chambers and myocardium. The gadolinium contrast agents have a T1 shortening property; combined with a T1-weighted MRI pulse sequence, a bright signal is generated from gadolinium. As can be seen in the sample

images from a mouse first-pass perfusion study (Figure 1-3 [123]), the gadolinium contrast agent migrates through the right-sided cardiac chambers, followed by the left-sided chambers, and ultimately the myocardium [120].

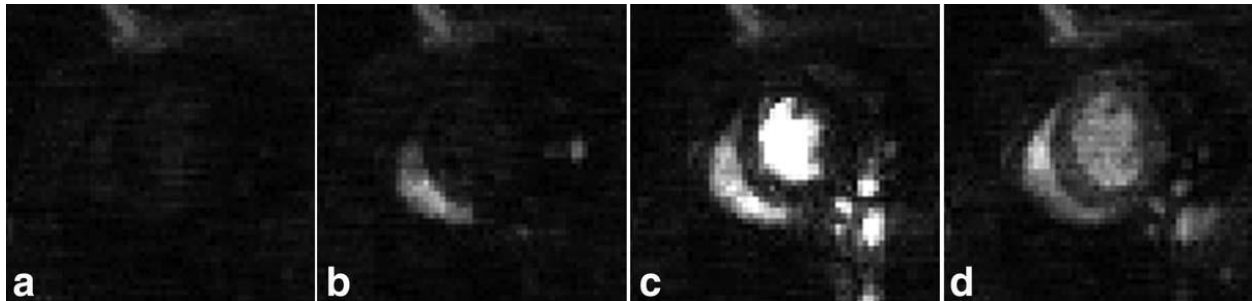


Figure 1-3. Example CS-accelerated dual-contrast first-pass MR images obtained from a mouse. Image source: Naresh, N.K., et al., Repeatability and variability of myocardial perfusion imaging techniques in mice: Comparison of arterial spin labeling and first-pass contrast-enhanced MRI. Magn Reson Med, 2015.

To quantify absolute blood flow, a measurement of the Arterial Input Function (AIF) is needed. The AIF describes the contrast agent input to the tissue of interest, and in myocardial perfusion imaging the AIF is estimated from the blood pool signal. To avoid saturation of the contrast in the AIF measurement, either a dual-contrast pulse sequence or dual-bolus protocols is used. A dual-bolus technique uses a low dose injection of the contrast agent to measure the AIF followed by a high dose contrast agent injection to measure the myocardial tissue function (TF) [124]. A dual-contrast acquisition, on the other hand, uses only one injection of high dose contrast agent. However, it measures the AIF using a short saturation delay and the TF using a longer saturation delay, as shown in Figure 1-4 [120]. To acquire both AIF and TF within one cardiac cycle at the fast heart rate of mice, compressed-sensing (CS) accelerated imaging with

k-space and time domain undersampling is used to achieve adequate spatial and temporal resolution [125].

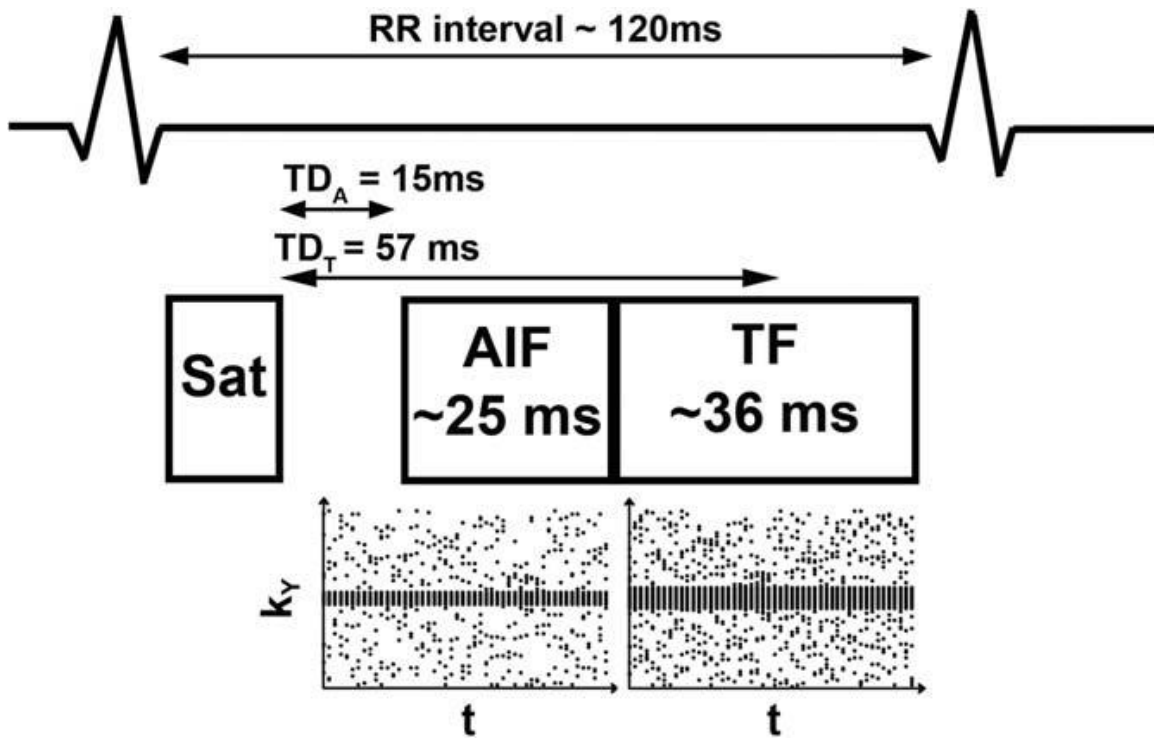


Figure 1-4. Diagram for the CS-accelerated dual-contrast first-pass MRI pulse sequence. A saturation pulse is applied after detection of the R wave, and thereafter AIF and TF are acquired at different saturation delays at TD_A and TD_T respectively. Both AIF and TF are CS-accelerated, and acquired within one cardiac cycle. Image source: Naresh, N.K., et al., Accelerated dual-contrast first-pass perfusion MRI of the mouse heart: development and application to diet-induced obese mice. *Magn Reson Med*, 2015. **73**(3): p. 1237-45. Naresh, N.K., et al., Accelerated dual-contrast first-pass perfusion MRI of the mouse heart: development and application to diet-induced obese mice. *Magn Reson Med*, 2015. **73**(3): p. 1237-45.

Example first-pass AIF and TF curves are shown in Figure 1-5 [123]. To quantify MBF, mathematical models of contrast dynamics are used, of which the Fermi deconvolution is the most common [126]. The AIF and TF curves in gadolinium concentration are calculated by first normalizing the signal intensity of blood and myocardium by that of the proton density weighted images, then converting the normalized signal intensity to T1, and finally converting T1 values to gadolinium concentrations [127]. Using this method, perfusion can also be estimated on a pixel-by-pixel level and produce perfusion maps as shown in Figure 1-5 [123].

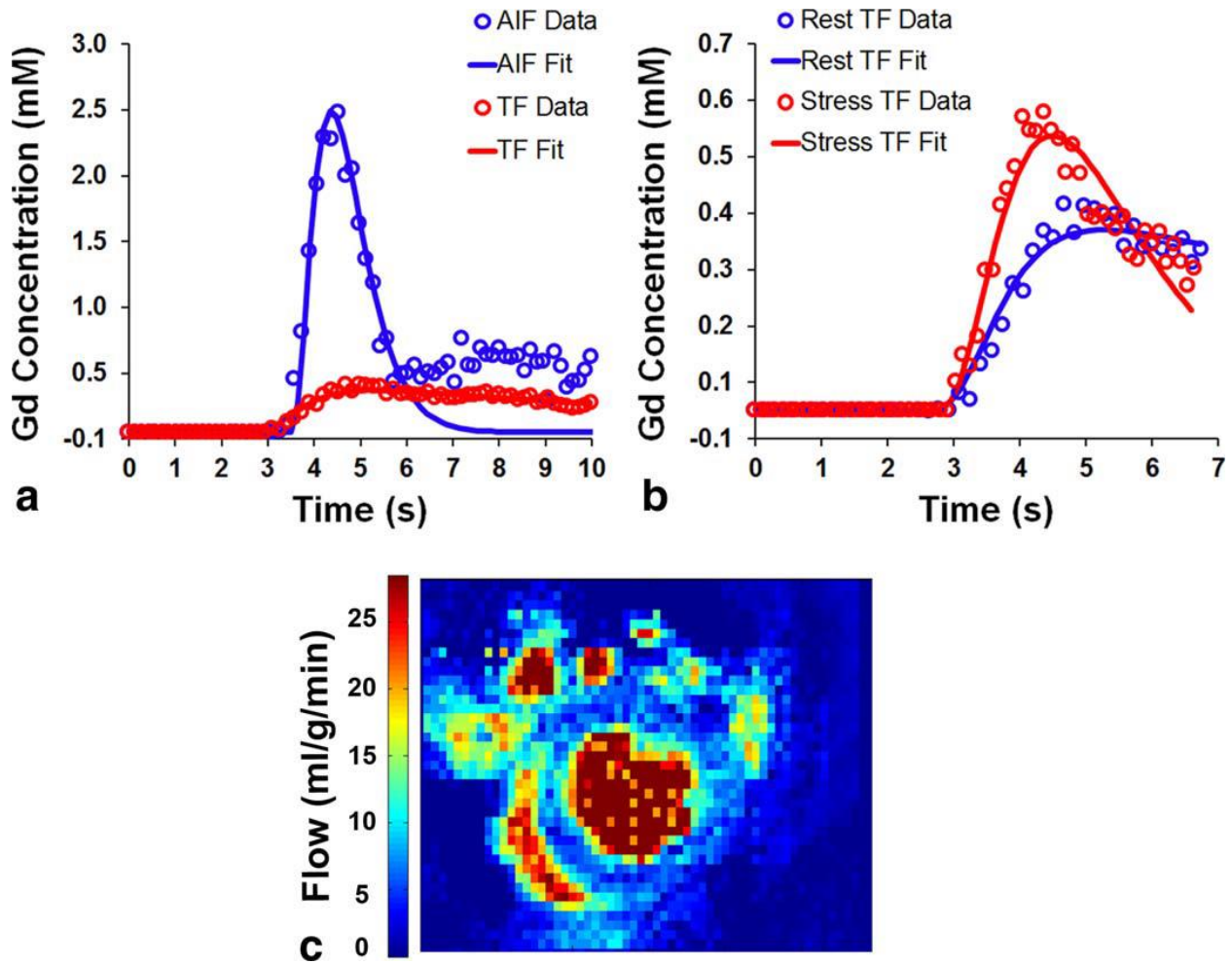


Figure 1-5. Example first-pass AIF (a) and TF (a,b) obtained from a mouse heart. Example pixel-by-pixel perfusion map obtained using first-pass MRI from a mouse at rest (c). Image source: Naresh, N.K., et al., *Repeatability and variability of myocardial perfusion imaging techniques in mice: Comparison of arterial spin labeling and first-pass contrast-enhanced MRI.* *Magn Reson Med*, 2015.

One important limitation of the first-pass contrast-enhanced MRI method is the use of gadolinium contrast agents. Gadolinium is contraindicated in patients with severely impaired renal function and can lead to organ fibrosis and failure. In mouse imaging, intravenous administration of contrast agent requires establishing an indwelling tail vein catheter, which is

time-consuming and technically challenging. Additionally, the use of contrast agent prevents perfusion to be measured continuously. Therefore, contrast-free perfusion MRI methods are needed. Another draw-back of first-pass MRI is that the mathematical modeling of contrast dynamics is relatively complex. An imaging method whose measured signal is directly proportional to perfusion would be desirable.

1.4.2 Arterial Spin Labeling (ASL) MRI

Arterial spin labeling (ASL) is an MRI technique that quantifies tissue blood flow without contrast agents. It is compatible with stress testing and can be performed repeatedly. While ASL myocardial perfusion imaging is still challenging in human, it has been performed with great success in quantifying myocardial perfusion in small animals. The key behind this ASL method is the use of radiofrequency (RF) pulses to modify the longitudinal magnetization of arterial blood, creating an endogenous tracer from the labeled blood. Images of the target tissue are acquired with and without the effect of the labeled blood. The difference between the two sets of images reflect the amount of blood flow to the target tissue. With the appropriate RF pulses, readout scheme and perfusion model, MBF can be quantitated using the ASL method.

1.4.2.1 Flow Alternating Inversion Recovery Look-Locker (FAIR-LL) ASL

Flow Alternating Inversion Recovery Look-Locker (FAIR-LL) ASL is a well-established method for quantifying myocardial perfusion in mice [128, 129]. The FAIR-LL ASL method quantifies MBF by measuring the effect of blood flow on apparent myocardial T1 relaxation. As shown in Figure 1-6 [123, 130], the FAIR-LL ASL imaging method consists of two inversion recovery measurements. In the first measurement the labeling zone is only around the imaging slice, denoted as slice-selective 'SS,' and in the second measurement the inversion is global,

denoted as nonslice-selective 'NS.' Look-Locker image acquisitions are gated to ECG R-waves and be gated to the quiescent period of respiration as well [129]. The faster heart rate in mice compared to humans is advantageous in the FAIR-LL ASL acquisition because it allows magnetization recovery to be sampled at better temporal resolution. Example images from a mouse FAIR-LL ASL scan are shown in Figure 1-6 [123, 130]. Images shown are following the SS (top) and NS (bottom) inversion pulses, and at different inversion times.

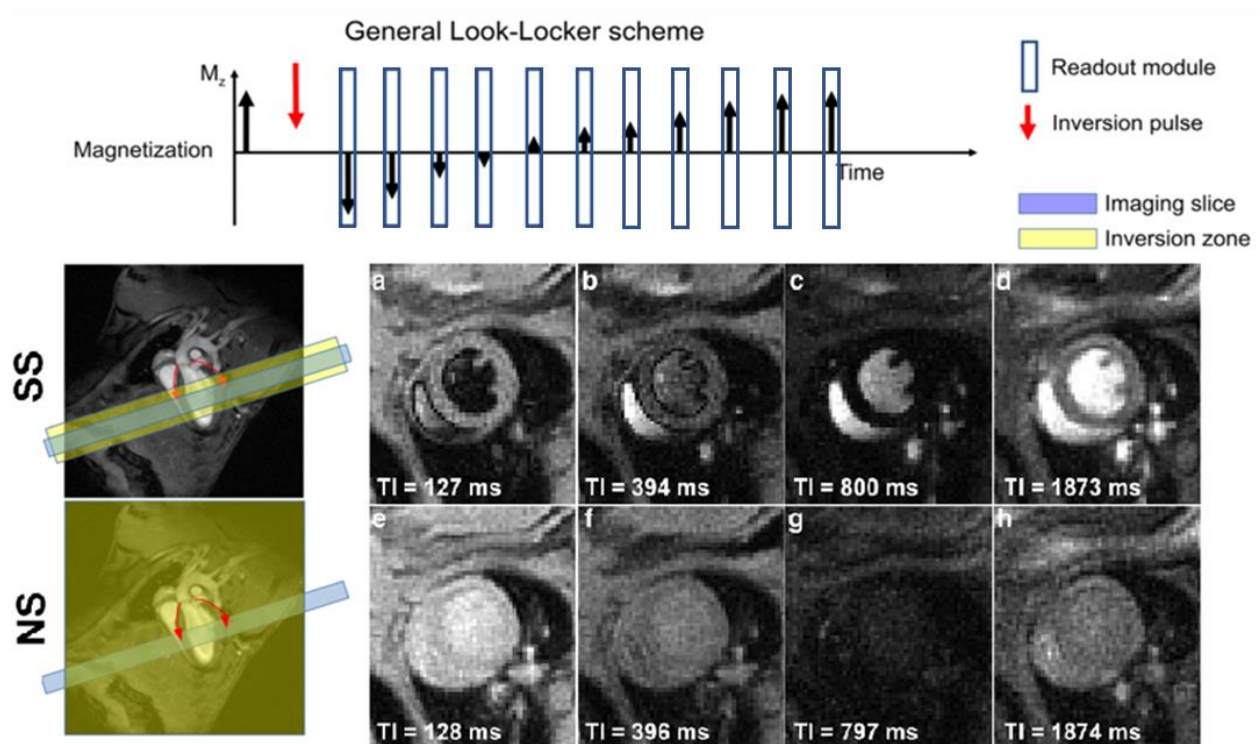


Figure 1-6. Flow Alternating Inversion Recovery Look-Locker (FAIR-LL) arterial spin labeling (ASL) imaging scheme. Example images shown are following the SS (top) and NS (bottom) inversion pulses, and at different inversion times. Image adapted from Kober, F., et al., Myocardial arterial spin labeling. *Journal of Cardiovascular Magnetic Resonance*, 2016. 18(1): p. 22. and Naresh, N.K., et al., Repeatability and variability of myocardial perfusion imaging

To quantify MBF, myocardial T1 relaxation curves following the SS and NS inversion pulse are extracted from the LL images. The shift between NS and SS T1 relaxation data depends on tissue perfusion, and the shift increases in response to vasodilatation (Figure 1-7 a ,b). Quantitatively, myocardial perfusion (P) can be calculated in units using the following equation [131]:

$$P = \frac{T_{1,NS}}{T_{1,blood}} \left(\frac{1}{T_{1,SS}} - \frac{1}{T_{1,NS}} \right) \cdot \lambda$$

Where $T_{1,NS}$ and $T_{1,SS}$ are the myocardial T1 following the NS and SS inversion pulses respectively; $T_{1,blood}$ is the blood pool T1; and the partition coefficient λ is estimated at 0.95. MBF can also be quantified using tracer-kinetic modeling [123]. Example difference curves of the NS and SS curves are shown in Figure 1-7 c. By and putting the difference curves through an ASL kinetic model, MBF and perfusion map can be calculated as shown in Figure 1-7 [123].

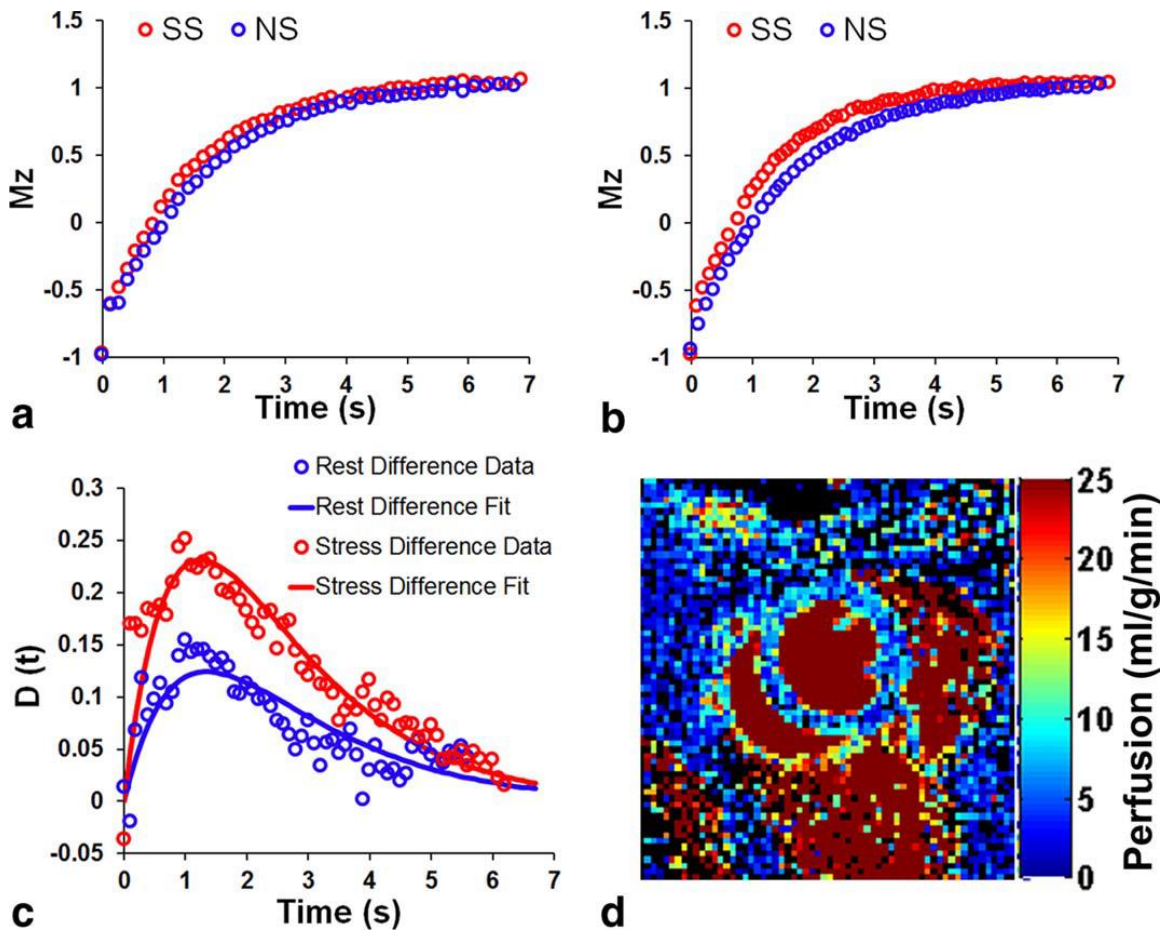


Figure 1-7. Representative T1 curves obtained from a mouse at rest (a) and stress (b) after a nonselective (blue circles) and slice-selective (red circles) inversion. (c) Example difference data and fits to the kinetic ASL model obtained from a mouse at rest (blue) and at stress (red). (d) Example pixel-by-pixel perfusion map obtained using ASL from a mouse at rest. Image source: Naresh, N.K., et al., *Repeatability and variability of myocardial perfusion imaging techniques in mice: Comparison of arterial spin labeling and first-pass contrast-enhanced MRI*.

Magn Reson Med, 2015.

One limitation of the FAIR-LL ASL method is the long scan time. The inverted myocardial magnetization takes approximately 6 to 7 seconds to recover. In order to fully sample the k-space, the inversion recovery process needs to be repeated a number of times, equal to the number of phase-encode lines or interleaves and multiply by the number of averages. As a result, the FAIR-LL ASL method has long acquisition time. For example, our standard FAIR-LL ASL protocol for mouse myocardial perfusion, if applied without acceleration, takes more than 1 hour to complete.

1.4.2.2 Steady-state Pulsed ASL (spASL)

Recently, steady-state pulsed ASL (spASL) or cine-ASL was introduced as a faster ASL method to measure MBF in mice [132]. In contrast to FAIR-LL ASL, which measure how perfusion affects the apparent T1 relaxation, spASL measures how perfusion affects the gradient echo steady state. The design of the spASL pulse sequence is show in (Figure 1-8 [132]). The basis sequence for spASL is the cine-GRE sequence. Except in one of the gradient readout, the readout part is substituted with a regional selective inversion pulse. The myocardium is imaged at steady state under two contrasts. In the first contrast called “tag,” the inversion recovery slab is strategically placed above the atria and aorta region, and as a result, blood is inverted and appears dark. In the second contrast called “control,” the inversion recovery slab is placed symmetric with respect to the short axis imaging slice, to account for any magnetization transfer effect. Under the control contrast the blood is not inverted and appears bright. The combination of steady-pulsed labeling and cine readout drives tissue magnetization into a steady state regime, and the difference of myocardial signal under these two contrasts is explicitly depends on MBF.

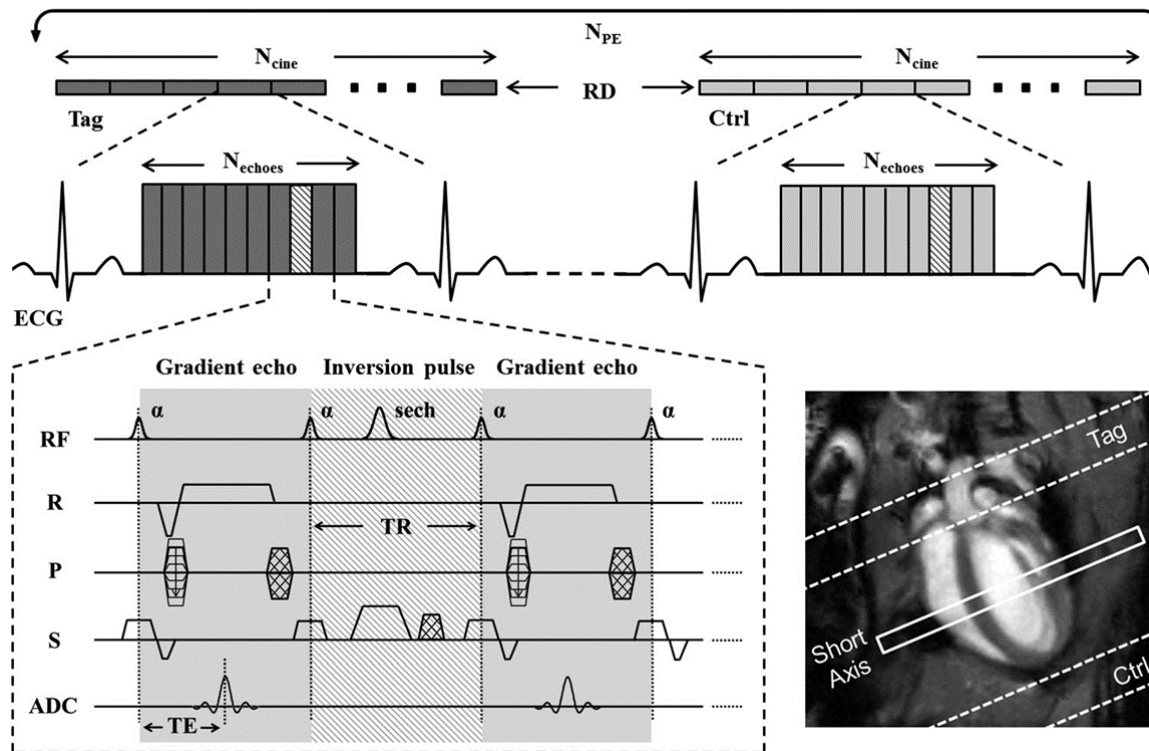


Figure 1-8. Schematic description of the original spASL pulse sequence. Image source: Troalen, T., et al., Cine - ASL: A steady - pulsed arterial spin labeling method for myocardial perfusion mapping in mice. Part I. Experimental study. Magnetic resonance in medicine, 2013. 70(5): p. 1389-1398.

The normalized myocardial signal intensity under tag and control are shown in Figure 1-9 [132]. The normalized difference between the two curves under steady state $\Delta M_{\infty}/M_{\infty}^c$ can be used to calculate myocardial blood flow with the following equation:

$$MBF = \frac{\lambda M_{SS}}{T_1^* M_0} \frac{\frac{\Delta M_{\infty}}{M_{\infty}^c}}{2\beta - \frac{\Delta M_{\infty}}{M_{\infty}^c}}$$

Where β is the blood tagging efficiency and can be estimated from the blood pool signal intensities at the two contrasts. Other parameters in the equation including λ ($\cong 0.95$), M_{SS} and T_1^* which can be estimated using the following equations

$$M_{ss} = M_0 \frac{1 - e^{-\frac{TR}{T_1}}}{1 - \cos(\alpha) e^{-\frac{TR}{T_1}}}$$

$$\frac{1}{T_1^*} = \frac{1}{T_1} - \frac{\ln(\cos(\alpha))}{TR}$$

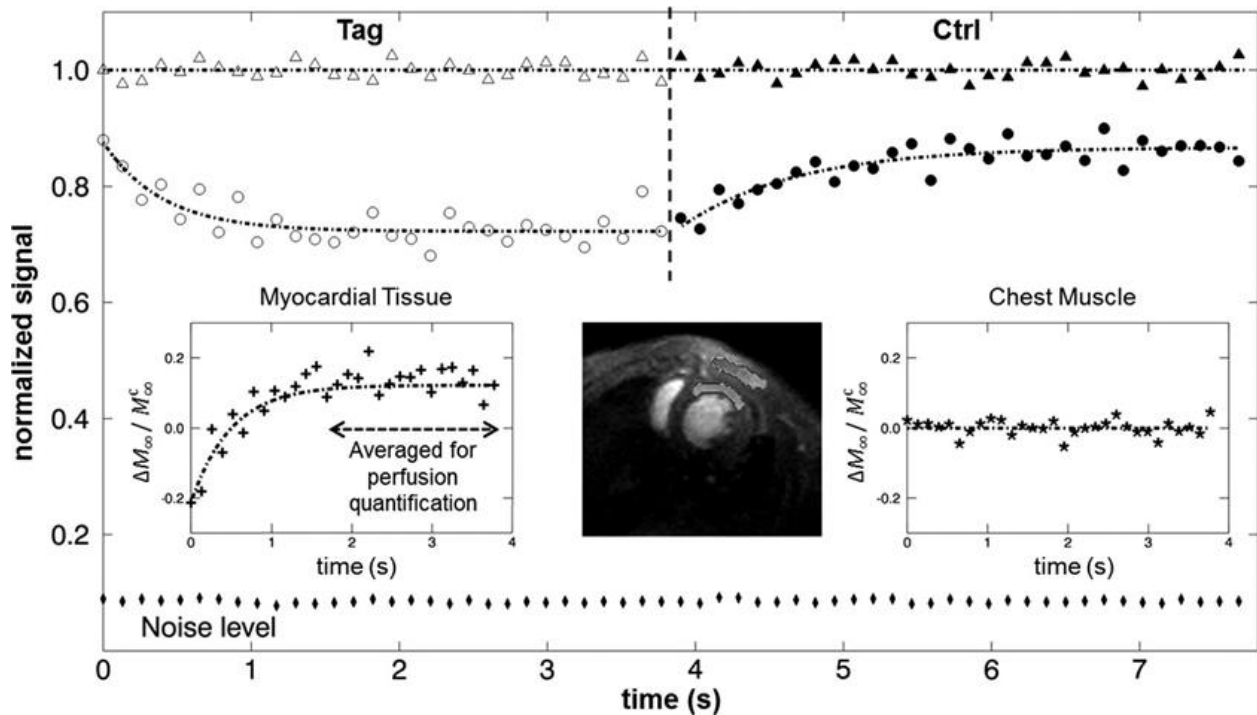


Figure 1-9. Dynamic MR signal behavior during tag and control scan of a spASL experiment
 Image source: Troalen, T., et al., Cine - ASL: A steady - pulsed arterial spin labeling method for myocardial perfusion mapping in mice. Part I. Experimental study. Magnetic resonance in medicine, 2013. 70(5): p. 1389-1398.

While the original spASL design paper proposed a very promising technique, there are opportunities to further improve upon the original design.

(1) The original spASL sequence uses a readout scheme that interleaves between the control and tag contrast. This interleaving looping structure requires re-establishment of steady-state twice for each phase encode. Since the transition to steady state is not needed for quantification, the interleaving looping structure introduced large scan inefficiencies.

(2) Respiratory motion during image acquisition introduces significant artifact. For ECG-triggered spASL, the accuracy of perfusion quantification may be especially reduced when imaging diseased animals with deeper and irregular respiratory motion, such as HFD mice or mice with myocardial infarction.

(2) The original spASL sequence is triggered by the ECG signal. As a result, depending on the heart rate variation, there is a 20 to 50 ms gap between the end of the readout train and the following ECG trigger. During this time, the myocardial magnetization deviates from the steady state due to the absence of continuous RF pulses. Since perfusion quantification depends on the steady state signal intensity, inaccurate estimation of the steady state signal would lead to inaccurate estimation of perfusion.

Thus, this dissertation seeks to address these opportunities and develop an improved spASL pulse sequence through the following specific aim:

Specific Aim 3 is to develop an improved MRI perfusion method for the mouse heart to facilitate future studies that may investigate the kinetics of impaired MPR and CMD.

Specifically, we sought to develop an improved spASL sequence that further accelerates the original spASL sequence, eliminates the gap between the readout is train and ECG trigger to allow true continuous imaging, and accounts for respiratory motion. The design and evaluation of the new sequence are summarized in [Chapter 3](#).

Chapter 2 MRI Assessment of Coronary Microvascular Endothelial Nitric Oxide Synthase (eNOS) Function using Myocardial T1 Mapping

Note: The content in chapter 2 has been published in Magnetic Resonance in Medicine and the formal publication can be accessed using the following DOI link:

Cui, S. X. and Epstein, F. H. (2018), MRI assessment of coronary microvascular endothelial nitric oxide synthase function using myocardial T₁ mapping. Magn. Reson. Med, 79: 2246-2253. doi:[10.1002/mrm.26870](https://doi.org/10.1002/mrm.26870)

2.1 Abstract

Purpose: Endothelial nitric oxide synthase (eNOS) plays a central role in regulating vascular tone, blood flow, and microvascular permeability. Endothelial dysfunction, including eNOS dysfunction, is an early biomarker of vascular disease. This study aimed to show that myocardial T1 mapping during nitric oxide synthase (NOS) inhibition could assess coronary microvascular eNOS function.

Methods: Wild-type (WT) mice, eNOS^{-/-} mice, and WT mice fed a high-fat diet (HFD) underwent T1 mapping at baseline and for 20 minutes after injection of LNAME, a NOS inhibitor. First-pass perfusion MRI was performed in WT mice at baseline and 5 minutes after LNAME injection.

Results: T1 mapping detected an increase in myocardial T1 five minutes after 4 mg/kg LNAME injection compared to baseline in control mice (T1=1515±30 ms with LNAME vs. T1=1402±30 ms at baseline, $P<0.05$). No change in myocardial T1 after LNAME injection was observed in eNOS^{-/-} mice. The change in T1 after LNAME injection was less in HFD mice ($\Delta T1=31\pm 14$ ms at 12 weeks of diet and $\Delta T1=16\pm 17$ ms at 18 weeks of diet) compared to mice fed a standard diet ($\Delta T1=113\pm 15$ ms), with $P<0.05$. First-pass MRI measured similar perfusion at baseline and 5 minutes after LNAME injection.

Conclusion: NOS inhibition causes an increase in myocardial T1 in healthy mice, and this effect is mediated through eNOS. T1 mapping during NOS inhibition detects coronary microvascular eNOS dysfunction in HFD mice. T1 mapping during NOS inhibition may be useful in preclinical studies aiming to investigate mechanisms underlying and therapies for coronary microvascular eNOS dysfunction.

2.2 Introduction

The vascular endothelium is a monolayer of cells that line the inner surface of blood vessels. Endothelial nitric oxide synthase (eNOS), an enzyme that produces nitric oxide (NO) in the vascular endothelium, plays a central role in regulating vascular properties such as tone, regional blood flow, and microvascular permeability. Cardiovascular risk factors such as obesity [133], diabetes mellitus [134] and hypertension [135] lead to excess production of superoxide or, more generally, reactive oxygen species, in the vascular wall. The resulting vascular oxidative stress leads to a process referred to as eNOS uncoupling, where eNOS dysfunction occurs, and eNOS is converted from a NO producer to a superoxide producer [136]. Under these conditions, the central roles of eNOS in endothelial function are compromised, and instead of promoting vascular health, eNOS contributes to oxidative stress and endothelial dysfunction. A minimally-invasive imaging method to assess eNOS function would enable the study of mechanisms leading to eNOS dysfunction and of potential therapies targeting eNOS, as eNOS dysfunction presently is not fully understood and there are limited therapies that promote normal eNOS function.

Prior studies have shown that pharmacological inhibition of NOS with agents such as N^G-nitro-L-arginine methyl ester (LNAME) rapidly depletes the local vessel wall NO concentration, leading to a rapid increase in microvascular permeability, protein efflux from the blood to the extracellular space, and microvascular fluid efflux [106-108, 137-139]. We hypothesized that MRI T1 mapping of the heart during NOS inhibition could detect changes in compartmental water content resulting from acute changes in microvascular permeability and fluid efflux. Furthermore, we hypothesized that these changes are mediated through eNOS and would be diminished in a disease state with eNOS dysfunction. The overall goal of this study was to show that T1 mapping during pharmacological NOS inhibition could be used to assess vascular eNOS function in the heart.

2.3 Methods

2.3.1 Experimental Design

We first sought to show that T1 mapping of the heart during NOS inhibition could detect an increase in myocardial T1. For these studies, healthy 19-week-old male wild-type (WT) C57Bl/6 mice underwent T1 mapping before and after injection of a NOS inhibitor. The pharmacological agent LNAME was chosen as the NOS inhibitor as it is tolerated by both animals [106, 138, 140, 141] and humans [142] when injected intravenously and is commercially available (Sigma-Aldrich, St. Louis, MO. Product number: N5751). LNAME was dissolved in sterile saline, and two doses of LNAME, 2 mg/kg (n = 8) and 4 mg/kg (n = 6) were tested. The bolus concentrations were 1 mg/mL and 2 mg/mL, respectively, and the total injection volume ranged from 55 to 60 μ L. The data acquisition protocol for the LNAME T1 mapping experiments is shown in Figure 2-1A.

Next, we tested the hypothesis that the change in myocardial T1 during NOS inhibition is mediated specifically through eNOS. For these studies, we performed experiments in 13-week-old male eNOS knockout (eNOS^{-/-}) mice on a C57Bl/6 background (n = 7) (Jackson Laboratory, Bar Harbor, Maine. Stock number: 002684 | eNOS KO) using the LNAME T1 mapping protocol described above and with an LNAME dose of 4 mg/kg.

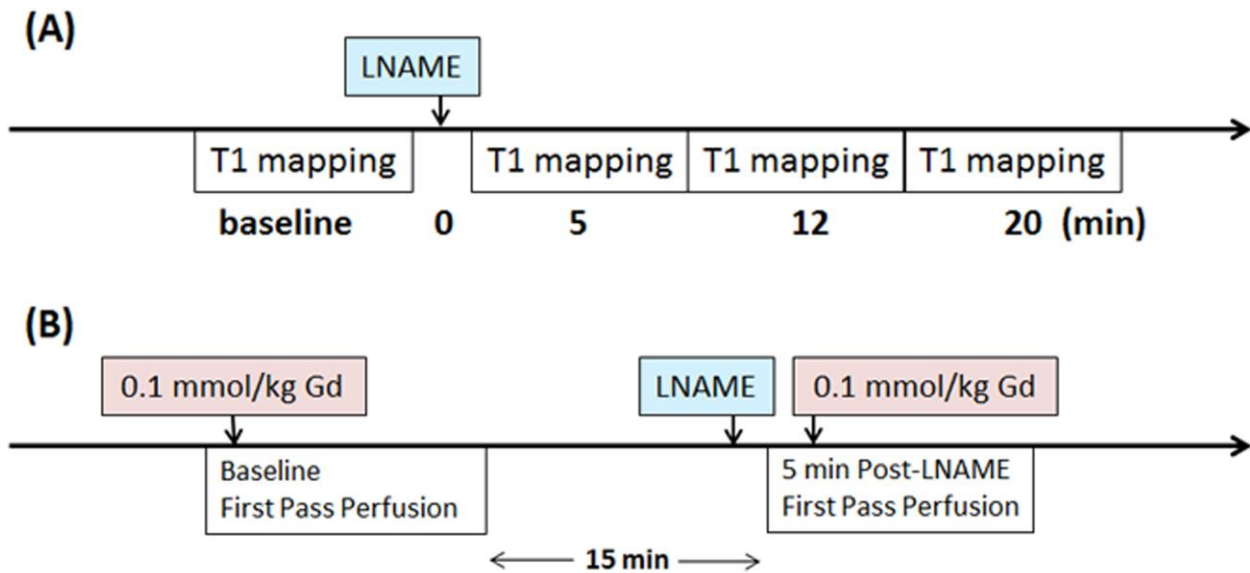


Figure 2-1. Schematic timing diagram of (A) the LNAME T1 mapping experiments, and (B) the LNAME first-pass perfusion experiments.

Previous studies have shown that pharmacological agents such as adenosine that cause vasodilation and changes in vascular tone and perfusion can also cause a detectable increase in myocardial T1 [143]. To exclude the possibility that increases in myocardial T1 during NOS inhibition may be due to potential vasodilatory effects, we measured myocardial perfusion at baseline and during NOS inhibition using gadolinium-enhanced first-pass perfusion MRI [120] in male WT control mice (n = 6). As shown in the data acquisition protocol for the LNAME first-pass perfusion experiments (Figure 2-1B), baseline and post-LNAME first-pass perfusion images were acquired within the same imaging session, and each used a 0.1 mmol/kg dose of Gd-DTPA. The bolus concentration of Gd solution was 0.05 M. The total injection volume, which included two injections of Gd solution and one injection of LNAME solution, ranged from 160 to 180 μ L. A 15-minute waiting period between first-pass measurements was employed to allow contrast agent wash out. Post-LNAME perfusion was measured 5 minutes after intravenous injection of LNAME to match the timing of the LNAME T1 mapping experiment.

Finally, we sought to show that LNAME T1 mapping could detect eNOS dysfunction in a mouse model of cardiac microvascular disease. For the disease model, we chose male C57BL/6 mice fed a high-fat diet (HFD), as this model exhibits hallmarks of diabetic cardiomyopathy [144, 145], and has previously been shown to develop coronary endothelial dysfunction [146-148]. To test the hypothesis that T1 mapping with NOS inhibition can detect coronary microvascular eNOS dysfunction in HFD mice, mice underwent HFD feeding (60% calories from fat, Diet 12492, Research Diets Inc., New Brunswick, NJ) for 12 (18-week-old, n = 10) and 18 weeks (24-week-old, n=10), and at each time point MRI T1 mapping with 4 mg/kg LNAME was performed. The LNAME solution injection volume ranged from 65 to 110 μ L.

2.3.2 Animal Handling

All animal studies were performed under protocols that comply with the Guide for the Care and Use of Laboratory Animals (NIH publication no. 85-23, Revised 1996) and were approved by the Animal Care and Use Committee at our institution. An indwelling tail vein catheter was established to deliver LNAME (Sigma-Aldrich Biotechnology, St Louis, MO, USA) and/or Gd-DTPA (Magnevist, 0.1 mmol/kg body weight) during MRI. Body temperature was maintained at $36 \pm 0.5^{\circ}\text{C}$ using circulating warm water, and anesthesia was maintained using 1.25% isoflurane in O_2 during MRI.

2.3.3 MRI Acquisitions

MRI was performed on a 7T Clinscan system (Bruker, Ettlingen, Germany) using 30-mm or 35-mm diameter birdcage RF coils and an MR-compatible physiological monitoring and gating system for mice (SA Instruments, Inc., Stony Brook, NY). The larger diameter RF coil was used

when necessary to accommodate the heavier HFD mice. Localizer imaging was performed to select a mid-ventricular short-axis slice.

T1 mapping MRI was performed using a spiral Look-Locker T1-mapping method for mice combined with cardio-respiratory gating, as previously described [123]. The technique uses fuzzy-clustering of spiral k-space interleaves [129] to ensure accurate T1 estimation even with varying respiratory or heart rate. Imaging parameters included: TR = 7 s, TE = 0.67 ms, flip angle = 3°, field of view (FOV) = 30 x 30 mm², number of averages = 3, number of spiral interleaves = 84, interleaves per heartbeat = 3 and in-plane resolution = 0.23 x 0.23 mm². Using k_y-t undersampling with randomness and a low-rank compressed-sensing reconstruction [125], the acquisition was rate-2 accelerated, providing a scan time of 7 minutes.

First-pass gadolinium-enhanced MRI was performed using a dual-contrast saturation-recovery sequence with k_y-t undersampling and a motion-compensated compressed sensing reconstruction algorithm as recently described [120]. Briefly, a saturation pulse is applied after detection of the ECG R-wave and thereafter two slices are acquired in each cardiac cycle: the arterial input function (AIF) and the tissue function (TF). Imaging parameters included: TR = 2.1 ms, TE = 1.2 ms, FOV = 28x11 mm², base resolution = 128, phase resolution = 80%, image resolution = 0.27 x 0.22 mm², excitation flip angle = 15°, slice thickness = 1 mm, number of frames = 300, acceleration rate = 2, AIF saturation delay = 24 ms with centrically-ordered phase encoding, and TF saturation delay = 84 ms with linearly-ordered phase encoding. Twenty phase-encode lines were acquired for each AIF image and 20 lines were acquired for each TF image. Contrast agent was injected intravenously 10 seconds after the start of the first-pass acquisition. Proton density weighted images were acquired at the end of the acquisition to normalize signal intensities for perfusion analysis. All imaging parameters were kept the same for proton density weighted image acquisitions compared to the saturation recovery portion of

the image acquisition, except that no saturation pulse was applied upon detection of the ECG R-wave and a flip angle of 5° was used.

2.3.4 Image analysis

Image reconstruction and analysis were performed in MATLAB (Mathworks, Natick, MA). Undersampled T1 mapping and first-pass perfusion images were reconstructed using Block LOw-rank Sparsity with Motion-guidance (BLOSM) [125]. For the respiratory-gated T1 mapping images which did not suffer from respiratory motion, BLOSM motion guidance was not used and a single block covering the entire image was used, such that the BLOSM reconstruction reduced to a simple low-rank reconstruction method. To quantify myocardial T1, regions of interest (ROIs) for the myocardium were drawn manually and included the entire left-ventricular myocardial area within a slice using conservative delineation of the endocardial and epicardial borders. Signal intensity-time curves were fitted to the following equation: $M_z(t) = M_o + (M_z(0) - M_o) \exp(-t/T1)$. An optimal fit of the model parameters M_o , $M_z(0)$ and $T1$ was obtained by minimizing the mean squared error. To quantify myocardial blood flow (MBF), perfusion analysis was performed as previously described [120]. Briefly, ROIs for blood and myocardium were drawn, and signal intensity was normalized by proton density weighted images. Normalized signal intensity was converted to T1 and T1 was converted to gadolinium concentration using methods described by Cernicanu and Axel [127], and MBF was quantified using Fermi deconvolution [126].

2.3.5 Statistical Analysis

Statistical analyses were performed using SigmaPlot (Systat Software Inc., Point Richmond, CA). Changes in myocardial T1 and absolute MBF were analyzed for various experimental

groups of mice at various time points using analysis of variance (ANOVA) and the t-test, as appropriate. All values in the text, tables and graphs are presented as mean \pm standard error.

2.4 Results

2.4.1 NOS inhibition causes an increase in myocardial T1

Intravenous administration of 2 mg/kg and 4 mg/kg LNAME caused a significant decrease in heart rate in control mice (Figure 2-2). The results of our studies performing T1 mapping after infusion of LNAME in WT mice are shown in Figure 2-3. The average area of the myocardial ROIs among all mice was 134 ± 4 pixels or 7.1 ± 0.2 mm². An example showing the T1 lengthening effect of NOS inhibition is shown in Figure 2-3B and C where the R1 (R1 = 1/T1) map 5 minutes after injection of 4 mg/kg LNAME (Figure 2-3C) shows a reduction in myocardial R1 compared to baseline (Figure 2-3B). The same data displayed as myocardial T1 relaxation curves prior to and 5 minutes post LNAME injection illustrate the quality of the Look-Locker measurement data and also show the T1-lengthening effect of LNAME (Figure 2-3D). Figure 2-3E summarizes data from all mice and shows that T1 mapping after the injection of LNAME detected a transient increase in T1, as T1 was elevated at 5 minutes post injection (T1 = 1515 ± 30 ms with 4 mg/kg LNAME vs. T1 = 1402 ± 30 ms at baseline, $P < 0.05$). T1 decreased toward its baseline value at 20 minutes after injection. Two-way ANOVA also showed that myocardial T1 measured 5 minutes after a 4 mg/kg LNAME injection was significantly greater than T1 measured 5 minutes after a 2 mg/kg LNAME injection ($P < 0.05$).

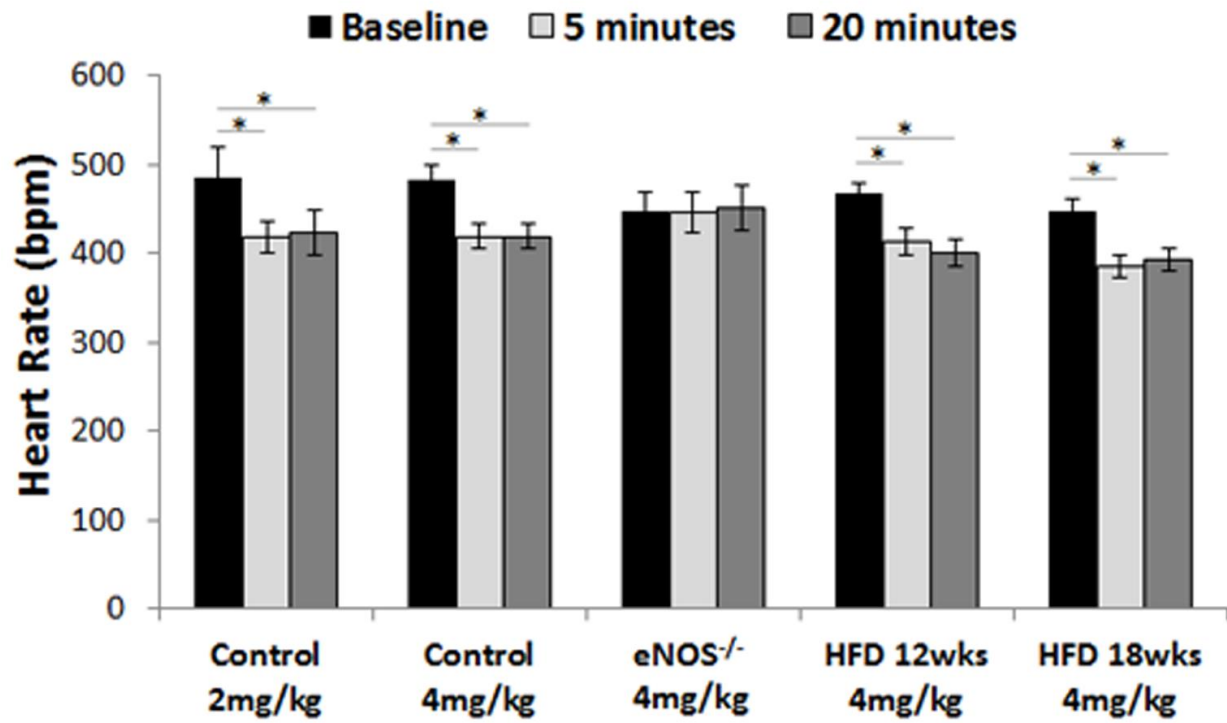


Figure 2-2. Intravenous administration of 2mg/kg and 4mg/kg LNAME caused a significant decrease in heart rate in control mice (* $P < 0.01$). 4mg/kg LNAME also caused a significant decrease in heart rate in HFD mice but not in eNOS^{-/-} mice.

WT

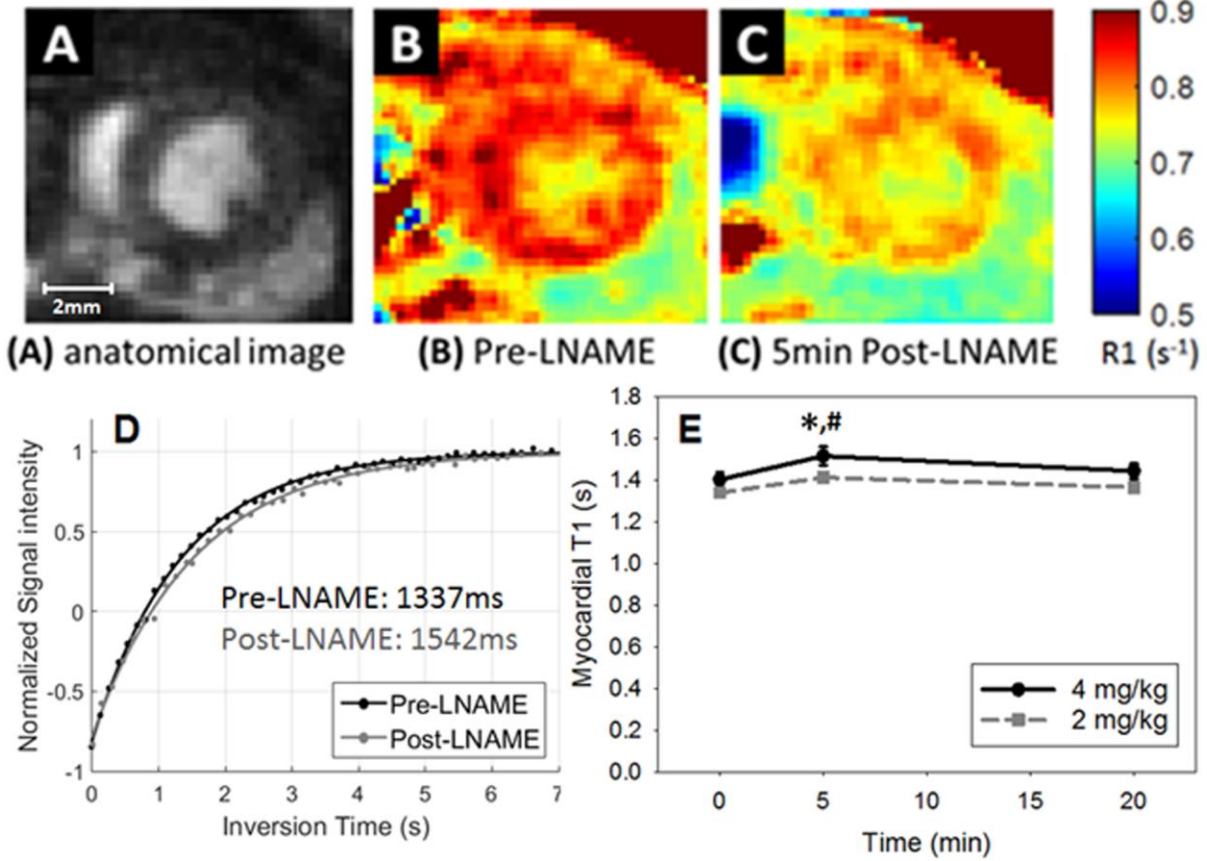


Figure 2-3(A) Example anatomical image used to visualize myocardial borders. R1 maps of the heart acquired before (B) and 5 minutes after injection of 4 mg/kg LNAME (C), demonstrating the decrease in R1 observed in response to NOS inhibition. (D) Example myocardial T1 relaxation curves prior to and 5 minutes after 4 mg/kg LNAME. (E) The time course of myocardial T1 after intravenous injection of LNAME at two doses is shown. Myocardial T1 measured five minutes after 4 mg/kg LNAME injection was higher than at baseline (* $P < 0.05$) and was higher than 5 minutes after 2mg/kg LNAME (# $P < 0.05$).

2.4.2 The LNAME-induced myocardial T1 increase is mediated through eNOS

In our second set of experiments, we performed LNAME T1 mapping in eNOS^{-/-} mice. Intravenous administration of 4mg/kg LNAME caused no change in heart rate in eNOS^{-/-} mice (Figure 2-2). As shown in Figure 2-4, no difference was observed in R1 maps of an example eNOS^{-/-} mouse between baseline (Figure 2-4B) and after LNAME injection (Figure 2-4C). The graph shown in Figure 2-4D summarizes the results of T1 mapping after 4 mg/kg LNAME in WT and eNOS^{-/-} mice, showing that while LNAME caused a significant and transient increase in myocardial T1 in WT mice, the effect was completely blunted in eNOS^{-/-} mice.

eNOS^{-/-}

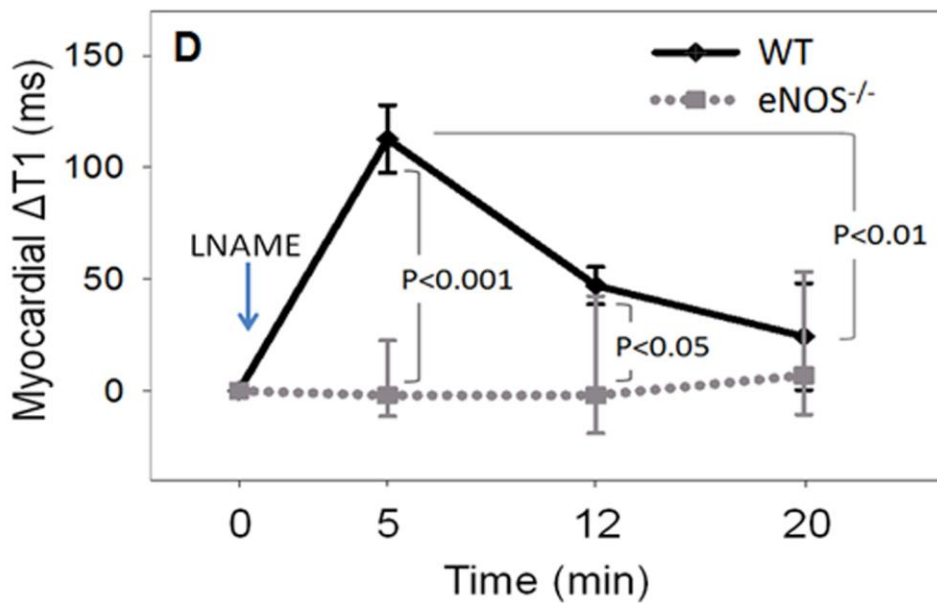
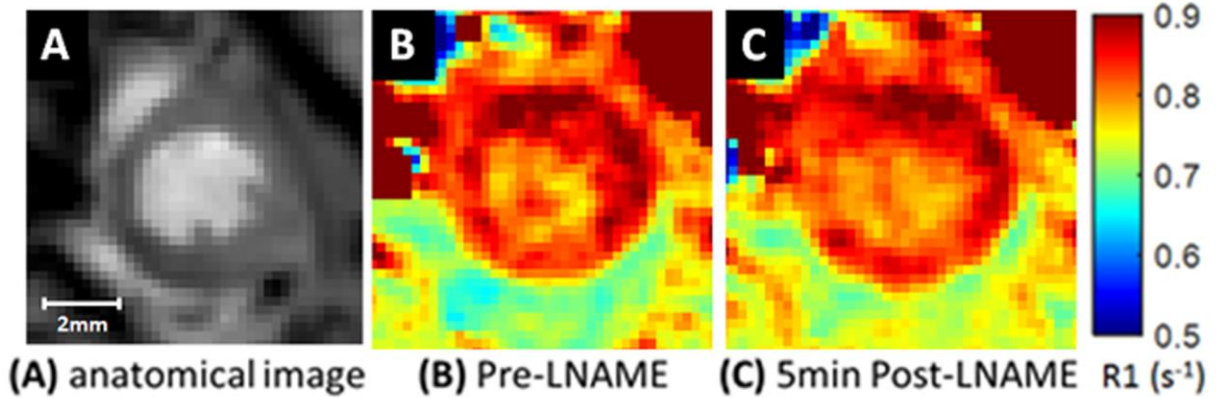


Figure 2-4. NOS inhibition with 4 mg/kg LNAME caused a significant transient increase in myocardial T1 in WT mice but not in *eNOS*^{-/-} mice. An example anatomical image used to visualize myocardial borders is shown in (A). R1 maps of the heart of *eNOS*^{-/-} mice acquired before and 5 minutes after injection of 4 mg/kg LNAME are shown in (B) and (C), respectively. The time course of the change in myocardial T1 after intravenous injection of LNAME is shown in (D) for WT and *eNOS*^{-/-} mice.

2.4.3 Myocardial perfusion does not change with LNAME

Data from first-pass perfusion MRI acquired at baseline and after 4 mg/kg LNAME injection are shown in Figure 2-5. Specifically, Figure 2-5A shows example AIF and TF curves from baseline and during NOS inhibition in one mouse. Both the AIFs and TFs are similar at baseline and 5-minutes after LNAME. Figure 2-5B summarizes the results from all LNAME perfusion data showing that first-pass MRI in WT mice measured similar perfusion at baseline (6.2 ± 0.4 ml/g/min) and 5 minutes after LNAME (6.1 ± 0.6 ml/g/min), suggesting no vasodilatory effects ($P = \text{NS}$).

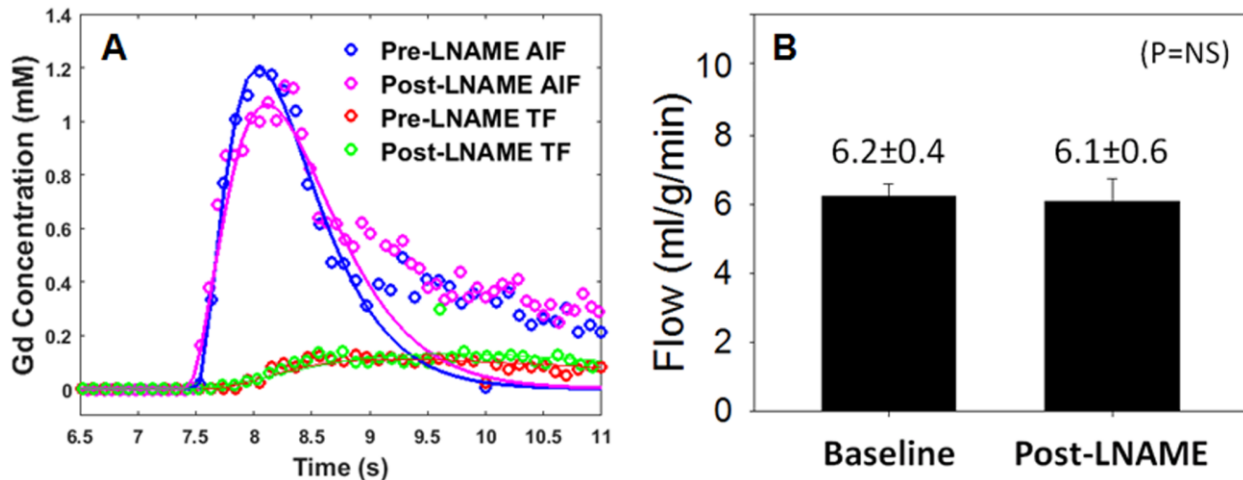


Figure 2-5. Myocardial perfusion is similar before and after LNAME injection. Example arterial input function (AIF) and tissue function (TF) curves from pre- and post-LNAME acquisitions (A). Myocardial perfusion was 6.2 ± 0.4 ml/g/min at baseline and 6.1 ± 0.6 ml/g/min after LNAME (B).

2.4.4 LNAME T1 mapping detects eNOS dysfunction in HFD mice

Body weight was significantly higher in the HFD mice at 12 and 18 weeks post-diet and it progressively increased with time (Figure 2-6). Intravenous administration of 4mg/kg LNAME caused a significant decrease in heart rate in mice fed an HFD for 12 and 18 weeks (Figure 2-2). The LNAME T1 mapping results from mice fed an HFD compared to controls are shown in Figure 2-7. Specifically, example R1 maps from an HFD mouse after 18 weeks of diet show no observable change in R1 when comparing the baseline (Figure 2-7B) and post-LNAME R1 maps (Figure 2-7C). A bar graph summarizing myocardial $\Delta T1$ results (T1 measured 5 minutes after LNAME injection minus T1 at baseline) is shown in Figure 2-7D for WT and HFD mice. These measurements detected a significant difference in $\Delta T1$ for mice fed an HFD for 12 and 18 weeks compared to mice fed a control chow diet ($P < 0.01$).

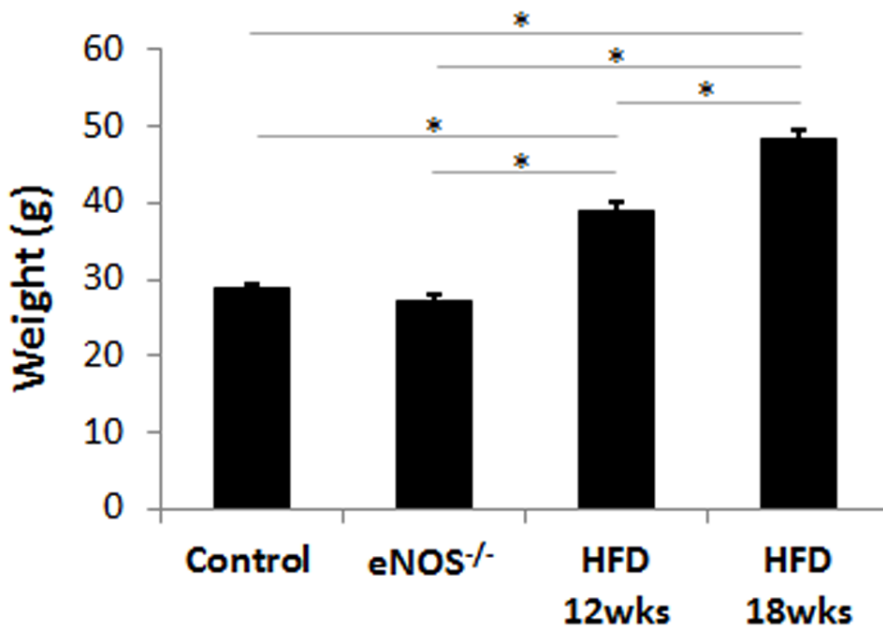


Figure 2-6. Body weight was significantly higher in the HFD mice at 12 and 18 weeks post-diet and it progressively increased with time (* $P < 0.01$).

HFD 18 wks

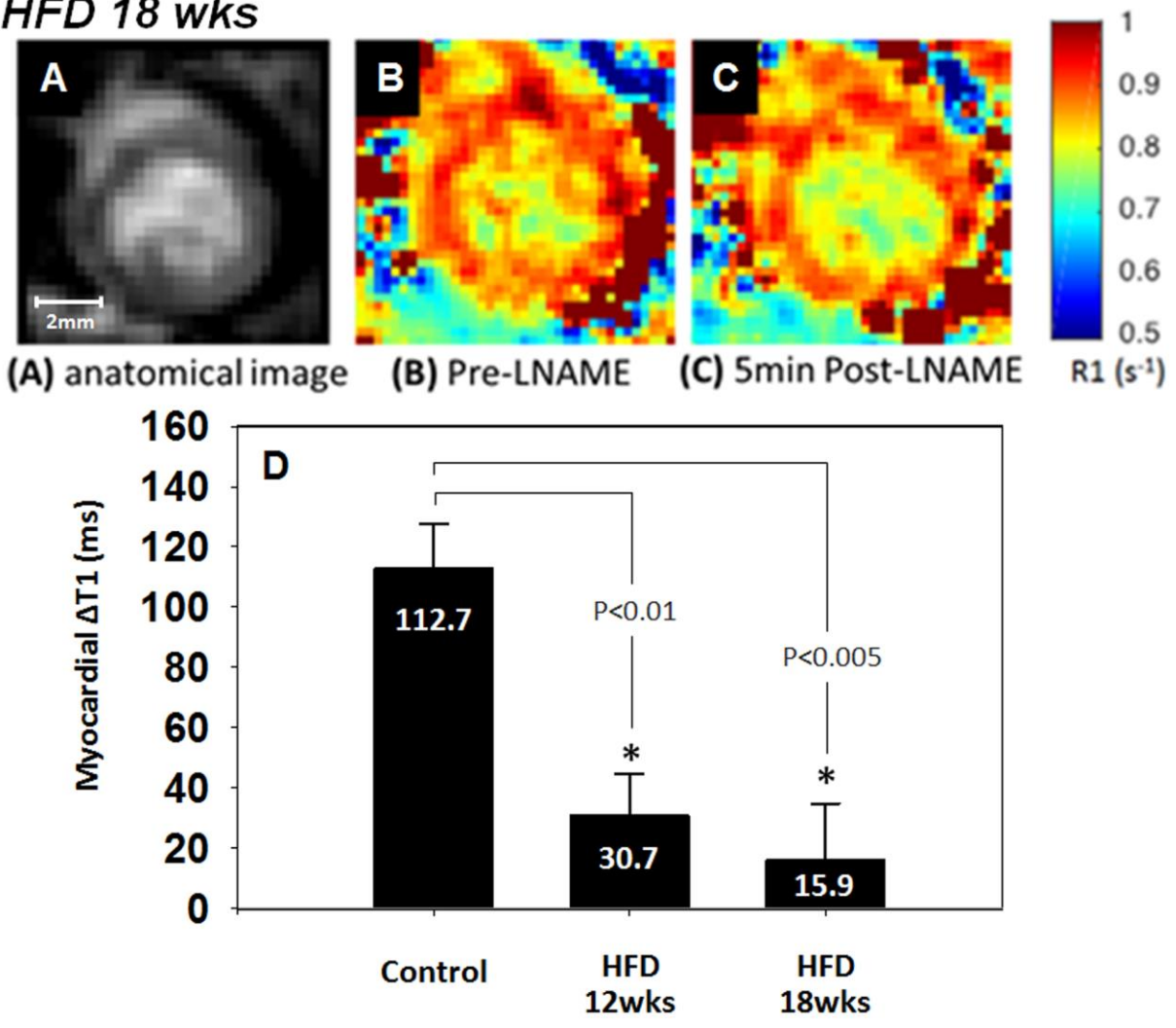


Figure 2-7. Anatomical image (A), pre-LNAME R1 map (B), and post-LNAME R1 map (C) of a mouse 18 weeks after initiation of a high-fat diet (HFD). One-way ANOVA detected significant differences in the change of myocardial T1 assessed five minutes after LNAME injection between the HFD groups and the control mice fed a standard chow diet (D).

2.5 Discussion

The major finding of this study is that an increase in myocardial T1 during NOS inhibition is a marker of coronary microvascular endothelial function, or, more specifically, of coronary microvascular eNOS function. Others have previously sought to image coronary endothelial function. For example, Hays et al. showed that coronary artery cross-sectional area and blood flow before and during isometric handgrip exercise could be used to assess coronary endothelial function [104]. The present method uniquely probes the effect of inhibiting NOS on coronary microvascular permeability and, as demonstrated by the experiments in eNOS^{-/-} mice, the effect was shown to be specifically mediated by eNOS. Thus, this method uses imaging to noninvasively probe the function of an enzyme that plays a key role in normal vascular physiology and in coronary microvascular pathophysiology.

In our experiments, we injected a bolus of LNAME and observed the system kinetics by imaging before and serially after the injection. The increase in myocardial T1 observed at 5 minutes after LNAME injection is consistent with prior literature where light and electron microscopy detected opening of interendothelial junctions (IEJ) within a few minutes of injecting LNAME [138]. In the same study, it was also observed that the response to LNAME on IEJ opening lasted longer than 30 minutes, which is longer than the transient effect of LNAME on myocardial T1 that we observed. This difference may be due to the higher dose of LNAME that was used in the IEJ experiment (30 mg/kg vs. 4 mg/kg), or due to the *ex vivo* context of the IEJ study as compared to our *in vivo* experiments. The return of T1 toward baseline that we observed at 20 minutes after LNAME injection is likely due to clearance by the lymphatic system, and the time course of our results is consistent with prior studies showing that acute edema causes gradual and significant elevation in the lymphatic flow rate within 30 minutes in the pulmonary [149, 150] and mesenteric lymphatic systems [151].

Prior studies show that endothelial dysfunction is an early biomarker of vascular disease [84-89]. In the present study, we detected coronary microvascular eNOS dysfunction at 12 and 18 weeks of HFD. Previously we showed that myocardial perfusion reserve is impaired in HFD mice at 18 weeks of diet, but not at 12 weeks of diet [145]. Thus, our imaging methods show that coronary microvascular eNOS dysfunction precedes impairment of myocardial perfusion reserve, which is consistent with the current understanding of the progression of coronary vascular disease in HFD mice.

Others have applied myocardial T1 mapping after the infusion of adenosine and observed an increase in T1 [143]. As adenosine is a vasodilator that increases blood flow and blood volume, that effect is attributed to vasodilation and an increase in myocardial blood volume. Our first-pass gadolinium-enhanced MRI experiments showed no change in myocardial blood flow. Also, LNAME is known to cause vasoconstriction. Given these results, it is unlikely that our observations of increased myocardial T1 after injection of LNAME are due to an increase in blood volume.

Our method probes microvascular eNOS function. In addition to the roles of eNOS in vasodilation, blood flow, and microvascular permeability, eNOS also plays important roles in inhibition of platelet aggregation and adhesion to the vascular wall [152-154], an early event in the development of atherosclerosis, suppression of vascular smooth muscle cell proliferation [155-157], and modulation of leukocyte-endothelial interactions [158-160]. Thus, methods to noninvasively assess eNOS function may be used in the future to shed light on the roles of microvascular eNOS in normal physiology and with regard to its various roles and functions.

Therapies that may prevent or treat eNOS dysfunction includes bone marrow cell treatment [161, 162], gene therapy [163, 164], drugs targeting the renin-angiotensin-aldosterone system [141, 165, 166], and statins [167]. LNAME T1 mapping may be a useful method to test whether therapeutic agents promote improved eNOS function.

The present study had several limitations. In order to keep the total anesthesia time under two hours, we did not acquire whole-heart cine images, which would have provided heart weight and global left-ventricular function data. LNAME causes an increase in blood pressure [106]. Even though NOS inhibition with intravenous LNAME has been used previously for human imaging studies [142], the side effect of increased blood pressure is not conducive to routine use in human subjects. Nonetheless, this method may be useful for preclinical studies that investigate mechanisms underlying and therapies for coronary microvascular endothelial dysfunction. The method was well tolerated in serial MRI sessions in anesthetized mice. While we showed that coronary microvascular endothelial dysfunction precedes impaired myocardial perfusion reserve in HFD mice, we did not determine the earliest time point where coronary microvascular endothelial dysfunction can be detected in this disease model. Future studies may seek to more precisely determine the time of onset of coronary microvascular endothelial dysfunction in HFD mice. We employed myocardial T1 mapping but not T2 mapping. The latter measurements would provide useful data, however the data acquisition times for current myocardial T2 mapping sequences for mice [168, 169] are long compared to the timing of changes in myocardial relaxation times after LNAME injection, which precluded the acquisition of these data. By applying better acceleration methods, T2 maps may be acquired in the future.

Chapter 3 Self-gated spASL: Improved Steady-Pulsed Arterial Spin Labeling using Retrospective Cardiac and Self-Navigated Respiratory Gating with Faster Looping Structure for Quantification of Myocardial Perfusion in Mice

3.1 Abstract

Background: Myocardial perfusion MRI in mice is used to investigate mechanisms underlying and therapies for impaired perfusion and myocardial perfusion reserve (MPR). Mice fed a high-fat diet (HFD) recapitulate characteristics of human obesity and diabetes with reduced MPR in the absence of significant coronary artery disease. Flow Alternating Inversion Recovery Look-Locker (FAIR-LL) arterial spin labeling (ASL) is a well-established contrast-free method for quantifying myocardial perfusion in mice. Recently, steady-state pulsed ASL (spASL) was introduced as a faster and more sensitive perfusion method. We sought to implement an improved spASL sequence that further accelerates the original spASL sequence, eliminates the gap between the readout train and ECG trigger to allow true continuous imaging, and accounts for respiratory motion.

Methods: A self-gated spASL sequence was developed on a small-bore 7 Tesla system. The self-gated spASL uses a sequential looping structure to reduce readout inefficiency, real-time retrospective ECG gating to allow true continuous imaging and self-navigated respiratory gating to account for breathing motion. To evaluate the new sequence, self-gated spASL and FAIR-LL ASL were performed and repeated in control and HFD mice (n=7 each). Acquisition time for self-gated spASL was 5 minutes and 15 minutes for FAIR-LL ASL. Raw data from the spASL acquisitions were reconstructed with and without respiratory gating to demonstrate the effect of self-gating. Global and segmental myocardial perfusion, perfusion map spatial variability, and repeatability were quantified to compare self-gated spASL and FAIR-LL ASL.

Results: Retrospective self-navigated respiratory gating improves myocardial boundary definition and reduces partial volume in spASL. Self-gated spASL measured lower myocardial perfusion than spASL without respiratory gating in HFD mice at 4.5 ± 0.8 and 5.4 ± 1.1 ml/g/min, respectively, but no significant difference in control mice at 4.8 ± 0.9 and 5.3 ± 1.0 ml/g/min. Self-

gated spASL measured lower perfusion than FAIR-LL ASL and provided lower pixel-wise and segmental-wise variability, and it also showed better repeatability in quantifying myocardial perfusion than FAIR-LL ASL.

Conclusions: The spASL sequence with sequential looping structure is faster than interleaved spASL. Self-navigated respiratory gating is more important when quantifying perfusion in HFD mice as it significantly reduces the partial volume effect. Compared to FAIR-LL, in one-third of the scan time, self-gated spASL provided less variability and better repeatability in quantifying perfusion in mice while maintaining the same spatial resolution. Measurements of absolute perfusion were different for self-gated spASL and FAIR-LL. With no gold standard, it is unknown which method is more accurate. However, reduced variability and repeatability is important because it provides more statistical power for hypothesis testing. Self-gated spASL may outperform FAIR-LL ASL for quantitative myocardial perfusion MRI in mice.

3.2 Backgrounds

Assessing myocardial perfusion or myocardial blood flow (MBF) is central to the evaluation of ischemic heart disease. Myocardial perfusion is markedly reduced following myocardial infarction [170]. While late gadolinium enhanced imaging (LGE) can identify the location and size of the infarct, quantitative myocardial perfusion mapping has the unique ability to quantify reperfusion of injured tissue and evaluate therapies that enhance infarct healing or cardiac regeneration processes. Myocardial perfusion reserve (MPR) is the ratio of perfusion at stress over rest. MPR is reduced due to angina or coronary microvascular disease (CMD) [171]. While there are no established disease mechanisms and treatment for CMD, CMD has a high prevalence in women [172, 173] and patients with obesity [174], diabetes [175], and metabolic syndrome [176]. There is a strong need to translate current molecular, cellular, and physiological knowledge into new therapeutic options.

Mouse models of human cardiovascular diseases provide platforms to study the mechanisms underlying and test therapies for impaired perfusion and perfusion reserve [128, 170, 172, 177]. Mice fed a high-fat diet (HFD) recapitulate key characteristics of human obesity and diabetes with reduced MPR in the absence of significant coronary artery disease, showing glucose intolerance, endothelial dysfunction, increased LV mass, decreased MPR with no aortic plaque, and interstitial fibrosis [145, 178].

Flow Alternating Inversion Recovery Look-Locker (FAIR-LL) arterial spin labeling (ASL) is a well-established method for quantifying myocardial perfusion in mice [128, 129, 177, 179]. The FAIR-LL ASL method measures perfusion by quantifying the effect of blood flow on apparent myocardial T1 relaxation. The method consists of two inversion recovery measurements, one following a slice-selective inversion pulse and one following a global inversion pulse. The inverted myocardial magnetization takes approximately 6 to 7 seconds to

recover. To fully sample the k-space, the inversion recovery process needs to be repeated the same number of times as the number of phase encode lines or interleaves. As a result, the FAIR-LL ASL requires long acquisition times.

Recently, steady pulsed ASL (spASL), also known as cine-ASL, was introduced as a faster and more sensitive method to measure perfusion [132, 180, 181]. In contrast to FAIR ASL, spASL measures perfusion by quantifying the effect of blood flow on gradient echo steady state. The basis of the spASL sequence is the cine-GRE sequence; nonetheless, in one of the TR's towards end systole, the readout part is substituted with a regional selective inversion pulse. The evenly spaced cine-readout RF pulses drive the myocardium into a steady state. To measure perfusion, the myocardium is imaged at steady state under two different contrasts. In the first contrast, called tag, the inversion recovery slab is strategically placed above the atria and aorta region; this causes the blood to be inverted and appear dark. In the second contrast, called control, the inversion recovery slab is placed symmetrically with respect to the short axis imaging slice to account for any magnetization transfer effect. Under the control contrast, the blood is not inverted and appears bright. The difference in myocardial steady state signal under the two contrasts explicitly depends on perfusion [182].

Our goals for this study were to develop an improved spASL sequence that further accelerates the original spASL sequence, eliminates the gap between the readout train and ECG trigger to allow true continuous imaging, and accounts for respiratory motion. The original spASL sequence [132] uses a readout scheme that interleaves between the control and tag contrast. This interleaving looping structure requires the re-establishment of steady-state twice for each phase encode. Since the transition to steady state is not needed for quantification, the interleaving looping structure introduced large scan inefficiencies. The original spASL sequence is triggered by the ECG signal. As a result, depending on the heart rate variation, there is a 20

to 50 ms gap between the end of the readout train and the following ECG trigger. During this time, the myocardial magnetization deviates from the steady state due to the absence of continuous RF pulses. Since perfusion quantification depends on the steady state signal intensity, inaccurate estimation of the steady state signal would lead to inaccurate estimation of perfusion. Respiratory motion during image acquisition introduces significant artifact. For ECG-triggered spASL, the accuracy of perfusion quantification may be especially reduced when imaging diseased animals with deeper and irregular respiratory motion, such as HFD mice or mice with myocardial infarction.

There are several specific challenges to gate for respiratory motion in a mouse spASL acquisition. First, breath holding is not an option when imaging anesthetized mice, and mechanical ventilation is too challenging to be performed routinely. Second, to measure perfusion accurately, the inversion pulses in spASL need to be as evenly spaced as possible at RR intervals in order to drive and maintain the blood magnetization at a steady state. The external respiratory sensor that is commonly used in ECG and respiratory gated scans [183] is unsuitable for gating spASL because the communication between the external device and the MRI scanner bundles the ECG and respiratory signals, causing the triggers to be unevenly spaced. Third, the diaphragm navigator method [184] is also unsuitable because it would require additional RF pulses to excite a column of spins perpendicular to the lung-diaphragm interface, which would interfere with the steady-state magnetization. As a result, we sought to use the self-gated technique to detect respiratory motion [185-190], which would introduce no additional RF pulses or interruptions to the scan. The physical basis of the self-gated technique is that any MRI echo or free induction decay is sensitive to motion, and time-dependent changes in these signals can be used to generate cardio-respiratory gating signals. This technique was introduced for human imaging [185, 186, 188] and later applied to imaging small rodents [189, 190].

3.3 Methods

3.3.1 Self-gated spASL Pulse Sequence

A self-gated spASL sequence was implemented using the IDEA development environment (Siemens, Erlangen, Germany). This sequence has a sequential looping structure, real-time retrospective ECG gating to allow true continuous imaging and self-navigated respiratory gating to account for breathing motion. The acquisition scheme is illustrated in Figure 3-1. The basis of the sequence is a cine-GRE sequence. Similar to the original spASL design [132], each acquisition consists of two contrasts, namely, the control and tag. In one of the TR's towards end systole, the readout part is substituted with a regional selective inversion pulse. For the tag contrast, the inversion region is above the atria and aorta region, nulling the blood signal, and for the control contrast, the inversion region is symmetric with respect to the imaging slice to account for any magnetization transfer effect (Figure 3-1, bottom). The combination readout RF pulses and inversion RF pulses, applied at consistent time intervals and flip angles, drive the myocardial magnetization to steady state. Since the capturing of the transition to steady state is not necessary for perfusion quantification, a sequential looping structure was implemented to minimize the number of transitions. Acquisition of all data for the control contrast is completed before switching to the tag contrast. Each contrast contains a number of averages (N_{avg}), and each average contains a number of phase-encode lines (N_{PE}) to sample the k-space fully. The phase-encode index is incremented after each RR interval. As a result, the number of heartbeats it takes to complete a full dataset is $2 \times N_{avg} \times N_{PE}$.

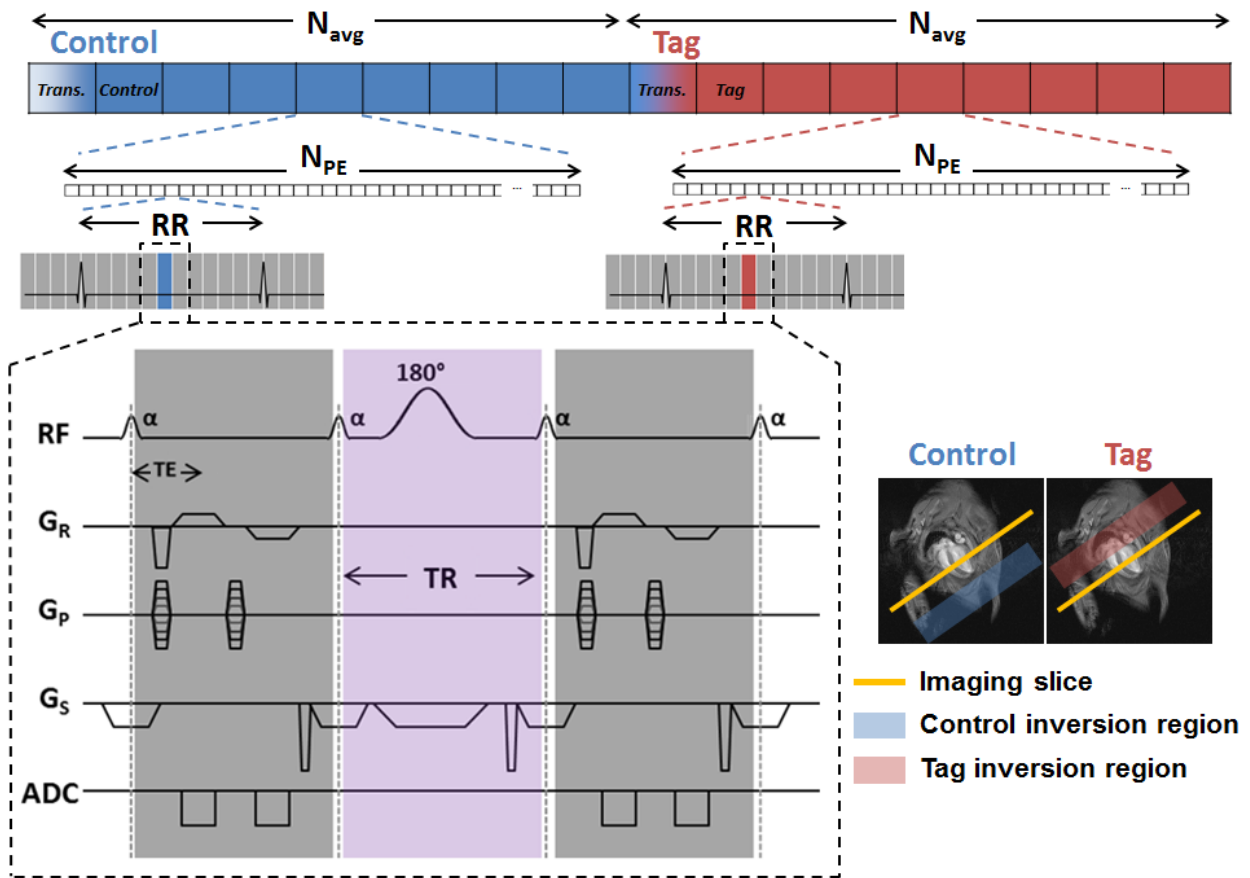


Figure 3-1. Schematic description of the modified-spASL pulse sequence. Each acquisition consists of two contrasts, namely, control and tag. The inversion regions of the control and tag scans are shown on the bottom right. The looping structure (top) shows data acquisition for the control contrast followed by the tag contrast. Only one transition to steady state is necessary for each contrast. The sequence is retrospectively gated to ECG signal in order to achieve continuous acquisition. The chronogram (bottom right) shows the readout module (in gray) and the spatially selective inversion pulse module (in purple). Each TR contains the readout for the spASL imaging data in the first echo and the acquisition of the self-navigated motion detection signal for respiratory gating in the second echo.

To eliminate any disturbances to the steady-state longitudinal magnetization, the sequence gates to ECG signal retrospectively in real time to allow true continuous steady-state imaging. At the beginning of each TR, the real-time controller determines the time between the current moment and the last ECG trigger detected. If this duration is greater than that of the previous TR, then the gradient and ADC are adjusted to read the next cardiac phase; if this duration is lower, indicating that a trigger was detected since the previous TR, then the gradient and ADC are adjusted to read the next phase encode.

A modified double echo sequence was implemented to acquire imaging and navigator data for retrospective respiratory gating in each TR [186]. At the end of the first echo, the second phase-encoding gradient negates the effect of the first phase-encoding gradient. Consequently, the first echo is phase-encoded and contains the gradient echo image data, and the second echo is nonphase-encoded and contains the motion sensitive self-navigator signal for respiratory gating. The addition of navigator echo introduces no interruptions or additional RF pulses to disturb the spASL steady state, and it has no impact on the imaging echo time (TE) or total scan time. The repetition time (TR) of the sequence is driven by the length of the spatially selective inversion pulse. Therefore, the additional echo also does not have any impact on TR or the temporal resolution. If a shorter inversion pulse is used, the acquisition time for the second echo can be easily shortened by reducing the number of readout points.

3.3.2 Retrospective Self-navigated Reconstruction

All reconstructions were performed retrospectively in MATLAB after the experiment. For all spASL reconstructions, whether with or without respiratory gating, the first 700 data points of each contrast are considered in transition and therefore excluded from reconstruction. The self-navigator data are obtained during the period where the readout gradient exists. To extract

motion information from raw MR data, the first step is to select the location along the readout direction that exhibits the most amount of respiration-related signal variation [187]. Since the location of this signal is not necessarily the center of k-space nor the line with peak energy, a search algorithm was written to select the location automatically. The algorithm first takes the magnitude of the complex navigator echo MR data. Then the algorithm use two rules to select the optimal location: first, the k-space is fully sampled or as fully sampled as possible (see the following paragraph); second, the line has the highest ratio between the energy within the respiratory frequency range (60-300 respiration/min) and within the cardiac frequency range (300-800 beats/min).

The magnitude of the self-navigator signal is representative of the physiological motion of the imaging echo within the same TR. The fluctuation of the self-navigator signal is affected by the collective motion of the object, which includes cardiac motion, respiratory motion, and noise. To extract the periodic respiratory waveform, the self-navigator signal is filtered through a low pass filter with a cut-off frequency of 10 Hz or 600 times/min. This cut-off frequency was selected because it is well above the physiological respiratory rate, which preserves the respiratory waveform, and at the same time, it effectively filters out the cardiac motion and the high-frequency noises. To create an adaptable threshold to accept or reject data, the self-navigator signal is filtered through a low pass filter with a cut-off frequency of 0.75 Hz or 40 times/min. This cut-off frequency was selected because it is unlikely that any mouse will have a respiratory rate lower than 40 respirations/min and, at the same time, the filtered signal captures any baseline drift during the scan. For respiratory gated reconstruction, the image data is accepted when the magnitude of the respiratory waveform is higher than that of the threshold. The valleys of the self-navigator signal are likely a result of the motion-induced spin density changes and through-plane motion during end expiration. After thresholding, the k-lines measured during the inhalation and exhalation respiratory motion (30-40% of all acquisitions)

are excluded from the reconstruction of the images. In the very rare event that all averages of a particular k-space line were below the threshold, which occurred in less than 0.1% of acquired data, the k-space line from the nearest cardiac phase was copied for reconstruction.

3.3.3 Experimental Design

We sought to evaluate the newly developed self-gated spASL sequence, examine the effect of respiratory gating in spASL imaging, and compare the self-gated spASL sequence with FAIR-LL ASL. For these studies, male wild-type C57BL/6 mice fed an HFD (60% calories from fat, Diet # 12492, Research Diets Inc., New Brunswick, NJ) for 24 weeks (n=7) and age-matched wild-type C57BL/6 mice fed standard chow diet (n=7) underwent self-gated spASL imaging and FAIR-LL ASL imaging at rest. The same scans were repeated one week later on the same animals to evaluate repeatability. Raw data from the spASL acquisitions were reconstructed both with and without respiratory gating. Global and segmental myocardial perfusion, pixel-wise myocardial perfusion spatial variability, and measurement repeatability were quantified to compare self-gated spASL and FAIR-LL ASL.

3.3.4 Animal Handling

All animal studies were performed under protocols that comply with the *Guide for the Care and Use of Laboratory Animals* (NIH publication no. 85-23, Revised 1996) and were approved by the Animal Care and Use Committee at the University of Virginia (Charlottesville, Virginia, USA). During imaging, mice were positioned supine in the magnet. Body temperature was maintained at $36 \pm 0.5^\circ\text{C}$ using circulating warm water. Anesthesia was maintained using

1.25% isoflurane in O₂ during MRI. The ECG, body temperature, and respiration were monitored during imaging using an MR-compatible system (SA Instruments, Stony Brook, New York).

3.3.5 MRI Acquisitions

MRI was performed on a 7T Clinscan system (Bruker, Ettlingen, Germany) using 30-mm or 35-mm diameter birdcage RF coils. The larger diameter RF coil was used to accommodate the heavier HFD mice. Localizer images were made in the short-axis and long-axis (4-chamber and 2-chamber) to determine the optimal location of the imaging slice and inversion regions. The location of the imaging slice was planned half-way between the spASL inversion regions for control and tag. In addition to sharing the same slice position, all perfusion scans, self-gated spASL and FAIR-LL ASL shared the following parameters: FOV = 38 x 38 mm² and voxel size = 0.3 x 0.3 x 1 mm³.

Parameters for self-gated spASL included: TR = 8 ms, TE = 2 ms, flip angle $\alpha = 7^\circ$ (Ernst angle), matrix size = 128 x 128, excitation pulse duration = 1 ms, inversion pulse duration = 3.6 ms, inversion labeling slice thickness = 6 mm, $N_{\text{avg}} = 9$, $N_{\text{PE}} = 128$. The total acquisition time was 5 minutes.

FAIR-LL ASL was performed with cardio-respiratory gating, fuzzy clustering, and a spiral readout, as previously described [129]. Imaging parameters for FAIR-LL ASL included: TR = 7 s, TE = 0.67 ms, flip angle = 3°, number of averages = 3, number of spiral interleaves = 84, interleaves per heartbeat = 3. Using k_y -t undersampling with randomness and a low-rank compressed-sensing reconstruction [125], the acquisition was rate-2 accelerated, providing a scan time of 15 minutes including both the slice-selective and the non-slice selective acquisition.

3.3.6 Image analysis

Image reconstruction and analysis were performed in MATLAB (Mathworks, Natick, MA).

For spASL, MBF was quantified as previously described [132]:

$$MBF = \frac{\lambda M_{SS}}{T_1^* M_0} \frac{\frac{\Delta M_\infty}{M_\infty^c}}{2\beta - \frac{\Delta M_\infty}{M_\infty^c}}$$

where partition coefficient λ was 0.95 [191]. M_{SS}/M_0 and T_1^* were estimated using the following equations and assuming $T_1 = 1.3$ s:

$$\frac{M_{SS}}{M_0} = \frac{1 - e^{-\frac{TR}{T_1}}}{1 - \cos(\alpha) e^{-\frac{TR}{T_1}}}$$

$$\frac{1}{T_1^*} = \frac{1}{T_1} - \frac{\ln(\cos(\alpha))}{TR}$$

β is the blood tagging efficiency and $\Delta M_\infty/M_\infty^c$ is the normalized signal difference at steady state. Both parameters were measured and calculated from the images directly.

Undersampled FAIR-LL images were reconstructed using Block LOw-rank Sparsity with Motion-guidance (BLOSM) [125]. Since the acquisition was cardio-respiratory gated, BLOSM motion guidance was not used and a single block covering the entire image was used, such that the BLOSM reconstruction reduced to a simple low-rank reconstruction method. Perfusion (P) was quantified using the T1-shift method [131]:

$$P = \frac{T_{1,NS}}{T_{1,blood}} \left(\frac{1}{T_{1,SS}} - \frac{1}{T_{1,NS}} \right) \cdot \lambda$$

For both spASL and FAIR-LL, regions of interests (ROIs) for blood and myocardium were drawn manually. For global perfusion, the myocardial contour included the entire left-ventricular myocardial area within a slice using conservative delineation of the endocardial and epicardial borders. For segmental perfusion, the global myocardial contour is divided into four sectors, namely, anterior, lateral, inferior, and lateral wall, and these sectors used RV insertion points as landmarks.

3.3.7 Statistical Analysis

Statistical analyses were performed using SigmaPlot (Systat Software Inc., Point Richmond, CA). Myocardial perfusion was analyzed for various groups of mice, by different perfusion assessment methods, and of different segments using two-way analysis of variance (ANOVA) with repeated measurements and the t-test, as appropriate. $P < 0.05$ was considered to be statistically significant. All values in the text are presented as mean \pm standard deviation.

3.4 Results

3.4.1 Effect of Respiratory Gating

Figure 3-2A shows a typical self-navigator signal intensity versus time. The self-navigator signal exhibits both low-frequency fluctuations consistent with the periodicity of the respiratory motion and high-frequency fluctuation consistent with heart rate. Respiratory waveform and the baseline drift, used for thresholding, were revealed by putting the navigator signal through low-pass filters with cut-off frequencies of 10 and 0.75 Hz, respectively (Figure 3-2B). The mean acceptance rate for all 28 datasets was 62.8 ± 4.9 %; 64.7 ± 5.6 % for control mice, and 61.0 ± 3.3 % for HFD mice. The accepted data for the sample self-navigator signal is

indicated in Figure 3-2C. In 3 out of the 28 data sets, the automatic algorithm did not pick out the best line that represented the respiratory waveform, and the selection was corrected manually. Representative spASL images and perfusion maps generated from spASL without and with self-navigated respiratory gating using the same HFD mouse dataset are shown in Figure 3-2D. These images demonstrate that self-navigated respiratory gating improves myocardial boundary definition and reduces partial volume.

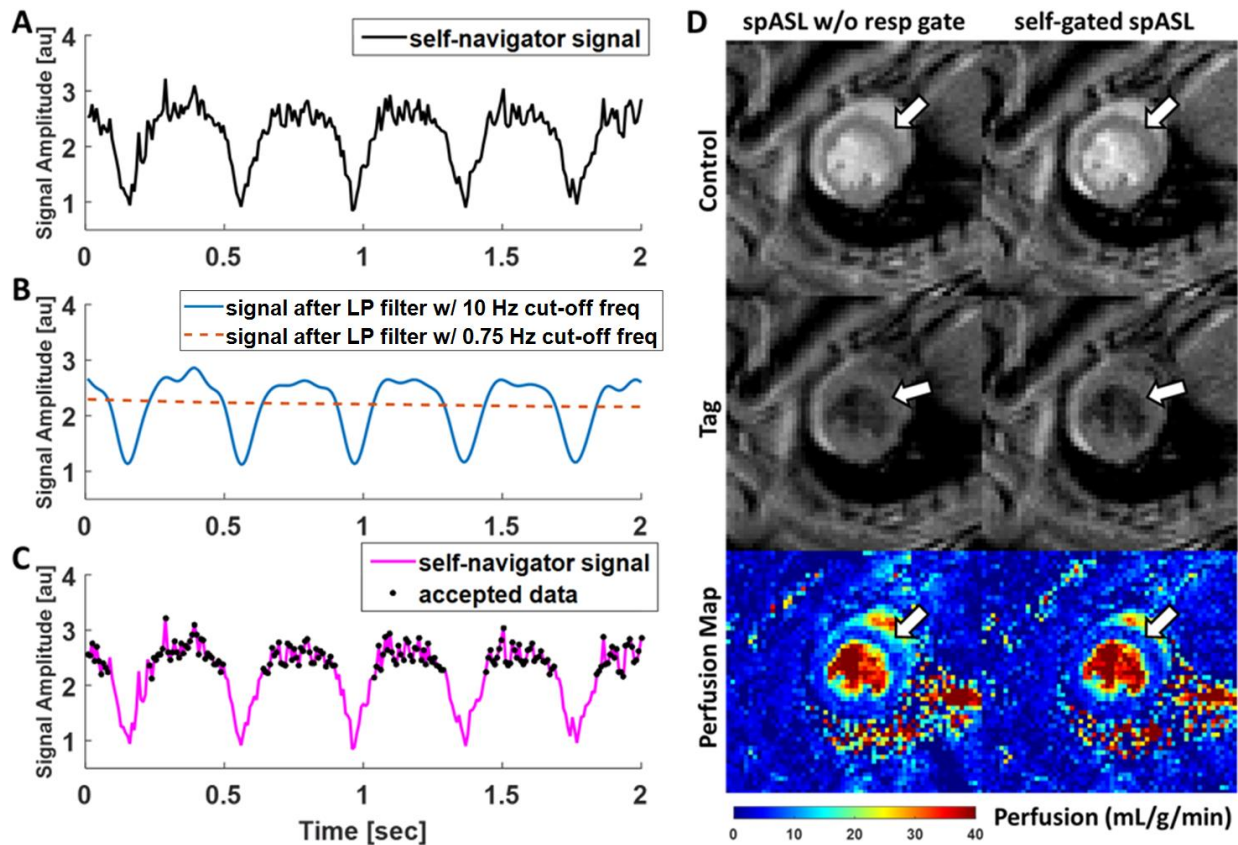


Figure 3-2. Respiratory gating with the self-gating signal. (A) Self-navigator signal acquired during in vivo mouse spASL experiment. (B) The respiratory waveform and threshold extracted from the self-navigator signal using low-pass filters with cutoff frequencies at 10 Hz and 0.75 Hz, respectively. Data points where the respiratory waveform signal is higher than the threshold are accepted for respiratory-gated reconstruction. (C) Accepted data points indicated on the self-navigator signal. (D) Example spASL images and perfusion maps of an HFD mouse heart reconstructed without and with self-navigated respiratory gating. Respiratory gating improves myocardial boundary definition and reduces partial volume.

Measurements of global and segmental (anterior, lateral, inferior, and lateral wall) perfusion estimated using ungated and self-gated spASL are shown in Figure 3-3. Perfusion was averaged over scans of all mice, of control mice, and of HFD mice. Overall, spASL reconstructed with respiratory gating measured lower perfusion than non-respiratory gated spASL (Figure 3-3A). Upon closer examination, in control mice, the difference was not statistically significant (Figure 3-3B). In contrast, in HFD mice, the differences are significant in global, lateral, inferior, and septal perfusion (Figure 3-3C). The global myocardial perfusion for self-gated and ungated spASL are 4.5 ± 0.8 and 5.4 ± 1.1 ml/g/min, respectively for HFD mice. Other perfusion values are summarized in Table 1. This result indicates that retrospective respiratory gating significantly reduces partial volume and that it is more important when scanning HFD mice. There are no differences among sectors or compared to global perfusion. The pixel-wise perfusion spatial variation within the myocardium are similar for myocardial perfusion maps reconstructed with or without respiratory gating. This is likely because while respiratory gating reduces partial volume, it also uses fewer averages to suppress background noise.

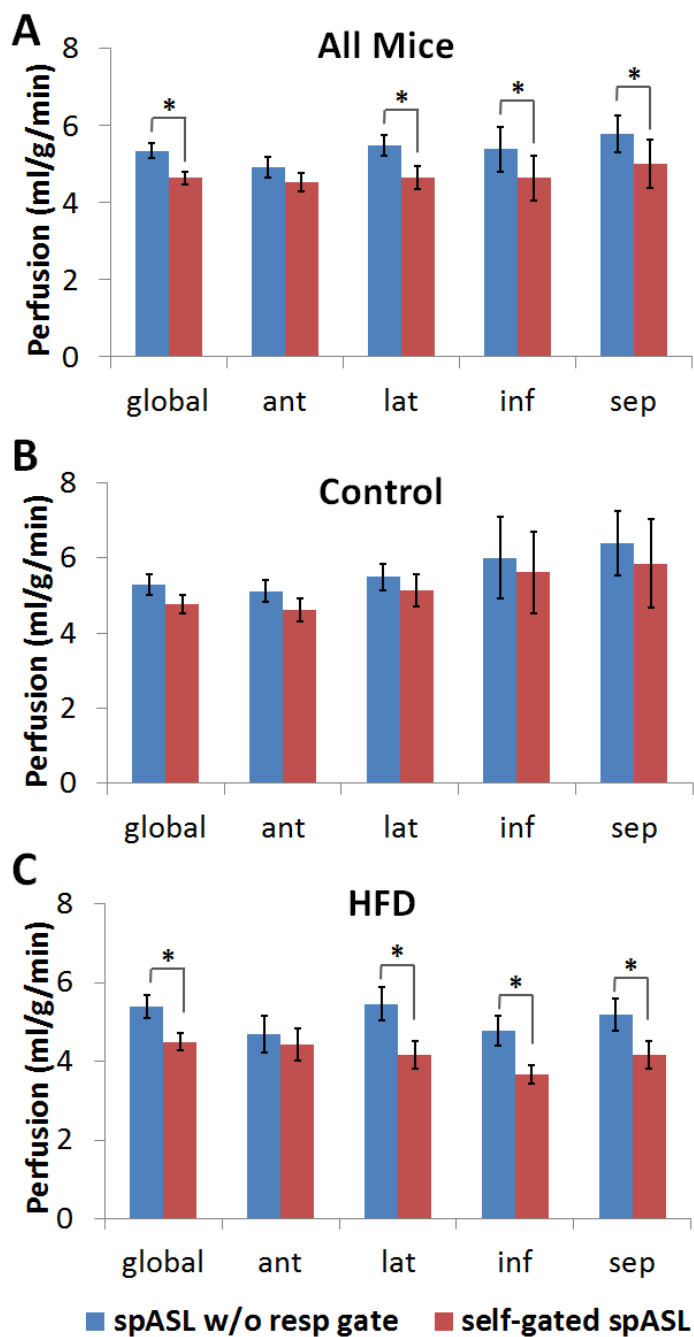


Figure 3-3. Global and segmental myocardial perfusion values of all mice (A), control mice only (B), and HFD mice only (C). Values were measured using spASL without respiratory gating (blue) and with self-navigated respiratory gating (red). (* $P < 0.05$ by two-way ANOVA with repeated measures).

3.4.2 Comparison: Self-gated SpASL versus FAIR-LL ASL

Example FAIR-LL ASL and spASL images and perfusion maps of a mouse heart are shown in Figure 3-4. For the FAIR-LL ASL images, non-slice selective (Figure 3-4A) and slice-selective (Figure 3-4B) images are shown at selected inversion times; and for spASL, the control (Figure 3-4C) and tag (Figure 3-4D) images are shown at selected cardiac phases. The normalized signal intensity time curves of the myocardium from a FAIR-LL ASL acquisition and a spASL acquisition are shown in Figure 3-4E and Figure 3-4F. FAIR-LL ASL measures the effect of perfusion on apparent myocardial T1 relaxation, while spASL measures the effect of perfusion on gradient echo steady state. Example perfusion maps generated from FAIR-LL ASL and spASL are shown in Figure 3-4G and Figure 3-4H. From visual inspection, spASL perfusion maps have better spatial homogeneity within the myocardium than FAIR-LL ASL. Quantitatively, the coefficient of variation for pixel-wise perfusion quantification within the myocardium are 0.74 ± 0.25 and 0.96 ± 0.34 , for self-gated spASL and FAIR-LL ASL, respectively, and are statistically significantly different ($P < 0.01$).

Figure 3-5 summarizes global and segmental (anterior, lateral, inferior, and lateral wall) perfusion measured using self-gated spASL and FAIR-LL ASL from all mice. Self-gated spASL measured lower absolute perfusion than FAIR-LL ASL globally and segmentally. The average global perfusion for self-gated spASL and FAIR-LL ASL are 4.6 ± 0.9 and 7.0 ± 1.7 ml/g/min, respectively. Two-way ANOVA with repeated measurements also tested significant difference among the segmental perfusion and global perfusion measured by FAIR-LL ASL. The significances are indicated using the various symbol in Figure 3-5. However, ANOVA revealed no difference among segments by spASL. No segmental differences are expected from the control or HFD mice scanned.

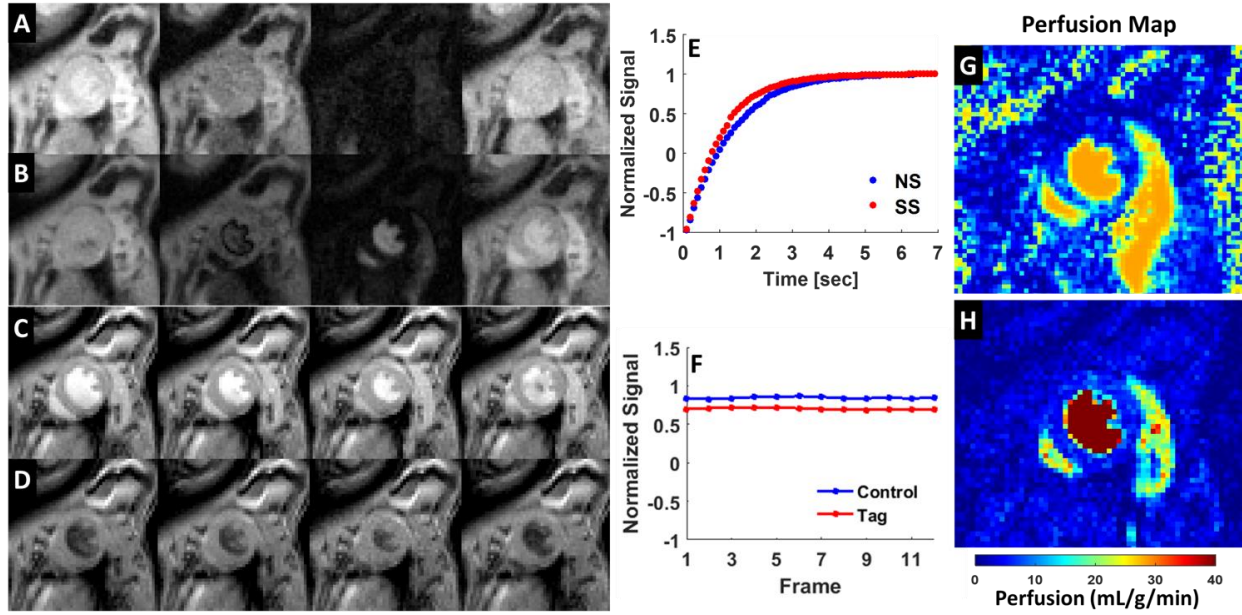


Figure 3-4. Example FAIR-LL ASL and spASL images (A-D) and perfusion maps (G,H) of a mouse heart. For FAIR-LL ASL images, non-slice selective (A) and slice-selective (B) images are shown at selected inversion times. For spASL, control (C) and tag (D) images are shown at selected cardiac phases. FAIR-LL measures the effect of perfusion on apparent myocardial T1 relaxation (E), and spASL measures the effect of perfusion on gradient echo steady state (F).

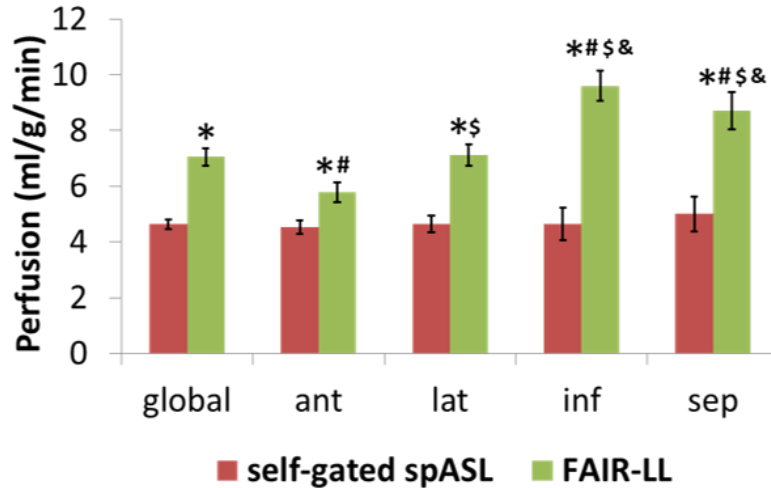


Figure 3-5. Myocardial perfusion values of all mice measured using spASL with self-navigated respiratory gating (red) and FAIR-LL (green). (* $P < 0.05$ vs. self-gated spASL, # $P < 0.05$ vs. global perfusion by FAIR-LL, \$ $P < 0.05$ vs. anterior perfusion by FAIR-LL, & $P < 0.05$ vs. lateral perfusion by FAIR-LL by two-way ANOVA with repeated measures).

Bland-Altman plots comparing the repeatability of self-gated spASL and FAIR-LL ASL in perfusion quantification are shown in Figure 3-6. Self-gated spASL show better repeatability than FAIR-LL ASL in assessment for global perfusion (Figure 3-6 A-B) and segmental perfusion (Figure 3-6 C-D). The coefficient of repeatability for self-gated spASL and FAIR-LL ASL are 3.1 and 6.6 ml/g/min, respectively, or 56% and 82%, respectively.

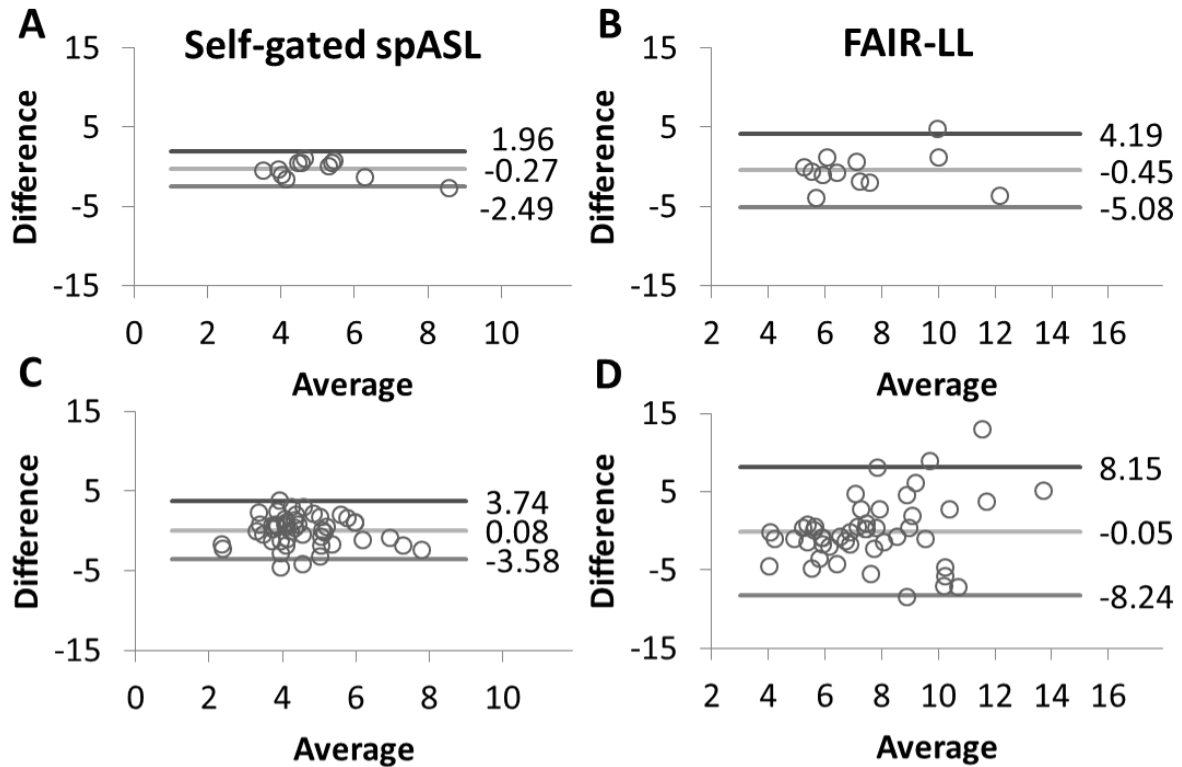


Figure 3-6. Bland-Altman plots for comparisons of repeatability between self-gated spASL (A,C) and FAIR-LL (B,D) for quantifying global (A,B) and segmental (C,D) myocardial perfusion.

3.5 Discussion

In this study, we developed a self-gated spASL perfusion MRI method for mice, which allowed cardio-respiratory gated spASL imaging to be performed without interruptions for the first time. This method used real-time retrospective ECG gating in order to gate to cardiac motion and retrospective self-navigated respiratory gating in order to gate to respiratory motion. It also used a sequential looping structure which significantly reduced the scan time by minimizing the number of transitions to steady state. Within a 5-minute scan time, the self-gated spASL technique successfully measured myocardial perfusion in control and HFD mice. Respiratory gating by self-navigator significantly reduced artifacts when imaging HFD mice.

Compared to FAIR-LL ASL, we found that self-gating spASL provides better spatial and segmental homogeneity in myocardial perfusion and better repeatability. Measurements of absolute perfusion were lower for self-gated spASL than for FAIR-LL. The gold standard method to measure regional myocardial perfusion is by fluorescent microspheres. Regional flow is calculated by counting the number of injected microspheres in the segment of interest. While this method has been applied in canines [192] and pigs [193], there are concerns about the validity of this technique in rodents because of the limited spatial resolution possible in such small organs [194]. Mouse hearts typically have tissue volumes of 100 to 200 μL and cannot provide the adequate spatial information to accommodate the 400 microsphere per piece rule required for confidence in the measurements [195]. With no gold standard, it is unknown which mouse perfusion method is more accurate. However, reduced variability and repeatability is important because it provides more statistical power for hypothesis testing.

3.5.1 Self-navigated Respiratory Gating

We evaluated the effect of respiratory gating by comparing reconstruction results with and without respiratory gating. Visually, respiratory gating improved myocardial boundary definition and reduced partial volume. Quantitatively, respiratory gating in HFD mice significantly reduced partial volume, which is evidenced by the significant lower perfusion measured using respiratory-gated spASL than by ungated spASL. The difference, however, is not significant in control mice. This is likely because HFD mice have deeper and more irregular respiratory motion than control mice; as such, the imaging of HFD mice resulted in more breathing artifacts when ungated. Respiratory gating is more important when imaging diseased mice. The reason that the spASL images without respiratory gating do not have more severe motion artifacts is likely due to the high number of averages, $N_{\text{avg}} = 9$ used in this study.

Theoretically, the signal at the center of the navigator echo contains most of the information needed to detect motion. However, among the data collected in this study, the line that best represents respiratory motion is not necessarily at the center of k-space. This may be due to eddy current effect or imperfection in gradient cancellation. It may also be attributed to the navigator signal coming from the second echo, which has second- and higher-order motion terms. The self-gated method has been reported to also characterize cardiac motion and can completely replace external sensors in mouse imaging [189, 196]. However, wireless spASL imaging may be challenging since the self-gated signal has lower sensitivity to heart motion during the dark-blood contrast; as such, gating may be difficult. Additionally, as in imaging any anesthetized animal, it is important to monitor the physiology throughout the experiment. To completely eliminate electrodes and external monitoring, the sequence must also be able to display in real time the heart rate and respiratory rate on the scanner console. As a result, while eliminating external sensors would reduce animal preparation time, the self-gated ECG trigger needs to be tested rigorously before applied to spASL imaging.

3.5.2 Comparison of Perfusion Methods

Compared to the original spASL method, the self-gated spASL improves the accuracy of perfusion measurement by (1) enforcing true steady state imaging and (2) reducing respiratory artifact. As a result of using the sequential looping structure, self-gated spASL spend less than 10 seconds in total in transition to steady state out of the entire scan, versus half of the scan time (4 minutes) in the original design [132]. While the sequential looping structure is faster, it may be more sensitive to physiological changes during the scan.

FAIR-LL ASL showed much greater segmental variability than self-gated spASL. We speculate that this is due to the spiral blurring and distortion near the tissue-lung interface and

the tissue-blood interface. Since the self-gated spASL is a Cartesian sequence, there would be no spiral related artifacts. Measurements of absolute perfusion were lower for self-gated spASL than FAIR-LL at 4.6 ± 0.9 and 7.0 ± 1.7 ml/g/min, respectively. With no gold standard, it is unknown which method is more accurate. Previously published studies using other perfusion techniques reported a mean resting perfusion of 4.1 - 7.0 ml/g/min [129, 177, 191, 197-200]. Our perfusion estimates both by self-gated spASL and FAIR-LL ASL are within the range of these published values.

3.5.3 Limitations

This study had several limitations. First, the respiratory gating was accomplished retrospectively. In order to acquire each k-space line during a quiescent period of the respiratory cycle, the k-space was oversampled with nine averages. Future development may implement a real-time self-navigator processing module that prospectively gates image acquisition to respiration. Such a module would produce a satisfactory SNR and fully sampled k-space with much fewer averages and therefore further reduce scan time. Second, the spASL method requires T1 in its perfusion calculation. In this study, we assumed a global myocardial T1 value. However, this may not be appropriate when imaging animals with expected regional perfusion defects or T1 variation. In these cases, a separate T1 mapping scan of the same resolution, FOV, and cardiac phase may be needed to quantify perfusion accurately. Finally, the current implementation of self-gated spASL only allows for perfusion measurement in a single slice. Future technical development combining PICORE RF pulse design with simultaneous multi-slice imaging and reconstruction may facilitate increased slice coverage.

3.6 Conclusions

The self-gated spASL technique presented in this paper improves upon the prior cardiac spASL or cine-ASL methods in mice and develops a method that assesses myocardial perfusion *in vivo* that is insensitive to respiration and enables true steady state imaging regardless of heart rate changes. Self-navigated respiratory gating improved boundary definition and reduced the partial volume in spASL imaging, and respiratory gating is more important when quantifying perfusion in diseased mice with deeper respiratory motion such as the HFD mice. With the short scan time of fewer than 5 minutes and no need for contrast agents, self-gated spASL can easily be integrated into cardiac MRI exams. Despite the short scan time, self-gated spASL is experimentally shown to provide less variability and better repeatability in quantifying myocardial perfusion in mice than FAIR-LL ASL. Nonetheless, the FAIR-LL ASL is more suitable for detecting regional perfusion defects, such as in mice with myocardial infarction. The self-gated spASL technique may be used to image diet-induced obese mice or genetically modified mice in order to test therapy for and study mechanisms underlying cardiovascular diseases such as a coronary microvascular disease.

**Chapter 4 First-pass Nitroxide-enhanced MRI for Imaging
Myocardial Perfusion without Gadolinium**

4.1 Abstract

First-pass MRI using gadolinium-based contrast agents is widely used to image myocardial perfusion. However, gadolinium is contraindicated in patients with severely impaired renal function (a substantial portion of heart disease patients), and methods that do not employ gadolinium are needed. Nitroxide stable free radicals are non-metallic compounds with an unpaired electron and, correspondingly, are paramagnetic and T1-shortening. We investigated first-pass nitroxide-enhanced perfusion MRI of the heart as an alternative to first-pass gadolinium-enhanced MRI. Five C57Bl/6 mice underwent first-pass imaging with the nitroxide agent 3CP, and the results showed that nitroxide-enhanced MRI could quantify regional myocardial blood flow, as the average myocardial perfusion was 7.0 ± 1.3 ml/g/min, a value in the normal range for mice.

4.2 Introduction

First-pass MRI using gadolinium-based contrast agents is widely used to image myocardial perfusion in clinical research and diagnosis. Multicenter trials have shown its superiority over SPECT in diagnosing perfusion defects [201, 202]. The key advantages of the first pass methods are the high spatial resolution and a large amount of signal change following a bolus of contrast agent. However, gadolinium is contraindicated in patients with severely impaired renal function and can lead to organ fibrosis and failure. In 2015, estimated 661,648 patients had the end-stage renal disease [203], and death rates from cardiovascular disease in end-stage renal disease patients are 20 to 40 times higher than in the general population [204]. MR imaging methods that do not employ gadolinium are needed.

Arterial spin labeling (ASL) is a potential alternative. As discussed extensively in the previous chapter, ASL is contrast-free perfusion method that uses magnetically labeled blood as an endogenous tracer. The contrast differences created by labeled and unlabeled blood, or ASL signal, is directly proportional to perfusion. While ASL is a well-established method for quantifying myocardial perfusion in mice, ASL imaging to measure myocardial perfusion in human remain challenging. This is because humans have a much lower myocardial perfusion than rodents. In humans, the ASL signal is measured to be less than 4%, and on average only 1.5% [205].

Nitroxide radicals are non-metallic compounds with antioxidant properties to degrade superoxide and peroxide and has been used in biophysics studies [206] to measure the level of oxidative stress, control hypertension, protect against damage from ischemia/reperfusion injury, and cancer prevention as it protects against ionizing radiation. On the other hand, as a radical, nitroxide has an unpaired electron, which correspondingly gives the compound paramagnetic property and is, therefore, T1-shortening [207]. Nitroxides are not commonly used in MRI because the metal-based contrast agents have a higher number of unpaired electrons, namely Gd (seven unpaired electrons), Fe (five unpaired electrons) and Mn (five unpaired electrons). Additionally, when administered intravenously, nitroxides undergo a bioreduction to a diamagnetic species called N-hydroxy and lose their T1-shortening property over the course of several minutes [208] (Figure 4-1).

Prior studies have used nitroxides in preclinical cancer imaging *in vivo* to assess tumor redox status [209, 210]. Since first-pass perfusion imaging occurs on a time scale on the order of seconds, we investigated first-pass nitroxide-enhanced perfusion MRI of the heart as an alternative to first-pass gadolinium-enhanced MRI.

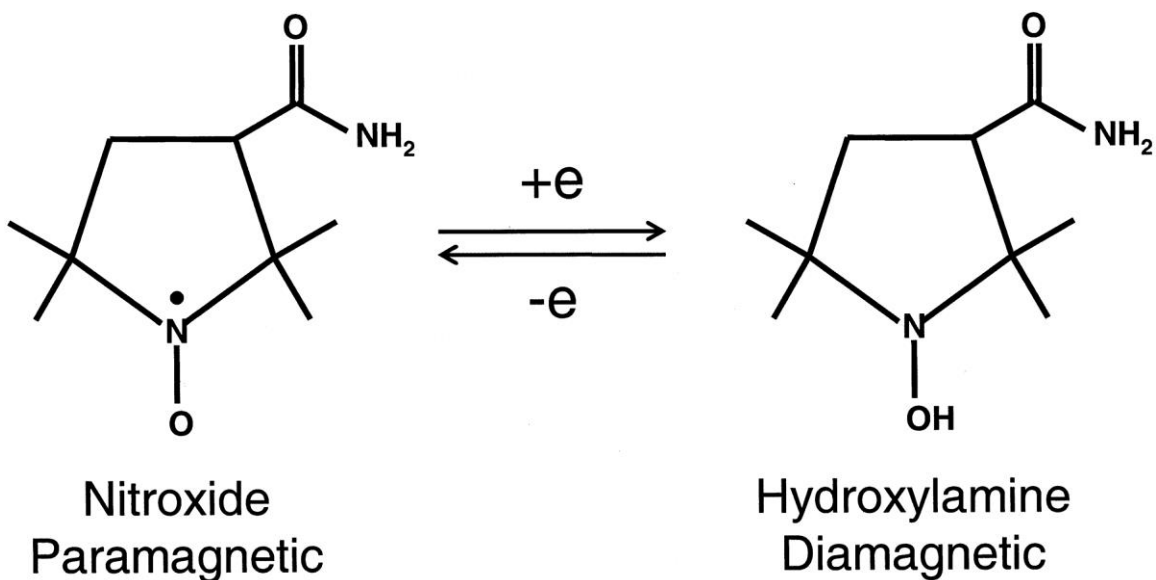


Figure 4-1. Chemical structure of nitroxide radicals and reduction process [207]

4.3 Methods

4.3.1 Relaxivity Measurement

The nitroxide contrast agent 3-Carbamoyl-PROXYL (3CP) (Sigma–Aldrich, St. Louis, MO) was chosen because it is water soluble, commercially available and well tolerated by mice. The relaxivity of 3CP at 7T was measured using a series of 12 phantoms with a range of 3CP concentrations of 0 to 35mM. The phantom's T1 values were measured using a Look-Locker sequence. Relaxivity Γ was calculated by least square fitting of the following equation:

$$\frac{1}{T1} = \frac{1}{T1_{baseline}} + \Gamma \cdot [3CP]$$

4.3.2 Animal Experiment

To assess nitroxides-enhanced first pass perfusion *in vivo*, wild-type male C57Bl/6 mice (n = 5) underwent MRI using a 7T system (Clinscan, Bruker) using 30-mm diameter birdcage RF coils. The ECG, body temperature, and respiration were monitored during imaging using an MR-compatible system (SA Instruments, Stony Brook, NY). An indwelling tail vein catheter was established to deliver 3CP. Body temperature was maintained at $36 \pm 0.5^\circ\text{C}$ using circulating warm water, and anesthesia was maintained using 1.25% isoflurane in O_2 during MRI.

First-pass nitroxides MRI was performed using a rate-3 undersampled saturation-recovery rapid gradient echo imaging with k_y -t undersampling and a motion-compensated compressed sensing reconstruction algorithm as recently described [120]. After localizer imaging, first-pass perfusion MRI was performed in a mid-ventricular short-axis slice. Imaging parameters included: TR = 1.8 ms, TE = 1 ms, FOV = $34 \times 24 \text{ mm}^2$, matrix size = 128×102 , image resolution = $0.27 \times 0.24 \text{ mm}^2$, excitation flip angle = 15° , slice thickness = 1 mm, and saturation delay = 45 ms. Proton density weighted images were acquired at the end of the acquisition to normalize signal intensities for perfusion analysis. All imaging parameters were kept the same for proton density weighted image acquisitions compared to the saturation recovery portion of the image acquisition, except that no saturation pulse was applied upon detection of the ECG R-wave and a flip angle of 5° was used. 3CP was administered through an indwelling tail vein catheter at 2 mmol/g body weight 10 seconds after the start of the first-pass acquisition over 3 to 4 seconds.

4.3.3 Image Analysis

Images were reconstructed using BLOSM [125], a compressed sensing method. Signal intensities of blood and myocardial regions were normalized by proton density images and were

converted to 3CP concentrations using the methods described by Cernicanu and Axel [127], and perfusion was quantified using Fermi function deconvolution [126]. Regional perfusion was assessed in regions of interest defined as anterior, anterolateral, inferolateral, inferior, inferoseptal, and anteroseptal according to a standard American Heart Association segment model. To compare the signal enhancement from 3CP to that achieved using a standard dose of Gd (0.1 mmol/kg), Gd-enhanced first-pass MRI was also performed and the blood and myocardial peak enhancement ratios were calculated for 3CP and gadolinium using the following formula:

$$\text{Percentage Enhancement} = (SI_{post} - SI_{pre})/SI_{pre} \times 100\%$$

where SI_{pre} is the pre-contrast signal intensity and SI_{post} is the peak post-contrast signal intensity.

4.4 Results

4.4.1 Relaxivity Measurement

In phantoms, the relaxation rates R1 (or 1/T1) increased linearly with 3CP concentration in the range of 0.5 to 35 mM at 7T (Figure 4-2), and the relaxivity of 3CP in saline solution was measured to be 0.14 mM⁻¹sec⁻¹.

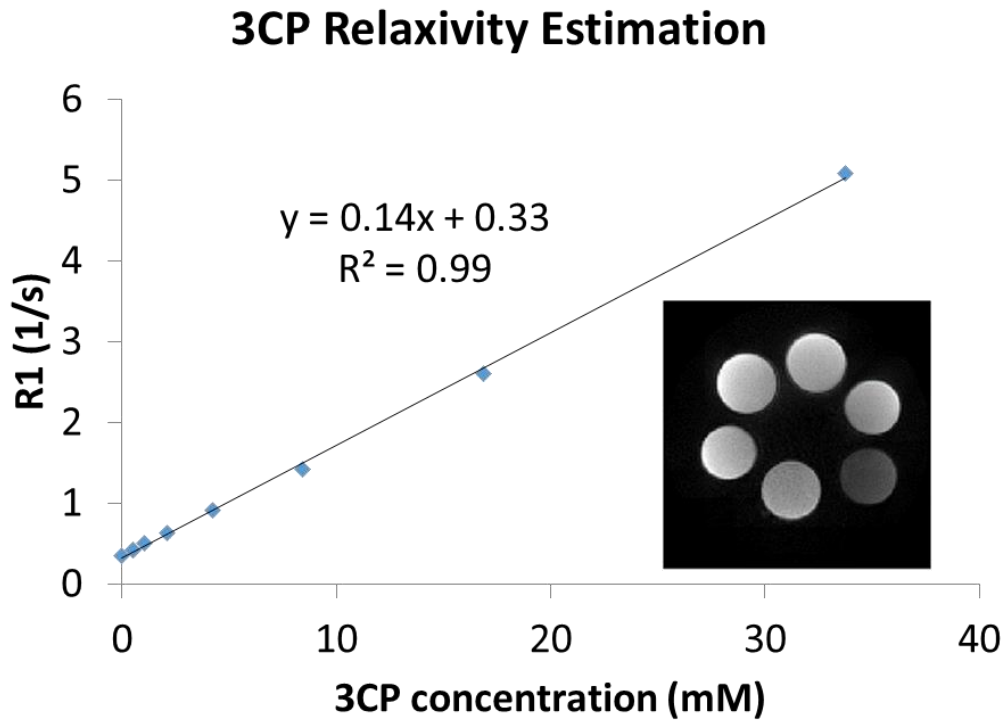


Figure 4-2. Relaxation rate R_1 (or $1/T_1$) of 3CP as a function of concentration in saline.

4.4.2 First-pass Nitroxide-enhanced MRI in Mice

3CP generated substantial enhancement of the blood and myocardium. Figure 4-3 shows example 3CP-enhanced first-pass MR images obtained from a mouse before (a) and after (b,c,d,e) injection of 3CP.



Figure 4-3. Example nitroxide-enhanced first-pass MR images of the mouse heart obtained before (a) and after (b,c,d,e) injection of 3CP (2 mmol/g body weight) via a tail vein catheter.

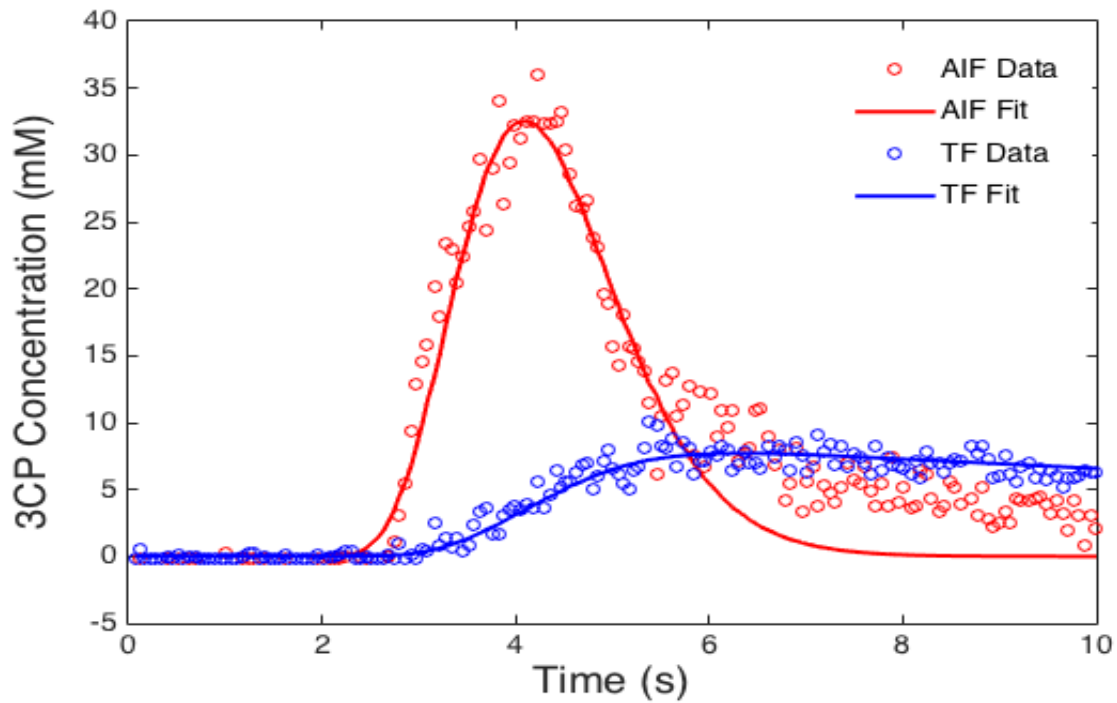


Figure 4-4. Example nitroxide-enhanced first-pass MRI arterial input function (AIF, red) and tissue function (TF, blue) data and fits obtained from a mouse.

Figure 4-4 shows example arterial input function (AIF) and tissue function (TF) data and fits obtained from a mouse. First-pass nitroxide-enhanced MRI was able to quantify global and segmental myocardial perfusion in mice. Table 1 summarizes the myocardial perfusion values (mean \pm standard error) from 5 mice using 3CP-enhanced first-pass MRI. The percentage enhancement at peak signal enhancement achieved by 3CP at 2 mmol/g (n=5) were $725 \pm 100\%$ and $275 \pm 41\%$ for blood and myocardium, respectively, compared to $1130 \pm 60\%$ and $342 \pm 21\%$, respectively, for gadolinium at 0.1 mmol/kg (n=5).

4.5 Conclusion and Discussion

We demonstrated that first-pass nitroxide-enhanced MRI, a non-gadolinium technique, can quantify myocardial perfusion in mice. As shown, 3CP generated substantial enhancement of the blood and myocardium, and the perfusion values estimated are within the normal range for mice [123]. While nitroxides have not been tested in humans, in principle nitroxide-enhanced MRI could translate to humans as these compounds may have sufficient safety profiles.

Table 4-1. Regional and global perfusion values (mean \pm standard error, n=5) measured using nitroxide-enhanced first-pass MRI.

Region	Flow (ml/g/min)
Global	7.0 \pm 1.3
anterior	7.3 \pm 1.3
anterolateral	7.3 \pm 2.5
inferolateral	8.5 \pm 2.0
inferior	6.6 \pm 0.7
inferoseptal	7.9 \pm 1.3
anteroseptal	6.2 \pm 0.7

Chapter 5 Conclusions and Future Directions

5.1 Conclusions

Minimally invasive MRI tools were developed in this dissertation to assess coronary microvascular function. The LNAME T1 mapping method probes the coronary endothelial-dependent dysfunction aspect of CMD, and the self-gated perfusion method used with endothelial-independent vasodilator such as regadenoson probes the coronary endothelial-independent dysfunction aspect of CMD. These new imaging tools combined with mouse models of CMD would help study molecular mechanisms behind CMD and establish models of CMD to test traditional or novel treatments.

5.1.1 Imaging Coronary eNOS Function by LNAME T1 Mapping

The major finding of this study is that an increase in myocardial T1 during NOS inhibition by LNAME is a marker of coronary microvascular endothelial function. Compared to other endothelial assessment techniques, the LNAME T1 mapping method uniquely probes the effect of inhibiting NOS on coronary microvascular permeability and, as demonstrated by the experiments in eNOS^{-/-} mice, the effect was shown to be specifically mediated by eNOS. Using this method, it was demonstrated that coronary microvascular eNOS dysfunction precedes impairment of myocardial perfusion reserve, which is consistent with the current understanding of the progression of coronary vascular disease in HFD mice. This method may be useful for preclinical studies that investigate mechanisms underlying and therapies for coronary microvascular endothelial dysfunction. Since T1 mapping is now nearly ubiquitous, these methods could be easily adopted in many preclinical MRI labs.

5.1.2 Self-gated spASL MRI in Mice

An improved perfusion method for mice called self-gated spASL was developed. The self-gated spASL quantitatively assess myocardial perfusion in under 5 minutes and without contrast agents. The self-gated spASL improves upon the original spASL sequence and reduces the readout inefficiencies, enables true steady state imaging regardless of heart rate changes, and is insensitive to respiratory motion. Self-navigated respiratory gating significantly reduces respiratory artifacts in diseased mice with deeper respiratory motion such as the HFD mice. Compared to FAIR-LL ASL, the self-gated spASL method uses one-third the scan time and provides less variability and better repeatability in quantifying myocardial perfusion in mice. Although the FAIR-LL ASL is more suitable for detecting regional perfusion defects, such as in mice with myocardial infarction. With the short scan time and no need for contrast agent, self-gated spASL can easily be integrated into cardiac MRI exams. The method may be especially useful in studies involve diet-induced obese mice or genetically modified mice to study mechanisms underlying and test therapy for global cardiovascular diseases such a coronary microvascular disease.

5.1.3 First-pass Nitroxide-enhanced MRI Myocardial Perfusion Quantification

For the first time, nonmetallic compound nitroxide was used as an alternative to gadolinium for first-pass contrast-enhanced myocardial perfusion imaging in mice. The nitroxide compound 3CP generated substantial enhancement of the blood and myocardium and enabled both global and segmental perfusion quantification. The perfusion values estimated are within the normal range for mice. While nitroxides have not been tested in humans, in principle nitroxide-enhanced MRI could translate to humans as these compounds may have sufficient

safety profiles. Nitroxide-enhanced MRI may be an alternative to gadolinium-enhanced MRI for patients that cannot tolerate gadolinium.

5.2 Future Directions

5.2.1 Imaging Coronary eNOS Function by LNAME T1 Mapping

Although we showed that coronary microvascular endothelial dysfunction precedes impaired myocardial perfusion reserve in HFD mice, we did not determine the earliest time point at which coronary microvascular endothelial dysfunction can be detected in this disease model. Future studies may seek to more precisely determine the time of onset of coronary microvascular endothelial dysfunction in HFD mice.

In addition to the roles of eNOS in vasodilation, blood flow, and microvascular permeability, eNOS also plays important roles in the inhibition of platelet aggregation and adhesion to the vascular wall, an early event in the development of atherosclerosis, suppression of vascular smooth muscle cell proliferation, and modulation of leukocyte-endothelial interactions. Thus, methods to noninvasively assess eNOS function may be used in the future to shed light on the roles of microvascular eNOS in normal physiology and with regard to its various roles and functions. Therapies that may prevent or treat eNOS dysfunction include bone marrow cell treatment, gene therapy, drugs targeting the renin-angiotensin-aldosterone system, and statins. The LNAME T1 mapping may be a useful method to test whether therapeutic agents promote improved eNOS function.

5.2.2 Improvement for Self-gated Steady State Pulsed ASL MRI in Mice

First, the respiratory gating was accomplished retrospectively. In order to acquire each k-space line during a quiescent period of the respiratory cycle, the k-space was oversampled with nine averages. Future development may implement a real-time self-navigator processing module that prospectively gates image acquisition to respiration. Such a module would produce a satisfactory SNR and fully sampled k-space with much fewer averages to and therefore further reduce scan time. Second, all spASL and FAIR-LL images were segmented manually. Future development or application of an automatic segmentation algorithm would decrease the amount of time spent on image analysis. Finally, the current implementation of self-gated spASL only allows for perfusion measurement in a single slice. Future technical development combining PICORE RF pulse design with simultaneous multi-slice imaging and reconstruction may facilitate increase slice coverage.

5.2.3 First-pass Nitroxide-enhanced MRI Myocardial Perfusion Quantification

Nitroxide stable free radicals lose their T1-shortening property as they undergo in vivo reduction reactions. Given this property, nitroxides have been used as redox-sensitive MRI contrast agents in preclinical cancer imaging to assess tumor redox status. Future development of a dynamic nitroxide-enhanced MRI method that measures redox reactions between the paramagnetic nitroxide the intracellular oxidizing species would allow noninvasive assessment of oxidative stress localized to the heart. These methods may be broadly applicable to preclinical studies of mechanisms and experimental therapies in numerous models of cardiovascular disease to study disease mechanisms and test therapies aiming at decrease oxidative stress.

Appendix A: Detection of Increased Coronary Microvascular Permeability with MRI T1 mapping and Gadolinium-labeled Albumin

This following study used macromolecular contrast agent Galbumin to show that LNAME and endothelin-1 cause an increase in microvascular permeability as evidenced by the increase in Galbumin partition coefficient. While we decided not to continue with the experiment on Galbumin, the findings of this experiment inspired the LNAME T1 mapping technique which was developed and applied in Aim 1 and 2 of this dissertation, summarized in [Chapter 2](#).

Background

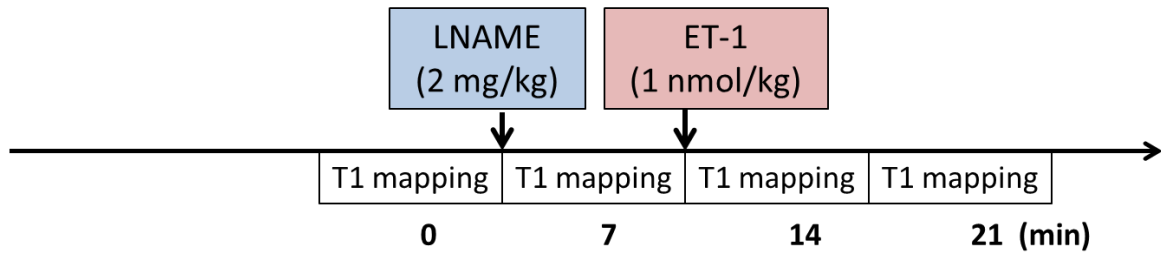
Conditions such as obesity and diabetes lead to coronary microvascular disease and, subsequently, an increased risk of adverse cardiac events. Increased microvascular permeability is thought to be an early biomarker of coronary microvascular disease. Currently, there are limited methods for imaging coronary microvascular permeability. Miles assay is the gold standard measurement to assess blood vessel permeability in animals [211]. This technique starts with an intravenous injection of Evans blue dye and a 30 minute waiting period, followed by organ collection. Then the Evans blue dye is extracted from the organ of interest and the amount of Evans blue dye in interstitial tissue is quantified. Evans blue dye has a high affinity for albumin, which is the standard molecule for measuring microvascular permeability. The invasive nature of this method prevents serial studies and has no potential to translate to human studies.

Gadolinium-labeled albumin, also known as Galbumin, is commercially available for preclinical imaging (BioPal, Worcester, MA). Studies have used this macromolecular contrast to detect myocardial infarction [212]. We hypothesized that MRI T1 mapping with gadolinium-labeled albumin could detect more subtle changes in coronary microvascular permeability such as those induced by noninjurious pharmacological methods. Previous studies [106] have shown that pharmacological inhibition of nitric oxide synthase (NOS) with agents such as NG-nitro-L-arginine methyl ester (LNAME) rapidly depletes the local vessel wall NO concentration, leading to a rapid increase in microvascular permeability. Additionally, intravenous injection of endothelin-1 (ET-1) causes smooth muscle cell contraction which further enhances the increase in microvascular permeability. The increase in microvascular permeability leads to protein efflux from the blood to the extracellular space, and microvascular fluid efflux.

Methods

We sought to develop and evaluate MR imaging methods to detect pharmacologically induced reversible changes in coronary microvascular permeability. For these studies, wild type male C57Bl/6 mice (n=7) underwent MR imaging at 7T using a Clinscan system (Bruker, Ettlingen, Germany). Mice were anesthetized with 1.25% isoflurane and maintained at $36 \pm 0.5^\circ\text{C}$ during MRI, and were fitted with an indwelling tail vein catheter for injections. As shown in Figure A-1, T1 mapping was performed at baseline and at 7, 14, 21, and 28 minutes after administering gadolinium-labeled albumin (4 mL/kg; Galbumin, BioPal, Worcester, MA) and, in a separate session, at the same times without administering contrast agent. Increase in coronary microvascular permeability was induced by intravenous administration of LNAME (2 mg/kg) and ET-1 (1 nmol/kg) as shown in Figure A-1. Control studies were performed without pharmacologically increasing permeability.

Session #1: Native T1



Session #2: Galbumin-enhanced T1

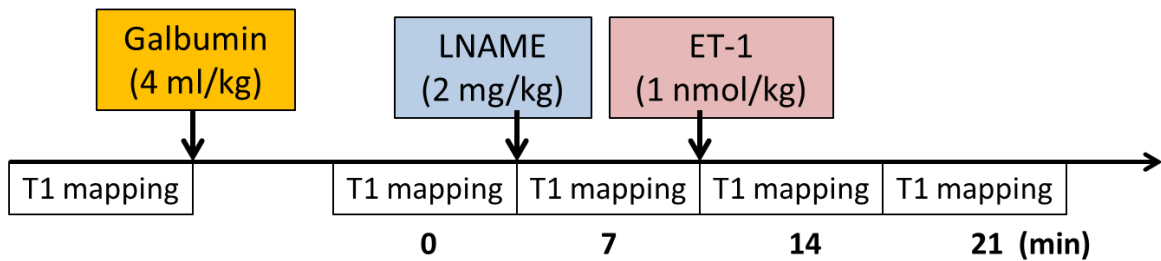


Figure A-1 Schematic timing diagram of the Galbumin T1 mapping experiments.

T1 mapping MRI was performed using a spiral Look-Locker T1-mapping method for mice combined with cardio-respiratory gating, as previously described [123]. The technique uses fuzzy-clustering of spiral k-space interleaves [129] to ensure accurate T1 estimation even with varying respiratory or heart rate. Imaging parameters included: TR = 7 s, TE = 0.67 ms, flip angle = 3°, field of view (FOV) = 30 x 30 mm², number of averages = 3, number of spiral interleaves = 84, interleaves per heartbeat = 3 and in-plane resolution = 0.23 x 0.23 mm². Using k_y-t undersampling with randomness and a low-rank compressed-sensing reconstruction [125], the acquisition was rate-2 accelerated, providing a scan time of 7 minutes.

The partition coefficient, defined as the ratio of contrast agent concentration in the myocardium to that in the blood, was calculated using the following equation and was used as a surrogate for microvascular permeability.

$$\lambda = \frac{R1(tissue)^{Post} - R1(tissue)^{Pre}}{R1(blood)^{Post} - R1(blood)^{Pre}}$$

Results

Figure A-2 shows example R1 (1/T1) maps acquired before and 14 minutes after injection of Gd-labeled albumin. Native T1 mapping after the injection of LNAME and ET-1 detected a transient increase in native T1 due to increase in interstitial fluid ($P < 0.05$), as shown in Figure A-3. T1 mapping before and after injecting Gd-labeled albumin detected a significant increase in the partition coefficient after administration of pharmacological agents compared to control (0.27 ± 0.017 LNAME and ET-1 vs. 0.21 ± 0.013 control; $p < 0.05$), reflecting the detection of the induced increase in microvascular permeability.

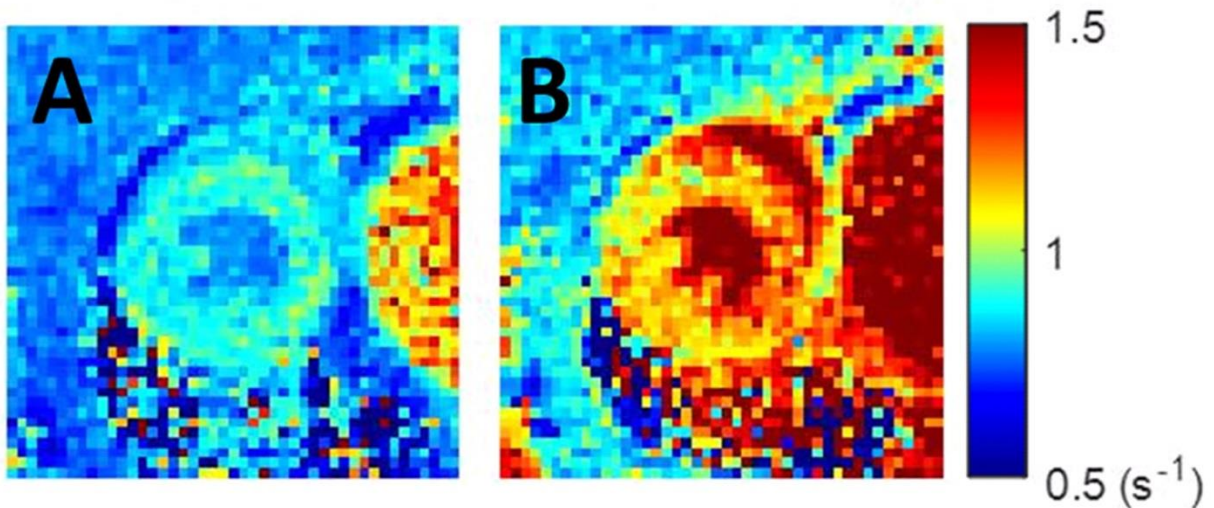


Figure A-2: Example R1 maps of the mouse heart before (A) and 14 minutes after iv injection of 4 mL/kg Gd-labeled albumin (B).

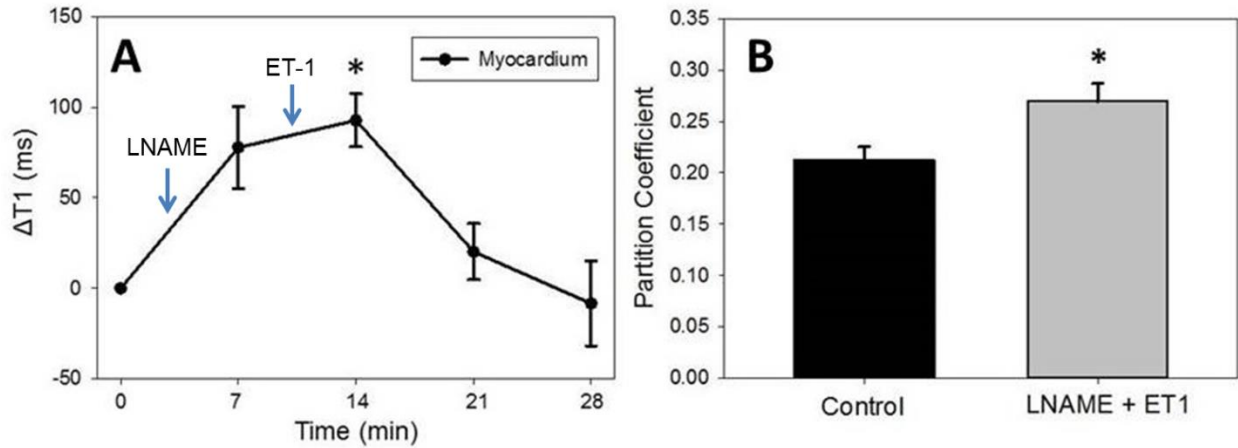


Figure A-3: (A) Native myocardial T1 values increase and return to baseline after iv injection of LNAME and ET-1. At the peak of the response (14 minutes), the injection of LNAME and ET-1 caused an average of 92 ms increase in native myocardial T1 (* $p < 0.05$ vs. baseline). (B) Without pharmacological agents, the partition coefficient of gadolinium-labeled albumin was 0.21 ± 0.017 and it increased to 0.27 ± 0.013 after administering LNAME and ET-1 (* $P < 0.05$ vs. control). All data shown are mean \pm standard error.

Conclusions

T1 mapping with gadolinium-labeled albumin can detect pharmacologically-induced changes in coronary microvascular permeability. These methods hold potential for the serial noninvasive assessment of the coronary microvasculature in preclinical models of heart disease and for studies evaluating potentially protective therapies for the microvasculature. Future work will investigate the use of clinically-applicable agents such as albumin-binding gadolinium (Ablavar, Lantheus, MA) as a means to potentially translate these methods for studies of coronary microvascular disease in human patients.

Appendix B: List of Publications

PUBLICATIONS:

1. **Cui SX** and Epstein FH. Self-gated SpASL: Improved Steady-Pulsed Arterial Spin Labeling using Retrospective Cardiac and Self-Navigated Respiratory Gating with Faster Looping Structure for Quantification of Myocardial Perfusion in Mice. *In Preparation*.
2. Kingsmore KM, Vaccari A, **Cui SX**, Epstein FH, Acton ST, Munson JM. MRI analysis to map interstitial flow in the brain tumor microenvironment. *Submitted to APL Bioengineering*.
3. **Cui SX** and Epstein FH. MRI assessment of coronary microvascular endothelial nitric oxide synthase function using myocardial T1 mapping. *Magn Reson Med* 2018 Apr;79(4):2246-2253.
4. Auger DA, Bilchick KC, Gonzalez JA, **Cui SX**, Holmes JW, Kramer CM, Salerno M, Epstein FH. Imaging left-ventricular mechanical activation in heart failure patients using cine DENSE MRI: Validation and implications for cardiac resynchronization therapy. *J Magn Reson Imaging* 2017;46(3):887-896.
5. Laughner JI, Marrus SB, Zellmer ER, Weinheimer CJ, MacEwan MR, **Cui SX**, Nerbonne JM, Efimov IR. A fully implantable pacemaker for the mouse: from battery to wireless power. *PLoS One* 2013;8(10):e76291.

FIRST-AUTHOR ORAL ABSTRACTS:

1. **Cui SX** and Epstein FH. Steady-State Pulsed Arterial Spin Labeling Is Faster and Provides Lower Variability for Quantification of Myocardial Perfusion Reserve in Mice Compared to Flow Alternating Inversion Recovery Look-Locker ASL. Abstract accepted for oral presentation at SCMR 2018 Annual Scientific Meeting, Barcelona, Spain.
2. **Cui SX** and Epstein FH. First-Pass Nitroxide-Enhanced MRI for Imaging Myocardial Perfusion without Gadolinium. Proc. ISMRM. 2017. 25; 2398.
3. **Cui SX** and Epstein FH. MRI Assessment of Coronary Endothelial Nitric Oxide Synthase (eNOS) Function Using T1 Mapping. Journal of Cardiovascular Magnetic Resonance, v. 19 (Suppl 1), p. O9, 2017. Winner of SCMR 2017 Early Career Award.
4. **Cui SX** and Epstein FH. MRI Assessment of Coronary Endothelial Function Using Native T1 Mapping with Nitric Oxide Synthase (NOS) Inhibition. Proc. ISMRM. 2016. 24; 4902.
5. **Cui SX**, French BA, Epstein FH. Detection of Increased Coronary Microvascular Permeability with MRI T1 mapping and Gadolinium-labeled Albumin. Journal of Cardiovascular Magnetic Resonance, v. 18 (Suppl 1), p. W3, 2016.
6. **Cui SX**, Bilchick KC, Epstein FH. Cine DENSE MRI Detects Delayed Mechanical Activation of the Left Ventricular Free Wall in a Canine Model of Heart Failure with Left Bundle Branch Block. Journal of Cardiovascular Magnetic Resonance, v. 16 (Suppl 1), p. O69, 2014.

FIRST-AUTHOR POSTERS ABSTRACTS

1. **Cui SX**, Roy RJ, French BA, Epstein FH. Dynamic Nitroxide-Enhanced MRI Detects Oxidative Stress in the Hearts of Mice Subject to Angiotensin II Infusion. Proc. ISMRM. 2017. 25; 7451.
2. **Cui SX** and Epstein FH. T1 Mapping with Nitric Oxide Synthase (NOS) Inhibition Detects Impaired Coronary Endothelial Function in Mice Fed a High Fat Diet. Proc. ISMRM. 2017. 25; 2387.
3. **Cui SX**, Gilliam AD, Bilchick KC, Epstein FH. Cine DENSE Strain Imaging of the Right Ventricle: Improved Methods and Initial Experience in Heart Failure. Journal of Cardiovascular Magnetic Resonance, v. 16 (Suppl 1), p. P4, 2014.

OTHER ABSTRACTS

1. Li J, Huang Q, **Cui SX**, Chordia M, Roy J, Kramer CM, Epstein FH, Keller S, Kundu B. Metabolic, Functional and Structural Remodeling of Spontaneously Hypertensive Rat Hearts Over Time. SNMMI Annual Meeting. Philadelphia, Pennsylvania, June 23-26, 2018
2. Auger DA, **Cui SX**, Chen X, Gonzalez JA, Kramer CM, Bilchick KC, Epstein FH. Cine DENSE MRI of mechanical activation in heart failure patients referred for cardiac resynchronization therapy. Journal of Cardiovascular Magnetic Resonance, v. 18 (Suppl 1), p. P215, 2016

3. Kingsmore K, **Cui SX**, Epstein FH, Munson J. Role of Interstitial Flow in Glioma Microenvironment as Assessed by Dynamic Contrast Enhanced MRI. Biomedical Engineering Society Annual Meeting. Tampa Florida, October 7-10 2015.
4. Auger DA, **Cui SX**, Chen X, Holmes JW, Bilchick KC, Epstein FH. Mechanical Activation Time Mapping in Heart Failure Patients with and without Myocardial Scar using Cine DENSE MRI. Proc. ISMRM. 2015. 23; 0187.
5. Auger DA, **Cui SX**, Chen X, Bilchick KC, Epstein FH. Cardiac mechanical activation mapping in heart failure patients with left bundle branch block using cine DENSE MRI. Journal of Cardiovascular Magnetic Resonance, v. 17 (Suppl 1), p. O43, 2015.
6. Auger DA, **Cui SX**, Chen X, Bilchick KC, Epstein FH. CMR Mapping of Mechanical Activation Time in Patients with Heart Failure and Left Bundle Branch Block: Methods and Initial Results. American Heart Association Scientific Sessions. November 2014.
7. Auger DA, **Cui SX**, Chen X, Bilchick KC, Epstein FH. Magnetic Resonance Imaging of Cardiac Activation in Heart Failure Patients with Left Bundle Branch Block. Biomedical Engineering Society Annual Meeting. Tampa Florida, September 2014.
8. Bilchick KC, Kuruvilla S, Hamirani YS, Ramachandran R, Clarke S, **Cui SX**, Salerno M, Holmes J, Kramer CM, Epstein FH. Electromechanical and Scar Characteristics at Left Ventricular Lead Implant Site in the Context of Overall Dyssynchrony with Cine DENSE Predict Cardiac Resynchronization Therapy Outcomes. Journal of Cardiovascular Magnetic Resonance, v. 16 (Suppl 1), p. O53, 2014.
9. Auger DA, **Cui SX**, Chen X, Bilchick KC, Epstein FH. CMR Mapping of Mechanical Activation Time in Patients with Heart Failure and Left Bundle Branch Block: Methods and Initial Results. January 2014.

References

1. Safdar, B., et al., *Prevalence and characteristics of coronary microvascular dysfunction among chest pain patients in the emergency department*. Eur Heart J Acute Cardiovasc Care, 2018: p. 2048872618764418.
2. Selker, H.P., et al., *Use of the acute cardiac ischemia time-insensitive predictive instrument (ACI-TIPI) to assist with triage of patients with chest pain or other symptoms suggestive of acute cardiac ischemia. A multicenter, controlled clinical trial*. Ann Intern Med, 1998. **129**(11): p. 845-55.
3. Farrehi, P.M., et al., *Frequency of negative coronary arteriographic findings in patients with chest pain is related to community practice patterns*. Am J Manag Care, 2002. **8**(7): p. 643-8.
4. Bradley, S.M., et al., *Normal coronary rates for elective angiography in the Veterans Affairs Healthcare System: insights from the VA CART program (veterans affairs clinical assessment reporting and tracking)*. J Am Coll Cardiol, 2014. **63**(5): p. 417-26.
5. Radico, F., et al., *Angina Pectoris and Myocardial Ischemia in the Absence of Obstructive Coronary Artery Disease: Practical Considerations for Diagnostic Tests*. JACC: Cardiovascular Interventions, 2014. **7**(5): p. 453-463.
6. Jespersen, L., et al., *Stable angina pectoris with no obstructive coronary artery disease is associated with increased risks of major adverse cardiovascular events*. European Heart Journal, 2012. **33**(6): p. 734-744.
7. Reis, S.E., et al., *Coronary microvascular dysfunction is highly prevalent in women with chest pain in the absence of coronary artery disease: Results from the NHLBI WISE study*. American Heart Journal. **141**(5): p. 735-741.

8. Hasdai, D., et al., *Prevalence of coronary blood flow reserve abnormalities among patients with nonobstructive coronary artery disease and chest pain*. Mayo Clin Proc, 1998. **73**(12): p. 1133-40.
9. Sara, J.D., et al., *Prevalence of Coronary Microvascular Dysfunction Among Patients With Chest Pain and Nonobstructive Coronary Artery Disease*. JACC Cardiovasc Interv, 2015. **8**(11): p. 1445-53.
10. Murthy, V.L., et al., *Effects of sex on coronary microvascular dysfunction and cardiac outcomes*. Circulation, 2014. **129**(24): p. 2518-27.
11. Pepine, C.J., et al., *Coronary microvascular reactivity to adenosine predicts adverse outcome in women evaluated for suspected ischemia results from the National Heart, Lung and Blood Institute WISE (Women's Ischemia Syndrome Evaluation) study*. J Am Coll Cardiol, 2010. **55**(25): p. 2825-32.
12. Taqueti, V.R., et al., *Global coronary flow reserve is associated with adverse cardiovascular events independently of luminal angiographic severity and modifies the effect of early revascularization*. Circulation, 2015. **131**(1): p. 19-27.
13. Britten, M.B., A.M. Zeiher, and V. Schachinger, *Microvascular dysfunction in angiographically normal or mildly diseased coronary arteries predicts adverse cardiovascular long-term outcome*. Coron Artery Dis, 2004. **15**(5): p. 259-64.
14. Gulati, M., et al., *Adverse cardiovascular outcomes in women with nonobstructive coronary artery disease: a report from the Women's Ischemia Syndrome Evaluation Study and the St James Women Take Heart Project*. Arch Intern Med, 2009. **169**(9): p. 843-50.
15. Murthy, V.L., et al., *Association between coronary vascular dysfunction and cardiac mortality in patients with and without diabetes mellitus*. Circulation, 2012. **126**(15): p. 1858-68.

16. Johnson, B.D., et al., *Prognosis in Women With Myocardial Ischemia in the Absence of Obstructive Coronary Disease*. Results From the National Institutes of Health–National Heart, Lung, and Blood Institute–Sponsored Women’s Ischemia Syndrome Evaluation (WISE), 2004. **109**(24): p. 2993-2999.
17. Olson, M.B., et al., *Symptoms, myocardial ischaemia and quality of life in women:Results from the NHLBI-sponsored WISE Study*. European Heart Journal, 2003. **24**(16): p. 1506-1514.
18. Sicari, R., et al., *Additive prognostic value of coronary flow reserve in patients with chest pain syndrome and normal or near-normal coronary arteries*. Am J Cardiol, 2009. **103**(5): p. 626-31.
19. Kaufmann, P.A., et al., *Coronary heart disease in smokers: vitamin C restores coronary microcirculatory function*. Circulation, 2000. **102**(11): p. 1233-8.
20. Tona, F., et al., *Systemic inflammation is related to coronary microvascular dysfunction in obese patients without obstructive coronary disease*. Nutr Metab Cardiovasc Dis, 2014. **24**(4): p. 447-53.
21. Nitenberg, A., et al., *Impairment of coronary vascular reserve and ACh-induced coronary vasodilation in diabetic patients with angiographically normal coronary arteries and normal left ventricular systolic function*. Diabetes, 1993. **42**(7): p. 1017-25.
22. Yokoyama, I., et al., *Reduced myocardial flow reserve in non-insulin-dependent diabetes mellitus*. J Am Coll Cardiol, 1997. **30**(6): p. 1472-7.
23. Rizzoni, D., et al., *Relationships between coronary flow vasodilator capacity and small artery remodelling in hypertensive patients*. J Hypertens, 2003. **21**(3): p. 625-31.
24. Schwartzkopff, B., et al., *Structural and functional alterations of the intramyocardial coronary arterioles in patients with arterial hypertension*. Circulation, 1993. **88**(3): p. 993-1003.

25. Kaufmann, P.A., et al., *Low density lipoprotein cholesterol and coronary microvascular dysfunction in hypercholesterolemia*. J Am Coll Cardiol, 2000. **36**(1): p. 103-9.
26. Marzilli, M., et al., *Obstructive coronary atherosclerosis and ischemic heart disease: an elusive link!* J Am Coll Cardiol, 2012. **60**(11): p. 951-6.
27. Paulus, W.J. and C. Tschöpe, *A novel paradigm for heart failure with preserved ejection fraction*. Journal of the American College of Cardiology, 2013. **62**(4): p. 263-271.
28. Giamouzis, G., E.B. Schelbert, and J. Butler, *Growing evidence linking microvascular dysfunction with heart failure with preserved ejection Fraction*. 2016, Am Heart Assoc.
29. Camici, P.G. and F. Crea, *Coronary microvascular dysfunction*. N Engl J Med, 2007. **356**(8): p. 830-40.
30. Zeiher, A.M., et al., *Coronary vasomotion in response to sympathetic stimulation in humans: Importance of the functional integrity of the endothelium*. Journal of the American College of Cardiology, 1989. **14**(5): p. 1181-1190.
31. Feliciano, L. and R.J. Henning, *Coronary artery blood flow: physiologic and pathophysiologic regulation*. Clin Cardiol, 1999. **22**(12): p. 775-86.
32. Murray, K.J., *Cyclic AMP and mechanisms of vasodilation*. Pharmacol Ther, 1990. **47**(3): p. 329-45.
33. Blaise, G.A., D.J. Stewart, and M.J. Guerard, *Acetylcholine stimulates release of endothelium-derived relaxing factor in coronary arteries of human organ donors*. Can J Cardiol, 1993. **9**(9): p. 813-20.
34. Fearon, W.F., et al., *Novel index for invasively assessing the coronary microcirculation*. Circulation, 2003. **107**(25): p. 3129-32.
35. De Bruyne, B., et al., *Coronary thermodilution to assess flow reserve: experimental validation*. Circulation, 2001. **104**(17): p. 2003-6.

36. Pijls, N.H., et al., *Coronary thermodilution to assess flow reserve: validation in humans*. *Circulation*, 2002. **105**(21): p. 2482-6.
37. Williams, R.P., et al., *Doppler Versus Thermodilution-Derived Coronary Microvascular Resistance to Predict Coronary Microvascular Dysfunction in Patients With Acute Myocardial Infarction or Stable Angina Pectoris*. *Am J Cardiol*, 2018. **121**(1): p. 1-8.
38. Prior, J.O., et al., *Quantification of myocardial blood flow with ⁸²Rb positron emission tomography: clinical validation with ¹⁵O-water*. *Eur J Nucl Med Mol Imaging*, 2012. **39**(6): p. 1037-47.
39. Wohrle, J., et al., *Myocardial perfusion reserve in cardiovascular magnetic resonance: Correlation to coronary microvascular dysfunction*. *J Cardiovasc Magn Reson*, 2006. **8**(6): p. 781-7.
40. Valenta, I., et al., *Quantitative PET/CT measures of myocardial flow reserve and atherosclerosis for cardiac risk assessment and predicting adverse patient outcomes*. *Curr Cardiol Rep*, 2013. **15**(3): p. 344.
41. Doyle, M., et al., *Prognostic value of global MR myocardial perfusion imaging in women with suspected myocardial ischemia and no obstructive coronary disease: results from the NHLBI-sponsored WISE (Women's Ischemia Syndrome Evaluation) study*. *JACC Cardiovasc Imaging*, 2010. **3**(10): p. 1030-6.
42. Freed, B.H., et al., *Prognostic value of normal regadenoson stress perfusion cardiovascular magnetic resonance*. *Journal of Cardiovascular Magnetic Resonance*, 2013. **15**(1): p. 108.
43. Vogel, R., et al., *The quantification of absolute myocardial perfusion in humans by contrast echocardiography: algorithm and validation*. *J Am Coll Cardiol*, 2005. **45**(5): p. 754-62.

44. Youn, H.J. and E. Foster, *Demonstration of coronary artery flow using transthoracic Doppler echocardiography*. J Am Soc Echocardiogr, 2004. **17**(2): p. 178-85.
45. Marinescu, M.A., et al., *Coronary microvascular dysfunction, microvascular angina, and treatment strategies*. JACC Cardiovasc Imaging, 2015. **8**(2): p. 210-20.
46. Kaski, J.C., et al., *Effects of angiotensin-converting enzyme inhibition on exercise-induced angina and ST segment depression in patients with microvascular angina*. J Am Coll Cardiol, 1994. **23**(3): p. 652-7.
47. Motz, W. and B.E. Strauer, *Improvement of coronary flow reserve after long-term therapy with enalapril*. Hypertension, 1996. **27**(5): p. 1031-8.
48. Bender, S.B., G. Jia, and J.R. Sowers, *Mineralocorticoid Receptors: An Appealing Target to Treat Coronary Microvascular Dysfunction in Diabetes*. Diabetes, 2015. **64**(1): p. 3-5.
49. Bavry, A.A., et al., *Aldosterone inhibition and coronary endothelial function in women without obstructive coronary artery disease: An ancillary study of the NHLBI-sponsored Women's Ischemia Syndrome Evaluation (WISE)*. American heart journal, 2014. **167**(6): p. 826-832.
50. Denardo, S.J., et al., *Effect of phosphodiesterase type 5 inhibition on microvascular coronary dysfunction in women: a Women's Ischemia Syndrome Evaluation (WISE) ancillary study*. Clin Cardiol, 2011. **34**(8): p. 483-7.
51. Egashira, K., et al., *Effects of L-arginine supplementation on endothelium-dependent coronary vasodilation in patients with angina pectoris and normal coronary arteriograms*. Circulation, 1996. **94**(2): p. 130-4.
52. Gellman, J., et al., *L-arginine ameliorates the abnormal sympathetic response of the dysfunctional human coronary microvasculature*. Angiology, 2004. **55**(1): p. 1-8.

53. Houghton, J.L., et al., *Cholesterol lowering with pravastatin improves resistance artery endothelial function: report of six subjects with normal coronary arteriograms*. Chest, 2000. **118**(3): p. 756-60.
54. Zhang, X., et al., *Effects of combination of statin and calcium channel blocker in patients with cardiac syndrome X*. Coron Artery Dis, 2014. **25**(1): p. 40-4.
55. Eshtehardi, P., et al., *Effect of intensive atorvastatin therapy on coronary atherosclerosis progression, composition, arterial remodeling, and microvascular function*. J Invasive Cardiol, 2012. **24**(10): p. 522-9.
56. Caliskan, M., et al., *Effects of atorvastatin on coronary flow reserve in patients with slow coronary flow*. Clin Cardiol, 2007. **30**(9): p. 475-9.
57. Yutzey, K.E. and J. Robbins, *Principles of Genetic Murine Models for Cardiac Disease*. Circulation, 2007. **115**(6): p. 792-799.
58. Zaragoza, C., et al., *Animal models of cardiovascular diseases*. J Biomed Biotechnol, 2011. **2011**: p. 497841.
59. Aoqui, C., et al., *Microvascular dysfunction in the course of metabolic syndrome induced by high-fat diet*. Cardiovascular Diabetology, 2014. **13**: p. 31-31.
60. Stokes, K.Y., et al., *Dietary nitrite prevents hypercholesterolemic microvascular inflammation and reverses endothelial dysfunction*. Am J Physiol Heart Circ Physiol, 2009. **296**(5): p. H1281-8.
61. Abdesselam, I., et al., *Time course of cardiometabolic alterations in a high fat high sucrose diet mice model and improvement after GLP-1 analog treatment using multimodal cardiovascular magnetic resonance*. Journal of Cardiovascular Magnetic Resonance, 2015. **17**: p. 95.
62. Kibel, A., et al., *Coronary microvascular dysfunction in diabetes mellitus*. Journal of International Medical Research, 2017. **45**(6): p. 1901-1929.

63. Van den Bergh, A., W. Flameng, and P. Herijgers, *Type II diabetic mice exhibit contractile dysfunction but maintain cardiac output by favourable loading conditions*. Eur J Heart Fail, 2006. **8**(8): p. 777-83.
64. Choi, S.K., et al., *Poly(ADP-ribose) polymerase 1 inhibition improves coronary arteriole function in type 2 diabetes mellitus*. Hypertension, 2012. **59**(5): p. 1060-8.
65. Moien-Afshari, F., et al., *Exercise restores coronary vascular function independent of myogenic tone or hyperglycemic status in db/db mice*. American Journal of Physiology-Heart and Circulatory Physiology, 2008. **295**(4): p. H1470-H1480.
66. DelloStritto, D.J., et al., *Differential regulation of TRPV1 channels by H₂O₂: implications for diabetic microvascular dysfunction*. Basic Res Cardiol, 2016. **111**(2): p. 21.
67. Kaul, D.K., et al., *Arginine therapy of transgenic-knockout sickle mice improves microvascular function by reducing non-nitric oxide vasodilators, hemolysis, and oxidative stress*. Am J Physiol Heart Circ Physiol, 2008. **295**(1): p. H39-47.
68. Neglia, D., et al., *Perindopril and indapamide reverse coronary microvascular remodelling and improve flow in arterial hypertension*. J Hypertens, 2011. **29**(2): p. 364-72.
69. Celermajer, D.S., et al., *Cigarette smoking is associated with dose-related and potentially reversible impairment of endothelium-dependent dilation in healthy young adults*. Circulation, 1993. **88**(5 Pt 1): p. 2149-55.
70. Zeiher, A.M., V. Schachinger, and J. Minners, *Long-term cigarette smoking impairs endothelium-dependent coronary arterial vasodilator function*. Circulation, 1995. **92**(5): p. 1094-100.
71. Sorensen, K.E., et al., *Impairment of endothelium-dependent dilation is an early event in children with familial hypercholesterolemia and is related to the lipoprotein(a) level*. J Clin Invest, 1994. **93**(1): p. 50-5.

72. Spieker, L.E., et al., *High-density lipoprotein restores endothelial function in hypercholesterolemic men*. *Circulation*, 2002. **105**(12): p. 1399-402.
73. Linder, L., et al., *Indirect evidence for release of endothelium-derived relaxing factor in human forearm circulation in vivo. Blunted response in essential hypertension*. *Circulation*, 1990. **81**(6): p. 1762-7.
74. Panza, J.A., et al., *Abnormal endothelium-dependent vascular relaxation in patients with essential hypertension*. *N Engl J Med*, 1990. **323**(1): p. 22-7.
75. Treasure, C.B., et al., *Epicardial coronary artery responses to acetylcholine are impaired in hypertensive patients*. *Circ Res*, 1992. **71**(4): p. 776-81.
76. Makimattila, S., et al., *Chronic hyperglycemia impairs endothelial function and insulin sensitivity via different mechanisms in insulin-dependent diabetes mellitus*. *Circulation*, 1996. **94**(6): p. 1276-82.
77. Celermajer, D.S., et al., *Non-invasive detection of endothelial dysfunction in children and adults at risk of atherosclerosis*. *Lancet*, 1992. **340**(8828): p. 1111-5.
78. Al Suwaidi, J., et al., *Obesity is independently associated with coronary endothelial dysfunction in patients with normal or mildly diseased coronary arteries*. *J Am Coll Cardiol*, 2001. **37**(6): p. 1523-8.
79. Steinberg, H.O., et al., *Obesity/insulin resistance is associated with endothelial dysfunction. Implications for the syndrome of insulin resistance*. *J Clin Invest*, 1996. **97**(11): p. 2601-10.
80. Fichtlscherer, S., et al., *Elevated C-reactive protein levels and impaired endothelial vasoreactivity in patients with coronary artery disease*. *Circulation*, 2000. **102**(9): p. 1000-6.
81. Hurlimann, D., et al., *Anti-tumor necrosis factor-alpha treatment improves endothelial function in patients with rheumatoid arthritis*. *Circulation*, 2002. **106**(17): p. 2184-7.

82. Flammer, A.J., et al., *Angiotensin-converting enzyme inhibition improves vascular function in rheumatoid arthritis*. *Circulation*, 2008. **117**(17): p. 2262-9.
83. Prasad, A., et al., *Predisposition to atherosclerosis by infections: role of endothelial dysfunction*. *Circulation*, 2002. **106**(2): p. 184-90.
84. Bonetti, P.O., L.O. Lerman, and A. Lerman, *Endothelial dysfunction: a marker of atherosclerotic risk*. *Arterioscler Thromb Vasc Biol*, 2003. **23**(2): p. 168-75.
85. Hadi, H.A., C.S. Carr, and J. Al Suwaidi, *Endothelial dysfunction: cardiovascular risk factors, therapy, and outcome*. *Vasc Health Risk Manag*, 2005. **1**(3): p. 183-98.
86. Suwaidi, J.A., et al., *Long-term follow-up of patients with mild coronary artery disease and endothelial dysfunction*. *Circulation*, 2000. **101**(9): p. 948-54.
87. Brunner, H., et al., *Endothelial function and dysfunction. Part II: Association with cardiovascular risk factors and diseases. A statement by the Working Group on Endothelins and Endothelial Factors of the European Society of Hypertension*. *J Hypertens*, 2005. **23**(2): p. 233-46.
88. Gokce N, Keaney JK Jr., and V. JA, *Endotheliopathies: Clinical manifestations of endothelial dysfunction*, in *Thrombosis and Hemorrhage*, L. J and S. Al, Editors. 1998, Williams and Wilkins. p. 901-924.
89. Levine, G.N., J.F. Keaney, Jr., and J.A. Vita, *Cholesterol reduction in cardiovascular disease. Clinical benefits and possible mechanisms*. *N Engl J Med*, 1995. **332**(8): p. 512-21.
90. Vita, J.A. and J.F. Keaney, Jr., *Endothelial function: a barometer for cardiovascular risk?* *Circulation*, 2002. **106**(6): p. 640-2.
91. Kinlay, S. and P. Ganz, *Role of endothelial dysfunction in coronary artery disease and implications for therapy*. *Am J Cardiol*, 1997. **80**(9A): p. 11I-16I.

92. Halcox, J.P., et al., *Prognostic value of coronary vascular endothelial dysfunction*. *Circulation*, 2002. **106**(6): p. 653-8.
93. Heitzer, T., et al., *Endothelial dysfunction, oxidative stress, and risk of cardiovascular events in patients with coronary artery disease*. *Circulation*, 2001. **104**(22): p. 2673-8.
94. Neunteufl, T., et al., *Late prognostic value of flow-mediated dilation in the brachial artery of patients with chest pain*. *Am J Cardiol*, 2000. **86**(2): p. 207-10.
95. Schachinger, V., M.B. Britten, and A.M. Zeiher, *Prognostic impact of coronary vasodilator dysfunction on adverse long-term outcome of coronary heart disease*. *Circulation*, 2000. **101**(16): p. 1899-906.
96. von Mering, G.O., et al., *Abnormal coronary vasomotion as a prognostic indicator of cardiovascular events in women: results from the National Heart, Lung, and Blood Institute-Sponsored Women's Ischemia Syndrome Evaluation (WISE)*. *Circulation*, 2004. **109**(6): p. 722-5.
97. Lee, B.K., et al., *Invasive evaluation of patients with angina in the absence of obstructive coronary artery disease*. *Circulation*, 2015. **131**(12): p. 1054-60.
98. Ong, P., et al., *3-Year Follow-Up of Patients With Coronary Artery Spasm as Cause of Acute Coronary Syndrome: The CASPAR (Coronary Artery Spasm in Patients With Acute Coronary Syndrome) Study Follow-Up*. *Journal of the American College of Cardiology*, 2011. **57**(2): p. 147-152.
99. Kuvin, J.T., et al., *Assessment of peripheral vascular endothelial function with finger arterial pulse wave amplitude*. *Am Heart J*, 2003. **146**(1): p. 168-74.
100. Yeboah, J., et al., *Comparison of novel risk markers for improvement in cardiovascular risk assessment in intermediate-risk individuals*. *JAMA*, 2012. **308**(8): p. 788-95.
101. Anderson, T.J., et al., *Close relation of endothelial function in the human coronary and peripheral circulations*. *J Am Coll Cardiol*, 1995. **26**(5): p. 1235-41.

102. Ludmer, P.L., et al., *Paradoxical vasoconstriction induced by acetylcholine in atherosclerotic coronary arteries*. N Engl J Med, 1986. **315**(17): p. 1046-51.
103. Salerno, M. and G.A. Beller, *Noninvasive assessment of myocardial perfusion*. Circ Cardiovasc Imaging, 2009. **2**(5): p. 412-24.
104. Hays, A.G., et al., *Noninvasive visualization of coronary artery endothelial function in healthy subjects and in patients with coronary artery disease*. J Am Coll Cardiol, 2010. **56**(20): p. 1657-65.
105. Forstermann, U. and T. Munzel, *Endothelial nitric oxide synthase in vascular disease: from marvel to menace*. Circulation, 2006. **113**(13): p. 1708-14.
106. Filep, J.G., E. Foldes-Filep, and P. Sirois, *Nitric oxide modulates vascular permeability in the rat coronary circulation*. Br J Pharmacol, 1993. **108**(2): p. 323-6.
107. Kubes, P. and D.N. Granger, *Nitric oxide modulates microvascular permeability*. Am J Physiol, 1992. **262**(2 Pt 2): p. H611-5.
108. Kurose, I., et al., *Modulation of ischemia/reperfusion-induced microvascular dysfunction by nitric oxide*. Circ Res, 1994. **74**(3): p. 376-82.
109. Drexler, H., *Endothelial dysfunction: clinical implications*. Prog Cardiovasc Dis, 1997. **39**(4): p. 287-324.
110. Lum, H. and K.A. Roebuck, *Oxidant stress and endothelial cell dysfunction*. Am J Physiol Cell Physiol, 2001. **280**(4): p. C719-41.
111. Radu, M. and J. Chernoff, *An in vivo Assay to Test Blood Vessel Permeability*. J Vis Exp, 2013(73).
112. Bottomley, P.A., et al., *A review of normal tissue hydrogen NMR relaxation times and relaxation mechanisms from 1-100 MHz: dependence on tissue type, NMR frequency, temperature, species, excision, and age*. Med Phys, 1984. **11**(4): p. 425-48.

113. Ferreira, V.M., et al., *Non-contrast T1-mapping detects acute myocardial edema with high diagnostic accuracy: a comparison to T2-weighted cardiovascular magnetic resonance*. J Cardiovasc Magn Reson, 2012. **14**: p. 42.
114. Williams, E.S., et al., *Prolongation of proton spin lattice relaxation times in regionally ischemic tissue from dog hearts*. J Nucl Med, 1980. **21**(5): p. 449-53.
115. Des Prez, R.D., et al., *Cost-effectiveness of myocardial perfusion imaging: a summary of the currently available literature*. J Nucl Cardiol, 2005. **12**(6): p. 750-9.
116. McCrohon, J.A., et al., *Adjunctive role of cardiovascular magnetic resonance in the assessment of patients with inferior attenuation on myocardial perfusion SPECT*. J Cardiovasc Magn Reson, 2005. **7**(2): p. 377-82.
117. Freed, B.H., et al., *Prognostic value of normal regadenoson stress perfusion cardiovascular magnetic resonance*. J Cardiovasc Magn Reson, 2013. **15**: p. 108.
118. Gerber, B.L., et al., *Myocardial first-pass perfusion cardiovascular magnetic resonance: history, theory, and current state of the art*. Journal of Cardiovascular Magnetic Resonance, 2008. **10**(1): p. 18.
119. Jerosch-Herold, M., *Quantification of myocardial perfusion by cardiovascular magnetic resonance*. Journal of Cardiovascular Magnetic Resonance, 2010. **12**(1): p. 57.
120. Naresh, N.K., et al., *Accelerated dual-contrast first-pass perfusion MRI of the mouse heart: development and application to diet-induced obese mice*. Magn Reson Med, 2015. **73**(3): p. 1237-45.
121. Makowski, M., et al., *First-Pass Contrast-Enhanced Myocardial Perfusion MRI in Mice on a 3-T Clinical MR Scanner*. Magnetic Resonance in Medicine, 2010. **64**(6): p. 1592-1598.
122. Coolen, B.F., et al., *Mouse myocardial first-pass perfusion MR imaging*. Magn Reson Med, 2010. **64**(6): p. 1658-63.

123. Naresh, N.K., et al., *Repeatability and variability of myocardial perfusion imaging techniques in mice: Comparison of arterial spin labeling and first-pass contrast-enhanced MRI*. Magn Reson Med, 2015.
124. Christian, T.F., et al., *Absolute myocardial perfusion in canines measured by using dual-bolus first-pass MR imaging*. Radiology, 2004. **232**(3): p. 677-84.
125. Chen, X., et al., *Motion-compensated compressed sensing for dynamic contrast-enhanced MRI using regional spatiotemporal sparsity and region tracking: block low-rank sparsity with motion-guidance (BLOSM)*. Magn Reson Med, 2014. **72**(4): p. 1028-38.
126. Jerosch-Herold, M., N. Wilke, and A.E. Stillman, *Magnetic resonance quantification of the myocardial perfusion reserve with a Fermi function model for constrained deconvolution*. Med Phys, 1998. **25**(1): p. 73-84.
127. Cernicanu, A. and L. Axel, *Theory-based signal calibration with single-point T1 measurements for first-pass quantitative perfusion MRI studies*. Acad Radiol, 2006. **13**(6): p. 686-93.
128. Kober, F., et al., *High-resolution myocardial perfusion mapping in small animals in vivo by spin-labeling gradient-echo imaging*. Magn Reson Med, 2004. **51**(1): p. 62-7.
129. Vandsburger, M.H., et al., *Improved arterial spin labeling after myocardial infarction in mice using cardiac and respiratory gated look-locker imaging with fuzzy C-means clustering*. Magn Reson Med, 2010. **63**(3): p. 648-57.
130. Kober, F., et al., *Myocardial arterial spin labeling*. Journal of Cardiovascular Magnetic Resonance, 2016. **18**(1): p. 22.
131. Belle, V., et al., *In vivo quantitative mapping of cardiac perfusion in rats using a noninvasive MR spin-labeling method*. J Magn Reson Imaging, 1998. **8**(6): p. 1240-5.

132. Troalen, T., et al., *Cine-ASL: A steady-pulsed arterial spin labeling method for myocardial perfusion mapping in mice. Part I. Experimental study*. Magnetic resonance in medicine, 2013. **70**(5): p. 1389-1398.
133. Ohara, Y., T.E. Peterson, and D.G. Harrison, *Hypercholesterolemia increases endothelial superoxide anion production*. Journal of Clinical Investigation, 1993. **91**(6): p. 2546.
134. Hink, U., et al., *Mechanisms underlying endothelial dysfunction in diabetes mellitus*. Circulation research, 2001. **88**(2): p. e14-e22.
135. Kerr, S., et al., *Superoxide anion production is increased in a model of genetic hypertension*. Hypertension, 1999. **33**(6): p. 1353-1358.
136. Förstermann, U. and T. Münzel, *Endothelial nitric oxide synthase in vascular disease: from marvel to menace*. Circulation, 2006. **113**(13): p. 1708-14.
137. Baldwin, A.L., G. Thurston, and H. al Naemi, *Inhibition of nitric oxide synthesis increases venular permeability and alters endothelial actin cytoskeleton*. Am J Physiol, 1998. **274**(5 Pt 2): p. H1776-84.
138. Predescu, D., et al., *Constitutive eNOS-derived nitric oxide is a determinant of endothelial junctional integrity*. Am J Physiol Lung Cell Mol Physiol, 2005. **289**(3): p. L371-81.
139. He, P., B. Liu, and F.E. Curry, *Effect of nitric oxide synthase inhibitors on endothelial [Ca²⁺]_i and microvessel permeability*. Am J Physiol, 1997. **272**(1 Pt 2): p. H176-85.
140. Garcia, J.L., et al., *Effects of nitric oxide synthesis inhibition on the goat coronary circulation under basal conditions and after vasodilator stimulation*. Br J Pharmacol, 1992. **106**(3): p. 563-7.
141. Imanishi, T., et al., *Renin inhibitor aliskiren improves impaired nitric oxide bioavailability and protects against atherosclerotic changes*. Hypertension, 2008. **52**(3): p. 563-72.

142. Frandsenn, U., et al., *Exercise-induced hyperaemia and leg oxygen uptake are not altered during effective inhibition of nitric oxide synthase with N(G)-nitro-L-arginine methyl ester in humans*. J Physiol, 2001. **531**(Pt 1): p. 257-64.
143. Liu, A., et al., *Adenosine Stress and Rest T1 Mapping Can Differentiate Between Ischemic, Infarcted, Remote, and Normal Myocardium Without the Need for Gadolinium Contrast Agents*. Jacc-Cardiovascular Imaging, 2016. **9**(1): p. 27-36.
144. Calligaris, S.D., et al., *Mice long-term high-fat diet feeding recapitulates human cardiovascular alterations: an animal model to study the early phases of diabetic cardiomyopathy*. PLoS One, 2013. **8**(4): p. e60931.
145. Naresh, N.K., et al., *Cardiovascular magnetic resonance detects the progression of impaired myocardial perfusion reserve and increased left-ventricular mass in mice fed a high-fat diet*. J Cardiovasc Magn Reson, 2016. **18**(1): p. 53.
146. Ketonen, J., T. Pilvi, and E. Mervaala, *Caloric restriction reverses high-fat diet-induced endothelial dysfunction and vascular superoxide production in C57Bl/6 mice*. Heart Vessels, 2010. **25**(3): p. 254-62.
147. Molnar, J., et al., *Diabetes induces endothelial dysfunction but does not increase neointimal formation in high-fat diet fed C57BL/6J mice*. Circ Res, 2005. **96**(11): p. 1178-84.
148. Kobayasi, R., et al., *Oxidative stress and inflammatory mediators contribute to endothelial dysfunction in high-fat diet-induced obesity in mice*. J Hypertens, 2010. **28**(10): p. 2111-9.
149. Erdmann, A.J., 3rd, et al., *Effect of increased vascular pressure on lung fluid balance in unanesthetized sheep*. Circ Res, 1975. **37**(3): p. 271-84.
150. Bhattacharya, M., et al., *Negative-Pressure Pulmonary Edema*. Chest, 2016. **150**(4): p. 927-933.

151. Zhang, W., et al., *Vascular perfusion limits mesenteric lymph flow during anaphylactic hypotension in rats*. *Am J Physiol Regul Integr Comp Physiol*, 2012. **302**(10): p. R1191-6.
152. Alheid, U., J.C. Frölich, and U. Förstermann, *Endothelium-derived relaxing factor from cultured human endothelial cells inhibits aggregation of human platelets*. *Thrombosis research*, 1987. **47**(5): p. 561-571.
153. Busse, R., A. Lackhoff, and E. Bassenge, *Endothelium-derived relaxant factor inhibits platelet activation*. *Naunyn-Schmiedeberg's archives of pharmacology*, 1987. **336**(5): p. 566-571.
154. Radomski, M.W., R.M. Palmer, and S. Moncada, *The anti-aggregating properties of vascular endothelium: interactions between prostacyclin and nitric oxide*. *Br J Pharmacol*, 1987. **92**(3): p. 639-46.
155. Garg, U.C. and A. Hassid, *Nitric oxide-generating vasodilators and 8-bromo-cyclic guanosine monophosphate inhibit mitogenesis and proliferation of cultured rat vascular smooth muscle cells*. *Journal of Clinical Investigation*, 1989. **83**(5): p. 1774.
156. Nunokawa, Y. and S. Tanaka, *Interferon- γ inhibits proliferation of rat vascular smooth muscle cells by nitric oxide generation*. *Biochemical and biophysical research communications*, 1992. **188**(1): p. 409-415.
157. Nakaki, T., M. Nakayama, and R. Kato, *Inhibition by nitric oxide and nitric oxide-producing vasodilators of DNA synthesis in vascular smooth muscle cells*. *European Journal of Pharmacology: Molecular Pharmacology*, 1990. **189**(6): p. 347-353.
158. Arndt, H., C.W. Smith, and D.N. Granger, *Leukocyte-endothelial cell adhesion in spontaneously hypertensive and normotensive rats*. *Hypertension*, 1993. **21**(5): p. 667-673.

159. Kubes, P., M. Suzuki, and D. Granger, *Nitric oxide: an endogenous modulator of leukocyte adhesion*. Proceedings of the National Academy of Sciences, 1991. **88**(11): p. 4651-4655.
160. Dimmeler, S. and A.M. Zeiher, *Nitric oxide—an endothelial cell survival factor*. Cell Death & Differentiation, 1999. **6**(10).
161. Wohlfart, P., et al., *Antiatherosclerotic effects of small-molecular-weight compounds enhancing endothelial nitric-oxide synthase (eNOS) expression and preventing eNOS uncoupling*. J Pharmacol Exp Ther, 2008. **325**(2): p. 370-9.
162. Sasaki, K., et al., *Ex vivo pretreatment of bone marrow mononuclear cells with endothelial NO synthase enhancer AVE9488 enhances their functional activity for cell therapy*. Proc Natl Acad Sci U S A, 2006. **103**(39): p. 14537-41.
163. Chen, A.F., J. Ren, and C.Y. Miao, *Nitric oxide synthase gene therapy for cardiovascular disease*. Jpn J Pharmacol, 2002. **89**(4): p. 327-36.
164. O'Connor, D.M. and T. O'Brien, *Nitric oxide synthase gene therapy: progress and prospects*. Expert Opin Biol Ther, 2009. **9**(7): p. 867-78.
165. Satoh, M., et al., *Angiotensin II type 1 receptor blocker ameliorates uncoupled endothelial nitric oxide synthase in rats with experimental diabetic nephropathy*. Nephrol Dial Transplant, 2008. **23**(12): p. 3806-13.
166. Imanishi, T., et al., *Addition of eplerenone to an angiotensin-converting enzyme inhibitor effectively improves nitric oxide bioavailability*. Hypertension, 2008. **51**(3): p. 734-41.
167. John, S., et al., *Increased bioavailability of nitric oxide after lipid-lowering therapy in hypercholesterolemic patients*. Circulation, 1998. **98**(3): p. 211-216.
168. Beyers, R.J., et al., *T(2) -weighted MRI of post-infarct myocardial edema in mice*. Magn Reson Med, 2012. **67**(1): p. 201-9.

169. Coolen, B.F., et al., *Quantitative T2 mapping of the mouse heart by segmented MLEV phase-cycled T2 preparation*. *Magnetic resonance in medicine*, 2014. **72**(2): p. 409-417.
170. Waters, D.D. and J.S. Forrester, *Myocardial ischemia: detection and quantitation*. *Ann Intern Med*, 1978. **88**(2): p. 239-50.
171. Liu, A., et al., *Diagnosis of Microvascular Angina Using Cardiac Magnetic Resonance*. *J Am Coll Cardiol*, 2018. **71**(9): p. 969-979.
172. Pepine, C.J., et al., *Emergence of Nonobstructive Coronary Artery Disease: A Woman's Problem and Need for Change in Definition on Angiography*. *J Am Coll Cardiol*, 2015. **66**(17): p. 1918-33.
173. Kuruvilla, S. and C.M. Kramer, *Coronary microvascular dysfunction in women: an overview of diagnostic strategies*. *Expert Rev Cardiovasc Ther*, 2013. **11**(11): p. 1515-25.
174. Brant, L.C., et al., *Relations of Metabolically Healthy and Unhealthy Obesity to Digital Vascular Function in Three Community-Based Cohorts: A Meta-Analysis*. *J Am Heart Assoc*, 2017. **6**(3).
175. Beckman, J.A. and M.A. Creager, *Vascular Complications of Diabetes*. *Circ Res*, 2016. **118**(11): p. 1771-85.
176. Labazi, H. and A.J. Trask, *Coronary microvascular disease as an early culprit in the pathophysiology of diabetes and metabolic syndrome*. *Pharmacol Res*, 2017. **123**: p. 114-121.
177. Streif, J.U., et al., *In vivo assessment of absolute perfusion and intracapillary blood volume in the murine myocardium by spin labeling magnetic resonance imaging*. *Magn Reson Med*, 2005. **53**(3): p. 584-92.
178. Cui, S.X. and F.H. Epstein, *MRI assessment of coronary microvascular endothelial nitric oxide synthase function using myocardial T1 mapping*. *Magn Reson Med*, 2017.

179. Campbell-Washburn, A.E., et al., *Cardiac arterial spin labeling using segmented ECG-gated Look-Locker FAIR: variability and repeatability in preclinical studies*. Magn Reson Med, 2013. **69**(1): p. 238-47.
180. Troalen, T., et al., *In vivo characterization of rodent cyclic myocardial perfusion variation at rest and during adenosine-induced stress using cine-ASL cardiovascular magnetic resonance*. Journal of Cardiovascular Magnetic Resonance, 2014. **16**(1): p. 18.
181. Capron, T., et al., *Myocardial perfusion assessment in humans using steady-pulsed arterial spin labeling*. Magnetic resonance in medicine, 2015. **74**(4): p. 990-998.
182. Capron, T., et al., *Cine-ASL: A steady-pulsed arterial spin labeling method for myocardial perfusion mapping in mice. Part II. Theoretical model and sensitivity optimization*. Magnetic resonance in medicine, 2013. **70**(5): p. 1399-1408.
183. Cassidy, P.J., et al., *Assessment of motion gating strategies for mouse magnetic resonance at high magnetic fields*. J Magn Reson Imaging, 2004. **19**(2): p. 229-37.
184. Ehman, R.L. and J.P. Felmlee, *Adaptive technique for high-definition MR imaging of moving structures*. Radiology, 1989. **173**(1): p. 255-63.
185. Kim, W.S., et al., *Extraction of cardiac and respiratory motion cycles by use of projection data and its applications to NMR imaging*. Magn Reson Med, 1990. **13**(1): p. 25-37.
186. Spraggins, T.A., *Wireless retrospective gating: application to cine cardiac imaging*. Magn Reson Imaging, 1990. **8**(6): p. 675-81.
187. Le, T.H. and X. Hu, *Retrospective estimation and correction of physiological artifacts in fMRI by direct extraction of physiological activity from MR data*. Magn Reson Med, 1996. **35**(3): p. 290-8.
188. Brau, A.C. and J.H. Brittain, *Generalized self-navigated motion detection technique: Preliminary investigation in abdominal imaging*. Magn Reson Med, 2006. **55**(2): p. 263-70.

189. Heijman, E., et al., *Comparison between prospective and retrospective triggering for mouse cardiac MRI*. NMR Biomed, 2007. **20**(4): p. 439-47.
190. Nieman, B.J., K.U. Szulc, and D.H. Turnbull, *Three-dimensional, in vivo MRI with self-gating and image coregistration in the mouse*. Magn Reson Med, 2009. **61**(5): p. 1148-57.
191. Kober, F., et al., *Myocardial blood flow mapping in mice using high-resolution spin labeling magnetic resonance imaging: influence of ketamine/xylazine and isoflurane anesthesia*. Magn Reson Med, 2005. **53**(3): p. 601-6.
192. Christian, T.F., et al., *Absolute Myocardial Perfusion in Canines Measured by Using Dual-Bolus First-Pass MR Imaging*. Radiology, 2004. **232**(3): p. 677-684.
193. Schuster, A., et al., *Quantitative assessment of magnetic resonance derived myocardial perfusion measurements using advanced techniques: microsphere validation in an explanted pig heart system*. Journal of Cardiovascular Magnetic Resonance, 2014. **16**(1): p. 82.
194. Decking, U.K., et al., *High-resolution imaging reveals a limit in spatial resolution of blood flow measurements by microspheres*. Am J Physiol Heart Circ Physiol, 2004. **287**(3): p. H1132-40.
195. Lesman, A., et al., *Transplantation of a tissue-engineered human vascularized cardiac muscle*. Tissue Eng Part A, 2010. **16**(1): p. 115-25.
196. Hiba, B., et al., *Cardiac and respiratory double self-gated cine MRI in the mouse at 7 T*. Magn Reson Med, 2006. **55**(3): p. 506-13.
197. Troalen, T., et al., *Cine-ASL: a steady-pulsed arterial spin labeling method for myocardial perfusion mapping in mice. Part I. Experimental study*. Magn Reson Med, 2013. **70**(5): p. 1389-98.

198. Raher, M.J., et al., *In vivo characterization of murine myocardial perfusion with myocardial contrast echocardiography: validation and application in nitric oxide synthase 3 deficient mice*. *Circulation*, 2007. **116**(11): p. 1250-7.
199. Vandsburger, M.H., et al., *Multi-parameter in vivo cardiac magnetic resonance imaging demonstrates normal perfusion reserve despite severely attenuated beta-adrenergic functional response in neuronal nitric oxide synthase knockout mice*. *European Heart Journal*, 2007. **28**(22): p. 2792-2798.
200. Jogiya, R., et al., *Hyperemic stress myocardial perfusion cardiovascular magnetic resonance in mice at 3 Tesla: initial experience and validation against microspheres*. *J Cardiovasc Magn Reson*, 2013. **15**: p. 62.
201. Schwitter, J., et al., *Superior diagnostic performance of perfusion-cardiovascular magnetic resonance versus SPECT to detect coronary artery disease: The secondary endpoints of the multicenter multivendor MR-IMPACT II (Magnetic Resonance Imaging for Myocardial Perfusion Assessment in Coronary Artery Disease Trial)*. *J Cardiovasc Magn Reson*, 2012. **14**: p. 61.
202. Greenwood, J.P., et al., *Cardiovascular magnetic resonance and single-photon emission computed tomography for diagnosis of coronary heart disease (CE-MARC): a prospective trial*. *Lancet*, 2012. **379**(9814): p. 453-60.
203. Benjamin, E.J., et al., *Heart Disease and Stroke Statistics-2017 Update: A Report From the American Heart Association*. *Circulation*, 2017. **135**(10): p. e146-e603.
204. Collins, A.J., et al., *Cardiovascular disease in end-stage renal disease patients*. *Am J Kidney Dis*, 2001. **38**(4 Suppl 1): p. S26-9.
205. Wang, D.J., et al., *Estimation of perfusion and arterial transit time in myocardium using free-breathing myocardial arterial spin labeling with navigator-echo*. *Magn Reson Med*, 2010. **64**(5): p. 1289-95.

206. Soule, B.P., et al., *The chemistry and biology of nitroxide compounds*. Free Radical Biology and Medicine, 2007. **42**(11): p. 1632-1650.
207. Kuppusamy, P., et al., *Noninvasive imaging of tumor redox status and its modification by tissue glutathione levels*. Cancer Res, 2002. **62**(1): p. 307-12.
208. Keana, J.F.W., S. Pou, and G.M. Rosen, *Nitroxides as Potential Contrast Enhancing Agents for Mri Application - Influence of Structure on the Rate of Reduction by Rat Hepatocytes, Whole Liver Homogenate, Subcellular-Fractions, and Ascorbate*. Magnetic Resonance in Medicine, 1987. **5**(6): p. 525-536.
209. Hyodo, F., et al., *Probing the intracellular redox status of tumors with magnetic resonance imaging and redox-sensitive contrast agents*. Cancer Res, 2006. **66**(20): p. 9921-8.
210. Matsumoto, K., et al., *High-resolution mapping of tumor redox status by magnetic resonance imaging using nitroxides as redox-sensitive contrast agents*. Clin Cancer Res, 2006. **12**(8): p. 2455-62.
211. Radu, M. and J. Chernoff, *An in vivo Assay to Test Blood Vessel Permeability*. Journal of Visualized Experiments : JoVE, 2013(73): p. 50062.
212. Demsar, F., et al., *A MRI spatial mapping technique for microvascular permeability and tissue blood volume based on macromolecular contrast agent distribution*. Magnetic Resonance in Medicine, 1997. **37**(2): p. 236-242.